Multi-Scale Simulation and Optimization of Lithium Battery Performance

by

Stephanie L. Golmon

B.S., Principia College, 2007

M.S., University of Colorado, 2009

A thesis submitted to the

Faculty of the Graduate School of the

University of Colorado in partial fulfillment

of the requirements for the degree of

Doctor of Philosophy

Department of Aerospace Engineering Sciences

2014

This thesis entitled:
Multi-Scale Simulation and Optimization of Lithium Battery Performance
written by Stephanie L. Golmon
has been approved for the Department of Aerospace Engineering Sciences

_____

Prof. Kurt Maute

_____

Prof. Martin L. Dunn

Date _____

The final copy of this thesis has been examined by the signatories, and we find that both the content and the form meet acceptable presentation standards of scholarly work in the above mentioned discipline.

Golmon, Stephanie L. (Ph.D., Aerospace Engineering Sciences)

Multi-Scale Simulation and Optimization of Lithium Battery Performance

Thesis directed by Prof. Prof. Kurt Maute

The performance and degradation of lithium batteries strongly depends on electrochemical, mechanical, and thermal phenomena. While a large volume of work has focused on thermal management, mechanical phenomena relevant to battery design are not fully understood. Mechanical degradation of electrode particles has been experimentally linked to capacity fade and failure of batteries; an understanding of the interplay between mechanics and electrochemistry in the battery is necessary in order to improve the overall performance of the battery. A multi-scale model to simulate the coupled electrochemical and mechanical behavior of Li batteries has been developed, which models the porous electrode and separator regions of the battery. The porous electrode includes a liquid electrolyte and solid active materials. A multi-scale finite element approach is used to analyze the electrochemical and mechanical performance. The multi-scale model includes a macro- and micro-scale with analytical volume-averaging methods to relate the scales. The macro-scale model describes Li-ion transport through the electrolyte, electric potentials, and displacements throughout the battery. The micro-scale considers the surface kinetics and electrochemical and mechanical response of a single particle of active material evaluated locally within the cathode region. Both scales are non-linear and dependent on the other. The electrochemical and mechanical response of the battery are highly dependent on the porosity in the electrode, the active material particle size, and discharge rate. Balancing these parameters can improve the overall performance of the battery. A formal design optimization approach with multi-scale adjoint sensitivity analysis is developed to find optimal designs to improve the performance of the battery model. Optimal electrode designs are presented which maximize the capacity of the battery while mitigating stress levels during discharge over a range of discharge rates.

Acknowledgements

Thanks to my advisors, Professors Kurt Maute and Martin L. Dunn for their encouragement, helpful discussions, and overall support. Thanks to my committee members: Professors Sehee Lee, Alireza Doostan, and Carlos Felippa. Thanks for support from my research group members, family, and friends.

Thanks for funding support from the National Science Foundation under the Graduate Research Fellowship Program, and Ann Smead and Michael Byram for their support through the Joseph Smead Graduate Student Fellowship. This research was also supported through the Air Force Office of Scientific Research MURI (grant F9550-06-1-0326) Energy Harvesting and Storage Systems for Future Aerovehicles, monitored by Dr. B.L. Lee, and the National Science Foundation under Grant CMMI 0729520.

Contents

Chapter

Tables

Table

Figures

Figure

Chapter 1

Introduction

1.1 Motivation and Goals

Batteries are a critical component in modern electronics, from micro-electronics, to iPods, to hybrid and electric cars. There is a constant and consistent demand for more reliable, longer lifetime, higher energy density, and increased rate capability from batteries. In addition, electrochemical energy storage is becoming a key component in integrating renewable energy sources into the power grid by mitigating the requirement to use power as it is generated. Improvement in rechargeable battery technology is enabling the production of today's hybrid-electric and all electric vehicles. Research on battery technology seeks to improve the energy density, rate capability, and/or lifetime of the battery. Much of this research is focused on the materials systems of the battery components while some is focused on electrode and overall battery architectures. Lithium ion chemistries are among the most promising material systems due to their higher energy densities and operating voltages as compared to other chemistries. However rechargeable lithium batteries generally have much shorter lifetimes, and are limited in number of charge-discharge cycles due to degradation of the electrodes and electrolyte[79]. This degradation, as well as the overall battery performance, has been experimentally linked to electrochemical, mechanical, and thermal phenomena. While a large volume of work has focused on thermal management, an understanding of the interplay between mechanics and electrochemistry in the battery is necessary in order to improve the overall performance of the battery. This dissertation extends existing electrochemical models of lithium-ion battery performance to include mechanical effects and applies a design optimization

methodology to improve the battery performance through functionally graded electrode structures.

Battery performance is often measured via (1) Ragone charts[17] which plots the power (or rate) capability vs. usable energy storage capacity and (2) in terms of capacity fade when charging and discharging the battery. Typically Ragone plots show a tradeoff between power and capacity - at low power requirements, the energy storage capacity is high, however as the power requirement increases, the storage capacity decreases. Figure 1.1 shows the power versus energy storage capacity for typical electrochemical energy storage devices. The diagonal lines show the time constants for these devices. As the power requirement increases, the devices reach a power plateau. This figure

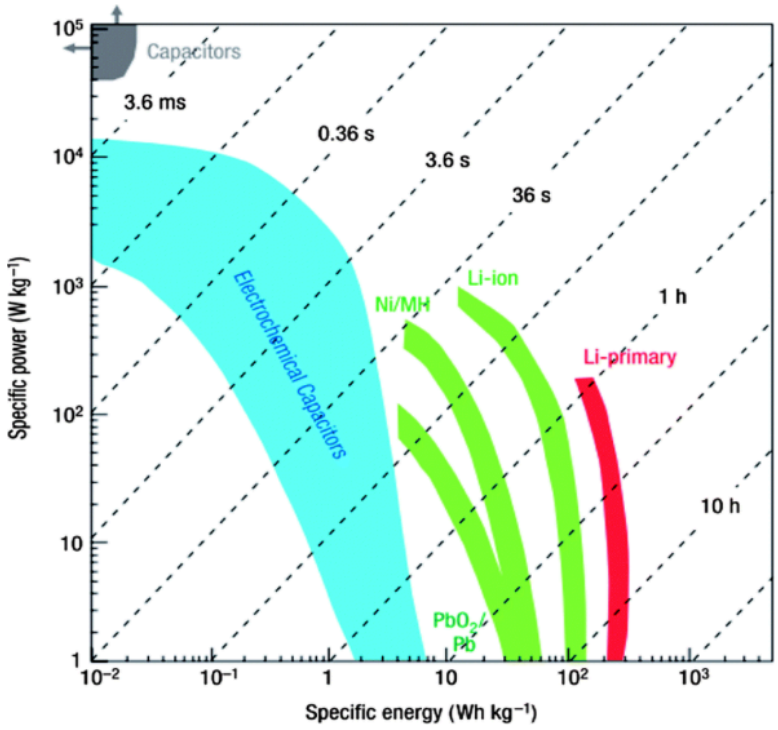

Figure 1.1: Ragone plot for electrochemical energy storage devices[66]

compares capacitors, electrochemical capacitors, and several battery chemistries. Capacitors have the highest power capability, but are limited in the amount of energy they can store; electrochemical capacitors are capable of greater energy storage, but with lower high power capability. Battery technologies have a lower power capability, but increased energy storage capacity. Four types of batteries are shown here, at the left is PbO_2/Pb or lead-acid battery, next is Ni/MH, then Li-ion,

and Li-primary batteries. Li-primary batteries are single-use batteries and have the highest energy storage capacities, while Li-ion (or secondary) batteries are rechargeable Li batteries. The focus of this study is on Li-ion rechargeable batteries. The goal is to increase the energy storage capacity - shifting the lines to the right, and to increase the power capability - extending the lines upwards - without sacrificing energy storage capacity.

Capacity fade of the battery when cycling (charging and discharging) the battery is an area of great concern as even a slight loss in capacity during each cycle will be significant when the battery is cycled 3,000 to 10,000 times as is needed in many applications.[67] Experimental studies have linked capacity fade with cracks in electrode particles[76] and shown that electrode particles are not uniformly strained during cycling [77].

This dissertation focuses on understanding and simulating the interplay between electrochemical and mechanical phenomena in the battery and subsequently improving the performance of the battery by optimizing the electrode structures. To this end, a multi-scale model to simulate the coupled electrochemical and mechanical behavior of Li batteries has been developed, which models the porous electrodes and separator regions of the battery. A multi-scale finite element approach is used to analyze the electrochemical and mechanical performance. This model includes a macro- and micro-scale with analytical volume-averaging methods to relate the scales. The macro-scale model describes Li-ion transport through the electrolyte, electric potentials, and deformations throughout the battery. The micro-scale considers the surface kinetics and the electrochemical and mechanical response of a single particle of active material evaluated locally within the electrode region. Both scales are non-linear and dependent on the other. The electrochemical and mechanical response of the battery are highly dependent on the porosity, the electrolyte volume fraction, in the electrode; the electrode active material particle size; and discharge rate. Balancing these parameters can improve the overall performance of the battery. A formal design optimization approach is used to find optimal electrode designs to improve the performance of the battery model via gradient-based optimization schemes. To this end, a decomposition method for computing the multi-scale adjoint sensitivities is developed which significantly reduces the computational time required for sensitivity

analysis versus numerical finite differencing. Optimal electrode designs are presented which maximize the capacity of the battery while mitigating stress levels during discharge over a range of discharge rates.

1.2 Structure of Dissertation

This dissertation summarizes the author's work completed during her Ph.D. studies. The majority of the work has been published; therefore this document focuses on the fundamental aspects of the study, outlining the basic concepts and theory with the publications included in the Appendices.

Chapter 2 introduces the multi-scale battery model and investigates the electrochemical and mechanical affects at both scales. This model is used to simulate the battery behavior in the author's publications, see Appendices A-D. Additionally, previously unpublished results from a single-scale study on silicon anodes are included in this chapter.

Chapter 3 focuses on design optimization as applied to Li batteries. A multi-scale adjoint sensitivity analysis method was developed to perform the sensitivity analysis on the battery using both macro- and micro-scale design variables. This efficient computation of the design sensitivities allows for the use of gradient-based optimization algorithm to predict optimal electrode structures. The development of the multi-scale adjoint sensitivity approach is detailed in C. Publications C and D present results of completed multi-scale optimization studies for lithium batteries.

Chapter 4 summarizes the completed study and ideas for future work.

1.3 Summary of Publications

Brief summaries of the author's publications are provided in this section.

1.3.1 Summary of A: Numerical modeling of electrochemical-mechanical interaction in lithium polymer batteries

This study presents a multi-scale finite element model for lithium batteries to study electrochemical and mechanical interaction phenomena. The battery model consists of a lithium foil anode, a separator, and a porous cathode that includes solid active materials and a liquid electrolyte. Three length scales are considered in this model. At the macro-scale, transport processes and mechanical deformations in the entire battery layer are modeled; at the micro- scale, a single active material particle in the cathode is modeled; and at the meso-scale, homogenization methods based on particle aggregates relate the micro- and macro-scales.

The macro-scale model is based on the work of Doyle **et. al**[29, 36, 35, 30, 28] which utilizes porous electrode theory [59, 28] and concentrated solution theory [59, 28] to predict the electrochemical response in the separator and electrode. This model is applicable to lithium-ion batteries with at least one porous insertion electrode in which the electrode acts as a host for the lithium ions tranported through a binary electrolyte. This model is extended to account for elastic and inelastic deformations due external loads and electrochemical eigenstrains resulting from swelling of the aggregate structure. The micro-scale model is based on the work of Zhang *et al.* [84], and models the Li diffusion into the particle and resulting diffusion-induced stresses in the particle. A multi-scale approach to analyze the surface kinetics and electrochemicalmechanical phenomena within a single spherical particle of the active material is developed. At the meso-scale, analytical homogenization methods are used to relate the macro- and micro-scales via an effective flux of Li^+ intercalating into the active material particles from the electrolyte and an effective chemically induced eigenstrain due to the swelling of the particles.

Results of this study show the time-evolution profiles of the Li^+ concentration in the electrolyte, stresses in the electrode due to aggregate swelling of the particles, and Li concentration and diffusion induced stresses in individual active material particles. The influence of discharge rate, electrode particle size, and the effect of external mechanical stress are investigated. Results

show lower stress levels for lower discharge rates, better electrochemical performance and lower particle-level stresses for smaller cathode particle sizes, and no influence of mechanical boundary conditions on electrochemical performance.

1.3.2 Summary of B: Stress Generation in Silicon Particle During Lithium Insertion

This study focuses on the single electrode particle model for spherical silicon particles. The model is based on the micro-scale model presented in [39] (Appendix A). The insertion of lithium into a spherical particle is simulated using the fully-coupled diffusion-elasticity model with Butler-Volmer surface kinetics. Simulations predict the evolution of concentration, displacements, and stresses in the particles during the initial insertion of Li. The particle response depends strongly on the reaction kinetics and the resulting stresses can be above the tensile failure limit of silicon depending on the particle size and discharge rate. Results of this study predict peak particle stress as a function of Li insertion rate and particle size. These results can be interpreted as a failure map to predict when particles can be expected to fail when incorporated into a battery.

1.3.3 Summary of C: Multi-Scale Design Optimization of Lithium Ion Batteries with Adjoint Sensitivity Analysis

This study applies design optimization to the battery model introduced in [39] (Appendix A) to predict optimal electrode architectures to improve the energy storage capacity of the battery. A computational framework for optimizing the multi-scale lithium ion battery cell model is developed. A key component of the optimization methodology is the development of the adjoint sensitivity equations for the multiscale battery model. The efficient solution of the adjoint equations relies on the decomposition of the multiscale problem into multiple, computationally small problems associated with the individual realizations of the micro-scale model. This decomposition method is shown to significantly reduce the computational time needed for sensitivity analysis versus numerical finite differencing. The potential of the proposed optimization framework is illustrated with

numerical examples involving both macro-scale and micro-scale performance criteria and design variables. The usable capacity of a lithium ion battery cell is maximized while limiting the stress level in the electrode particles through manipulation of the local porosities and particle radii. The optimization results suggest that optimal functionally graded electrodes improve the performance of a battery cell over using uniform porosity and particle radius distributions.

1.3.4 Summary of D: A Design Optimization Methodology for Li^+ Batteries

This study applies the design optimization methodology developed in [40] (Appendix C), to the optimization of the battery electrode over a range of discharge rates. A multi-objective formulation of the design problem is introduced to maximize the usable capacity over a range of discharge rates while limiting the mechanical stresses. Design optimization for functionally graded battery electrodes is shown to improve the usable energy capacity of Li batteries predicted by computational simulations by numerically optimizing the electrode porosities and particle radii. Studies were performed on both half and full cell configurations resulting in distinctly different optimal electrode designs. The numerical results show that the highest rate discharge drives the simulations and the optimal designs are dominated by Li^+ transport rates. The results also suggest that spatially varying electrode porosities and active particle sizes provides an efficient approach to improve the power-to-energy density of Li+ batteries. For the half-cell configuration, the optimal design improves the discharge capacity by 29% while for the full cell the discharge capacity was improved 61% relative to the initial design. Most of the improvement in capacity was due to the spatially varying porosity, with up to 5% of the gains attributed to the particle radii design variables.

Chapter 2

Battery Simulation

This chapter presents a broad overview of battery operation and previous work, outlines the multi-scale battery model used in the author's work - references [39, 40, 41] (Appendices A, C, and D), and presents previously unpublished results from a single-scale study on silicon anodes extending the work from Ref. [42] (Appendix B).

2.1 Battery Operation & Simulation

A typical Li battery is shown in Figure 2.1 and consists of current collectors, porous electrodes, and separator regions. The porous electrode includes active insertion compounds, conductive additives, and binders with electrolyte filling the pores. The liquid volume fraction of electrolyte in referred to as the porosity, ε, and in a typical battery is 30%[79]. When the battery is discharged, Li in the anode oxidizes. Electrons flow through the external circuit to the cathode and lithium ions, Li^+, are transported through the electrolyte via diffusion and migration to the cathode where they are reduced. In modern Li batteries, Li inserts into a host electrode material rather than plating onto metals, and these compounds shrink and swell as a result of the Li insertion and de-insertion. The resulting stresses can be high enough to fracture the active particle and experimental studies have linked mechanical effects with capacity fade[76] and localized degradation of the electrode[77]. These studies demonstrate that it is necessary to consider mechanical effects when designing a battery.

Here, the battery performance is investigated using a multi-scale model to simulate the full

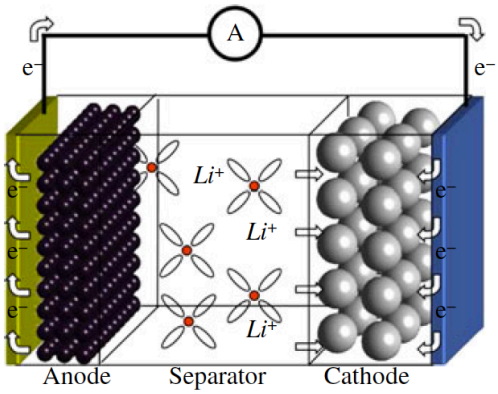

Figure 2.1: Battery cell.

battery and a single-scale model for Li concentration and stress fields in electrode particles during Li insertion. This chapter overviews previous work on battery simulation, and presents the multi-scale battery model and single-scale electrode particle model that are the basis for the publications.

2.2 Previous Work

Much of the previous work on modeling lithium batteries has focused on electrochemical and thermal phenomena in porous electrodes[9]. West *et al.*[78] and Doyle *et al.*[29] simulate electrochemical performance in lithium batteries using a porous electrode model. The porous electrode approach treats electrode regimes as a continuous superposition of solid electrode material and liquid electrolyte domains characterized by the relative porosity or liquid volume fraction of the electrolyte. This porous electrode approach has also been applied to Ni-MH batteries[45] and extended to include thermal effects in Ni-MH batteries[44] as well as thermal effects in lithium batteries[74, 54]. Kumaresan, Sikha, and White[54] compared their electrochemical-thermal model to experimental results to determine the solid-phase diffusion coefficient, kinetic constants, and thermal conductivity of the battery showing good agreement between predicted and experimental discharge curves and temperature increases. Porous electrode models have been extended to include capacity fade[68] and use more detailed models for the electrode conductivity, accounting for electron transfer between different-sized particles and materials including the conductive

carbon additives[70]. More recent work has extended the porous electrode to three-dimensions to resolve electrochemical, electrical, and thermal fields in large-format stacked prismatic battery cell designs.[51]

Some studies have opted to investigate the effects of the detailed electrode micro-structure. Wang and Sastry[75] studied the effects of regular and random arrays of cathode particles on the achievable capacity as compared to the theoretical capacity of the battery showing that, at low discharge rates, regular arrays can increase the achievable capacity by a factor of 10 compared to random arrays. Garcia *et al.*[38, 37] developed a two-dimensional single-scale model that includes the swelling of the electrode particles upon lithium insertion and studied the performance of various nano-structured electrode layouts showing that decreased distance between the electrodes is desirable.

Consideration of mechanical phenomena during charge and discharge is important for understanding fade and failure mechanisms in the battery as experimental studies have linked capacity fade of batteries to crack growth in the electrodes[76, 77]. Stress-induced surface cracks in electrode particles have been shown to nucleate new solid electrolyte interphase (SEI) layer growth and substantially contribute to the loss of Li, resulting in capacity fade.[27] In situ observations of the expansion of graphite particles upon lithiation have shown that the particle level strains are an order of magnitude higher than at the composite level due to the porosity of the electrode and that overall porosity changes significantly upon lithiation.[63]

Several studies have focused on modeling the electrochemistry, stress, and crack formation in a single electrode particle. Zhang *et al.*[82] modeled lithium intercalation into a single Mn_2O_4 particle with surface kinetics governed by a cyclic linear potential sweep and compared the predicted current density vs. applied voltage from their model to experimental work showing good agreement. Christensen and Newman[18] have developed a model for the growth of the solid electrolyte interphase layer on negative electrode particle surfaces to quantify capacity loss in a cell. Huggins and Nix[46] developed a one-dimensional model to predict stresses and fracture in electrodes undergoing volume changes. Their model predicts a terminal particle size below which particles are

not expected to crack. Aifantis and co-authors[1, 2, 3] have modeled crack formation in electrodes using facture mechanics; cracks in the electrode may break off pieces of the active material resulting in capacity fade due to loss of electrical contact and new SEI layer growth. Aifantis *et al.*[3] used fracture mechanics to predict when an electrode particle will fracture, finding that smaller particles are preferable. Christensen and Newman[21] predicted, for a single spherical particle, stress generation and fracture in lithium insertion compounds finding that particles are more likely to fracture when used in high-power applications. In subsequent work[20], they also modeled the effects for a spherical particle of lithium manganese oxide, predicting that the intercalation-induced stress can exceed the strength of the particles. Zhang *et al.*[84] studied intercalation-induced stress in $LiMn_2O_4$ particles, treating the intercalation-induced stress analogously to thermal stress and extending the spherical model to ellipsoidal particles. This study includes the effect of stress enhancing diffusion within the particle, however it ignores possible surface tractions due to external mechanical loads, surface stress effects, and constraint of the particle by the surrounding electrode matrix. An extension of this study also included heat generation within the single particle.[83] Cheng and Verbrugge developed analytical models for diffusion-induced stresses for both galvanostatic and potentiostatic operation of cells,[14, 15] with and without the influence of surface kinetics and not accounting for the influence of stress on diffusion.

Studying the mechanics of batteries at the cell level is necessary to understand the effects of swelling of the electrode particles, applied loads due to packaging of a battery in a pack, or incorporating the battery into a composite as a structural member. The swelling of electrode particles with Li insertion has been harnessed to utilize a battery as an electrochemical actuator with reversible linear strains of $\sim$3% under zero stress and 1.5% strain under 10MPa stress.[16] Batteries have been incorporated into structures and studies on the effect of external mechanical loads have been performed. Thomas and Qidwai[73] have placed commercial lithium batteries in the wings of microair vehicles (MAV) resulting in improved range of the MAV. In their mechanical model of structurally integrated batteries, Thomas and Qidwai[73] assumed that the effects of electrochemical-mechanical interactions are negligible. Pereira *et al.* have studied experimentally

the effects of flexural deection[61] and uniaxial pressure[60] on lithium thin film batteries. Their observations suggest that up until structural failure of the battery, the electrochemical performance of the battery is not signicantly affected by external mechanical loads. These authors showed in a subsequent paper[62] that the same batteries could be successfully incorporated into a carbon fiber composite lay-up without degrading the battery performance to improve the mechanical properties of the composite.

2.3 Multi-Scale Battery Model

The multi-scale battery model developed in the author's work is an extension of Doyle and Newman's electrochemical battery model[29, 36, 35, 30, 28] to include mechanical effects across the full electrode and at the single electrode particle level. Here, the electrodes are simulated using porous electrode theory[59, 28], treating the electrode as a superposition of solid and liquid phases, rather than modeling the detailed microstructure of the electrode. The model is extended to include deformations due to external mechanical loads and swelling of electrode particles upon lithiation. The effects of Li^+ transport in the electrolyte, Li transport in the electrode particles, local electrode surface kinetics, diffusion-induced stresses in the electrode particles, and resulting aggregate swelling of the electrode are considered. Solid electrolyte interphase (SEI) layer growth, chemical side reactions, thermal effects, and degradation effects due to cycling and aging are not included.

This model results in two length scales: at the macro-scale, transport processes in the electrolyte, electric potentials in both the electrode and electrolyte, and mechanical deformations across the full battery are modeled; at the micro-scale, the response of a single representative electrode particle is modeled; a meso-scale is used to relate these two scales using volume averaging homogenization methods. An overview of numerical multiscale modeling methods can be found in Kanoute *et al.*[48]. This model follows the approach of Miehe *et al.*[57, 56] and Feyel[32, 34, 33], using finite element models at both macro- and micro-scales bridged by volume averaging homogenization methods[58, 7, 8]. At a given material point in the macro-scale model, the local, volume-averaged

response of the micro-scale model is evaluated.

The model is verified against previously published numerical studies[84, 29] on which this model is based. Additionally, previous studies have qualitatively compared discharge curves generated by the electrochemical portion of this model with with experimental data with good agreement.[4, 54]

2.3.1 Governing Equations at Macro-Scale

At the macro-scale, the Li^+ concentration in the electrolyte, c_l, electric potentials in the electrode, ϕ_1, and electrolyte, ϕ_2, phases, and displacements, $\mathbf{u}$, are modeled.

The transport of Li^+ ions through the electrolyte and the current carried by the solid and liquid phases are described by Eqns. 2.1-2.3.[28, 29, 36, 35, 30] The macro-scale mechanical response is assumed to be linear-elastic with a volume-averaged eigenstrain model to account for swelling of the micro-scale electrode particles, Eq. 2.4.

$$\varepsilon \frac{\partial c_l}{\partial t} + \nabla \cdot \mathbf{N} + \frac{1}{F} \frac{\partial t_+^0}{\partial c_l} \mathbf{i}_2 \cdot \nabla c_l - \left(1 - t_+^0\right) j_{\text{eff}} = 0 \tag{2.1}$$

$$\nabla \cdot \mathbf{i}_1 + F j_{\text{eff}} = 0 \tag{2.2}$$

$$\nabla \cdot \mathbf{i}_2 - F j_{\text{eff}} = 0 \tag{2.3}$$

$$\nabla \cdot \boldsymbol{\sigma} + \mathbf{b} = 0 \tag{2.4}$$

with constitutive equations:

$$\mathbf{N} = -D_{\text{eff}} \nabla c_l \tag{2.5}$$

$$\mathbf{i}_1 = -\lambda \nabla \phi_1 \tag{2.6}$$

$$\mathbf{i}_2 = -\kappa_{\text{eff}} \left[\nabla \phi_2 - \frac{RT}{F} \left(1 - t_+^0\right) \nabla ln(c_l) \right] \tag{2.7}$$

$$\boldsymbol{\sigma} = \mathbf{C} : (\mathbf{e} - \mathbf{e}_{ch}), \quad \mathbf{e} = \frac{1}{2} \left(\nabla \mathbf{u} + \nabla \mathbf{u}^T \right) \tag{2.8}$$

D_{eff} is the effective diffusion coefficient of Li^+ in the electrolyte, λ is the conductivity of the electrode particles, κ_{eff} is the effective ionic conductivity of the electrolyte, $\mathbf{C}$ is the homogenized elasticity

tensor, and $\mathbf{e}_{ch}$ is the volume-averaged chemically induced eigenstrain due to the aggregate swelling of the electrode particles. Eq. 2.1 describes the transport of Li^+ ions through the electrolyte where ε is the porosity, $\mathbf{N}$ is the diffusive flux, and F is the Faraday constant. In addition to the diffusive flux, two source terms account for the migration of Li^+ ions due to the current carried by the electrolyte, $\mathbf{i}_2$, and for the effect of Li^+ ions leaving the electrolyte and intercalating into the solid material. The transference number, t_+^0, is the percentage of the current in the solution carried by the Li^+ ion rather than the anion in the solution; this is generally a function of the Li^+ ion concentration in the electrolyte, c_l. Li^+ ions leaving the electrolyte and entering the active electrode material results in an effective pore wall flux, j_{eff}. The currents in the solid active material and liquid electrolyte phases, $\mathbf{i}_1$ and $\mathbf{i}_2$, are governed by Eqns. 2.6 and 2.7, and include the effective pore wall flux to account for Li^+ entering and exiting the two phases. In the electrode, Eq. 2.6, Ohm's law relates the current to the electric potential in the active material particles. Similarly, the electric potential in the electrolyte, 2.7, is governed by a modified Ohm's law that accounts for the dependence of the current in the electrolyte on the concentration of Li^+ in the electrolyte.

At the anode-current collector boundary, Γ_{AC}, and cathode-current collector boundary, Γ_{CC}, all the current is carried by the electrode particles. The boundary conditions are given in Table 2.1.

Table 2.1: Boundary Conditions For Macro-Scale Battery Model

	Anode-Current Collector Boundary Γ_{AC}	Cathode-Current Collector Boundary Γ_{CC}
Li^+ flux	$\nabla c_l = 0$	$\nabla c_l = 0$
Current in solid particles	$\mathbf{i}_1 = I$	$\mathbf{i}_1 = I$
Current in electrolyte	$\mathbf{i}_2 = 0$	$\mathbf{i}_2 = 0$
Displacements	$\mathbf{u} = 0$	$\mathbf{u} = 0$

2.3.2 Governing Equations at Micro-Scale

At the micro-scale, the response of a single electrode particle embedded in the host electrolyte is modeled. The difference in length scales between the macro- and micro-scales allows for the assumption that the macro-scale Li^+ concentration, electric potentials, and displacement fields are spatially constant in the electrolyte immediately surrounding the micro-scale particle. In addition, it is assumed that the micro-scale particles are spherical. These assumptions allow for simplification of the micro-scale model to one dimension using spherical coordinates. The micro-scale model is based on the coupled diffusion-stress model developed by Zhang *et al.*[84], and extended to include Butler-Volmer surface kinetics[6, 59] and surface pressures.

The Li concentration, c_s, and deformation, u_r, fields within the particle are described by diffusion and linear static mechanical models:

$$\frac{\partial c_s}{\partial t} + \left(\frac{\partial}{\partial r} + \frac{2}{r}\right)\mathbf{J} = 0 \tag{2.9}$$

$$\frac{d\sigma_R}{dr} + \frac{2}{r}\left(\sigma_R - \sigma_T\right) = 0 \tag{2.10}$$

with constitutive equations:

$$\mathbf{J} = -D_s\left(\nabla_r c_s - \frac{\Omega c_s}{RT}\nabla_r \sigma_h\right) \tag{2.11}$$

$$\sigma_R = \frac{E}{(1+\nu)(1-2\nu)}\left((1-\nu)\nabla u + 2\nu\frac{u}{r} - \frac{\Omega}{3}c_s(1+\nu)\right) \tag{2.12}$$

$$\sigma_T = \frac{E}{(1+\nu)(1-2\nu)}\left(\frac{u}{r} + \nu\nabla u - \frac{\Omega}{3}c_s(1+\nu)\right) \tag{2.13}$$

where D_s is the diffusion coefficient of Li in the particle; R is the universal gas constant; T, is the temperature; σ_R, σ_T, and σ_h are the radial, tangential, and hydrostatic stresses; and E and ν are the Young's modulus and Poisson's ratio of the electrode material. The Li partial molar volume, Ω, accounts for the swelling of the particle upon lithiation and the degree of stress-diffusion coupling increases with Ω. The hydrostatic stress is defined as:

$$\sigma_h = (\sigma_R + 2\sigma_T)/3 \tag{2.14}$$

At the particle center, $r = 0$, the displacements and Li flux are zero, $u_r = 0,\ \mathbf{J} = 0$. At the particle surface, $r = R_s$, Li enters the particle and a mechanical surface pressure is applied.

$$\mathbf{J} = j_s \ @\ r = R_s \tag{2.15}$$

$$\sigma_R = P_{\text{micro}} \ @\ r = R_s \tag{2.16}$$

The Li pore wall flux at the particle surface, j_s, is described by a Butler-Volmer surface kinetics model which predicts the current/Li flux across the boundary as a function of the electric potentials and concentrations in both phases. In the equations presented here, the anodic and cathodic currents at the particle surface are limited by the availability of active material sites for Li insertion into the particle[29]:

$$j_s = \frac{i_0}{F}\left[c_{s|r=R_s} e^{k_1} - \left(c_{s,\max} - c_{s|r=R_s}\right) e^{k_2}\right] \tag{2.17}$$

$$i_0 = F K_2 \left(c_{l,\max} - c_l\right)^{\alpha_C} \left(c_l\right)^{\alpha_A} \tag{2.18}$$

$$k_1 = \frac{\alpha_A F}{RT}\left(\eta - U'(c_{s|r=R_s})\right) \tag{2.19}$$

$$k_2 = -\frac{\alpha_C F}{RT}\left(\eta - U'(c_{s|r=R_s})\right) \tag{2.20}$$

$$\eta = \phi_1 - \phi_2 \tag{2.21}$$

where $c_{s,\max}$ and $c_{l,\max}$ are the maximum Li and Li^+ concentrations in the electrode particle and electrolyte; α_A and α_C are the anodic and cathodic transfer coefficients; η is the surface overpotential; and $U'(c_{s|r=R_s})$ is the open circuit potential as a function of Li concentration.

The surface pressure the particle sees, P_{micro} has contributions due to the inclusion of the particle in the swelling aggregate, P_h, and from surface stress, P_{SS}:

$$P_{\text{micro}} = P_h + P_{SS} \tag{2.22}$$

For spherical particles, the pressure due to the surface stress can be written as:[14]

$$P_{SS} = -2\frac{\tau_0 + K^s \varepsilon_T \mid_{r=R_s}}{R_s} \tag{2.23}$$

where τ_0 is the deformation-independent surface tension, K^s is the surface modulus, and ε_T is the tangential strain, which in spherical coordinates is defined as: $\varepsilon_T = u_r/r$. This model does not include more complex phenomena such as the effects of chemical potential on stress, non-Fickian diffusion, finite strains, and plastic deformations.[10, 85, 24] These effects could be incorporated in future work.

2.3.3 Governing Equations at Meso-Scale

The micro-scale particles influence the macro-scale response through the effective pore wall flux, j_{eff}, and chemical chemically induced eigenstrain $\mathbf{e}_{ch}$. Similarly, the micro-scale pore wall flux, j_s, and surface pressure, P_h depend on both macro- and micro-scale state variables. Aggregate theory[58] and Bruggeman relations[29, 28] are used to relate the scales. The effective pore wall flux is related to the micro-scale pore wall flux through:

$$j_{\text{eff}} = \frac{3(1-\varepsilon)}{R_s} j_s \tag{2.24}$$

The porosity of the electrode influences the effective properties D_{eff} and κ_{eff} of the electrolyte which are found via Bruggeman relations based on the diffusion coefficient D_l and electrolyte conductivity, κ_∞ in the bulk electrolyte:

$$D_{\text{eff}} = \varepsilon D_l \tag{2.25}$$

$$\kappa_{\text{eff}} = \varepsilon^{3/2} \kappa_\infty \tag{2.26}$$

The Bruggeman relationships account for the reduced volume of the conducting (electrolyte) phase and increased path length or totruosity of the porous material.[28]

The micro-scale surface pressure, and macro-scale chemically induced eigenstrain depend on macro- and micro-scale strains through the Mori-Tanaka model. [58, 7, 8] It is assumed there is no chemically induced strain in the electrolyte.

$$P_h = \left(\mathbf{b}_s + \mathbf{B}_s \mathbf{C}_{\text{eff}} \left(\mathbf{e} - \mathbf{e}_{ch}\right)\right) \hat{\mathbf{n}} \tag{2.27}$$

$$\mathbf{e}_{ch} = (1-\varepsilon)\, \mathbf{e}_V + (1-\varepsilon) \left(\mathbf{C}_s^{-1} - \mathbf{C}_l^{-1}\right) \mathbf{b}_s \tag{2.28}$$

where $\mathbf{C}_l$ and $\mathbf{C}_s$ are isotropic elastic stiffness matrices for the electrolyte and electrode.

The micro-scale volumetric strain, $\mathbf{e}_V$ is found via:

$$\mathbf{e}_V = \frac{1}{3}\left(\frac{\left(R_s + u_{r|r=R_s}\right)^3}{R_s^3} - 1\right) \tag{2.29}$$

2.3.4 Spatial and Temporal Discretization

In a typical Li^+ battery, the thickness of the battery cell is significantly smaller than the overall size of the battery; this allows for an idealization of the model to one-dimension at the macro-scale. The Li transport processes, diffusion and migration at the macro-scale and diffusion at the micro-scale, operate on comparable time-scales, therefore separation in time scales between macro- and micro-scales is not required. At both scales, the governing equations are discretized in time using an implicit Euler backwards scheme and in space using finite elements [39]. Within the electrode domains, separate micro-scale problems are solved at the macro-scale integration points. The micro-scale problems are independent of each other, only coupled via the macro-scale equations. This system of equations is solved via a staggered approach where the micro-scale state variables are considered functions of the macro-scale state variables. This results in a separation of the full system into multiple smaller problems and facilitates parallel computing schemes. Additional details on the numerical implementation can be found in Ref. [40] (Appendix C).

2.4 Single-Scale Silicon Study

In addition to the multi-scale full battery model presented in Section 2.3, simulations of single silicon anode particles were conducted. This section expands upon previous work (Ref. [42], Appendix B), extending the published results to include surface stress effects that result in a lower limit for silicon particle size.

Silicon anodes show promise due to their high gravimetric capacity, in excess of 4000 mA h/g[43, 49] as compared to 372 mA h/g for typical carbonaceous anodes[43]. This high capacity, however, is coupled with a volume expansion on the order of 300-400%[5, 11] upon full lithiation

of the anode. The stress associated with this large volume expansion have been cited as the cause of the cracking and pulverization of the electrode seen experimentally.[49] Fracture of the electrode material results in loss of electrical contact, and thus decreases the capacity of the battery and exposes new electrode surfaces to the electrolyte resulting in new SEI layer growth and additional capacity fade of the battery. Literature values for the tensile failure stress of silicon are in the range of 1-4 GPa.[71, 22]

Previous work suggests that silicon anodes with morphology of nanometer scale dimensions are more robust than anodes with larger-dimension morphology with regard to cyclic degradation. For example, Li *et al.*[55] showed that composite anodes with Si particles in the 50-100 nm range have better cycling performance than those in the μm range. Another line of inquiry has shown that arrays of Si nanowires exhibit cycling performance with no degradation.[23] A third example showed that nanoporous Si architectures result in capacity retention that exceeds that of nano-scale particles and nanowires.[52] Presumably the improvement that results from these nano-scale architectures is related to the stresses developed during cycling. Mechanistic details regarding the cyclic degradation that leads to capacity fade, are not well developed, and many papers simply state that it is related to the large volume change that results upon Li insertion. Here, the linear-elastic particle model with diffusion-induced stresses is used as a first step to quantify the development of stresses in a single Si particle during the insertion of Li. A ButlerVolmer model that describes the electrochemical reaction kinetics at the Si particle/electrolyte interface, models the influx of Li. The effects of the particle size and Li insertion rate on the maximum tensile stress in the particle are studied. The focus is on the first insertion of Li into Si to quantify the initial development of stresses. The impact of degradation mechanisms during cycling is beyond the scope of this study. Results form a parameter map of the maximum tensile stress vs. rate and particle size and can be interpreted as guidelines to design cracking-resistant Si anodes.

Table 2.2: Material Parameters for Silicon Surface Stress Effect

Symbol	Value	Units	
τ_0	-0.606	J/m^3	surface tension
K^s	10.65	N/m	surface modulus

2.4.1 Silicon Particle Model

The particle is idealized as a sphere embedded in a host electrolyte with uniform Li^+ concentration and solid and liquid-phase electric potentials in the surrounding electrolyte; this allows for simplification of the governing equations to one dimension. The micro-scale particle governing and constitutive equations are the same as in Section 2.3.2 (Eqns. (2.9)-(2.14)). At the particle center, $u = 0$ and $\mathbf{J} = 0$; at the particle surface, $\mathbf{J} = j_s$ and $\sigma_R = P_{micro}$ (Eqns. (2.15) and (2.16)). The Li^+ flux is governed by a Butler-Volmer equation for the kinetics of the electrochemical reaction:[82]

$$\mathbf{J} = \frac{i_0}{F}\left[\exp\left(\frac{\alpha_A F}{R_g T}\left(\eta - U\left(c/c_{max}\right)\right)\right) - \exp\left(\frac{\alpha_C F}{R_g T}\left(\eta - U\left(c/c_{max}\right)\right)\right)\right] \tag{2.30}$$

$$i_0 = Fk\left(c_l\right)^{\alpha_A}\left(c_{max} - c\right)^{\alpha_A}\left(c\right)^{\alpha_C} \tag{2.31}$$

In Eqs. (2.30) and (2.31), F is the Faraday constant, c_l is the concentration of lithium in the surrounding matrix, k is the interfacial charge transfer reaction constant, η is the electric potential difference between the silicon particle and surrounding electrolyte, and $U(c/c_{max})$ is the open circuit electric potential of lithium in silicon. c_l, k, and T are taken to be constant in these simulations.

In the original publication, Ref. [39] (Appendix B), the surface was free to expand, $P_{micro} = 0$; surface stress and pressure due to swelling of the aggregate electrode structure were not included. Here, the model is expanded to include the surface stress effect, $P_{micro} = P_{SS}$, Eq. (2.23)[14]. Material parameters used in the model are given in Table 1 of Ref. [42] (Appendix B), and surface stress effect parameters for Silicon are in Table 2.2.

The model is driven by linearly varying the electric potential difference between the Si particle and surrounding electrolyte, η. The rate the electric potential difference is changed is the potential sweep rate, v; i.e., $\eta = \eta_0 - vt$ for $vt < \eta_0$ and $\eta = 0$ for $vt > \eta_0$. The difference between the applied potential and equilibrium open circuit potential drives the electrochemical reaction at the

particle surface, resulting in a current flux, and corresponding Li^+ flux, at the particle surface. The potential sweep rate and the radius of the Si particle affect the maximum tensile stresses in the particle.

2.4.2 Results

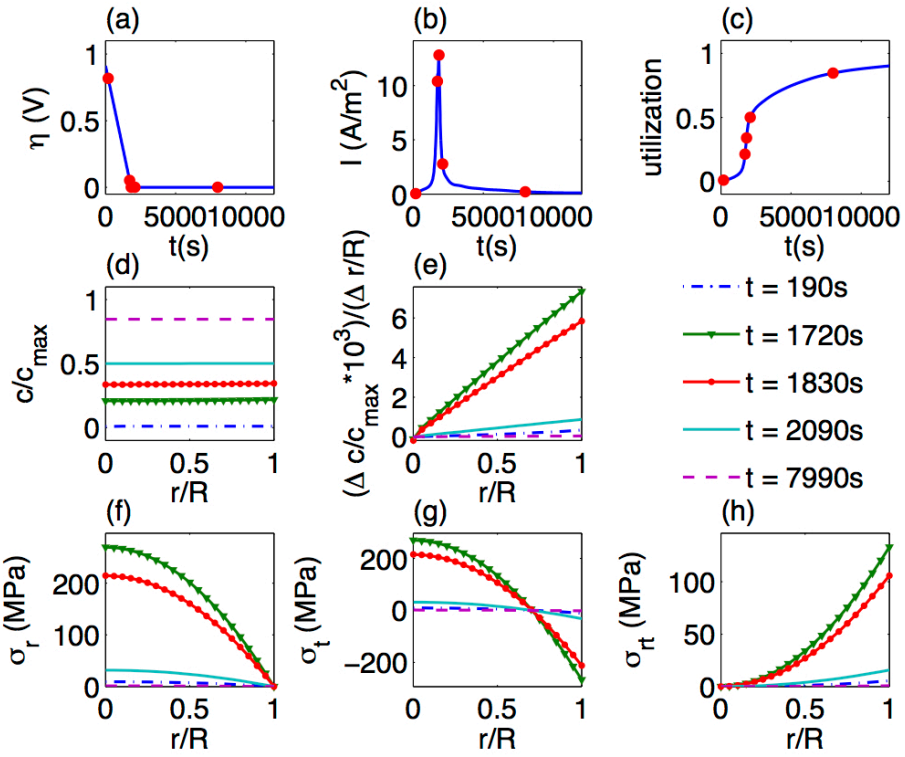

Figure 2.2: Behavior of single silicon particle model with time. (a) Applied overpotential, η, (b) current, I, and (c) particle utilization, as a function of time. (d) c/c_{max}, (e) $(\Delta c/c_{max})/(\Delta r/R)$, (f) radial stress, σ_r, (g) tangential stress, σ_t, and (h) shear stress, σ_{rt}, profiles across the radius of a $R = 1\mu m$ particle at different times for a potential sweep rate of $v = -0.5mV/s$. The time instances shown in plots (d)-(h) correspond to the times marked with dots in plots (a)-(c).

Figure 2.2, reprinted from Ref. [42], illustrates the spatial and temporal variation of the concentration and stress fields during lithium insertion, without accounting for the surface stress effects. The overpotential, η, is decreased linearly to zero, and then is maintained at zero, (Fig. 2.2a). The resulting current influx into the particle, (Fig. 2.2b), varies with time, peaking when the

difference between the applied overpotential η and open circuit potential, $U(c/c_{max})$, is greatest. The current influx drives the overall utilization of the particle, (Fig 2.2c). The timescales of Li insertion into and diffusion within the sphere are such that the spatial distribution of lithium in the sphere remains nearly constant at all times, (Fig. 2.2d), however there is a gradient in the concentration with higher concentrations at the particle surface than at the center, (Fig. 2.2e). The insertion of lithium and gradient in Li concentration within the particle, result in stresses that vary with position and time (Figs. 2.2f-h). As the concentration increases near the particle surface, the outer portion swells more than the material near the center of the particle, i.e., there is a mismatch in strain. Material with a lower Li concentration does not swell as much, constraining the material further out from swelling freely. This results in tensile stress near the center of the particle. The radial stress in the Si particle is always tensile, maximum at the center of the particle, and decreases to zero at the particle surface. The tangential stress is tensile at the center of the particle and compressive at the surface; it is equal to the radial stress at the center where the particle is in a state of hydrostatic tension and the magnitude is at maximum at the surface. The shear stress is zero at the center of the particle and increases with radius. When the rate of Li insertion rises, (Fig. 2.2b), lithium enters the particle at the surface significantly faster than it can diffuse through the particle, i.e. the process is reaction dominated. This causes the local concentration gradient and thus the mismatch in strain to increase. All three stresses peak together, shortly before the maximum current is reached, then decrease with continued Li insertion as the concentration becomes more uniform and strain mismatch within the particle decreases.

The influences of particle size and potential sweep rate on the maximum tensile tangential stress were studied. Figure 2.3 plots the maximum (over time and position) tensile tangential stress with and without surface stress effects as a function of particle size and potential sweep rate. For particles with $R_s \geq 200nm$, the surface stress effect does not influence the maximum stress level. A contour line of 1 GPa, corresponding to the lower limit for Si tensile failure stress, is seen to the right of the plot, and can be considered to separate two regions of a failure map. Points above and to the right of this line describe configurations that would be expected to fail while those below and

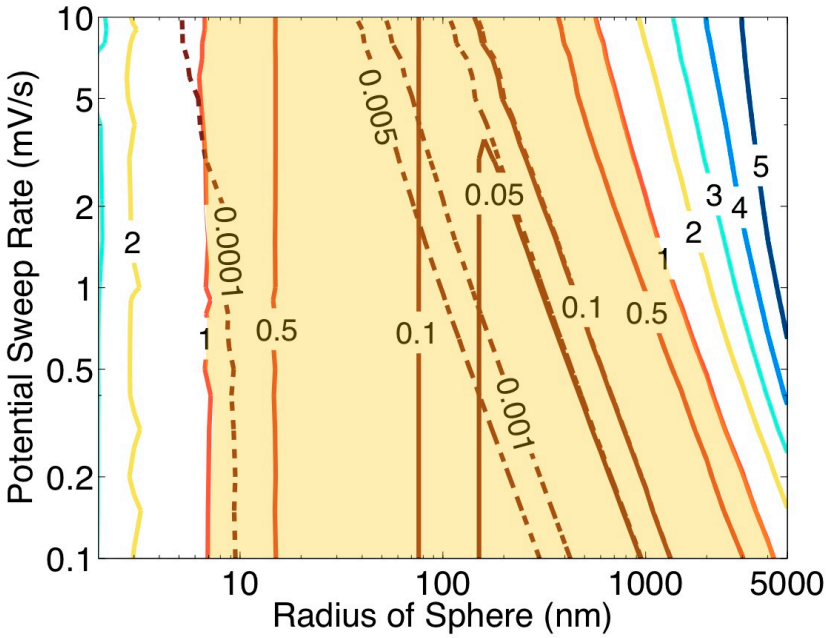

Figure 2.3: Predicted maximum stress levels upon Li insertion into Silicon particles as a function of particle size and sweep rate. Solid lines include the surface stress effect, dashed lines do not include this effect. Regions outside the highlighted section are expected to fail.

to the left of the line would be expected to be safe. When the surface stress effect is accounted for, the stresses increase with decreasing particle radii $\leq 200nm$. An additional contour at the 1 GPa level is seen on the left side of the plot where the maximum stress level is dominated by the surface stress. These results are consistent with experimental observations where smaller particles (in the larger nm-scale) have been shown to be more resistant to cracking than larger ones.[55] These results also suggest, as do experiments, that for high potential sweep rate applications, it is more important to use smaller particles than in low rate applications. These results are for the extreme case of a particle that is permitted to expand freely. The stresses are lower in the intermediate sized particles because the increased surface to volume ratio results in a more uniform lithium concentration throughout the particle; the lower concentration gradient results in lower stresses. For small-nm sized particles, the surface stress effect is dominant and the stresses increase. If the particle is constrained by a host matrix during insertion, the stresses will increase. Note, though, that this discussion and analysis, has not considered dependencies of the material parameters on

phase-changes in the silicon, Li concentration, nor stress levels in the particle. DeLuca, Maute, and Dunn[26] have performed follow up work focusing on the single scale silicon model.

Chapter 3

Design Optimization

The author's first publication (Appendix A) illustrated how several parameters, such as electrode porosity, electrode particle size, and discharge rate strongly affect the usable capacity and stress levels in the electrode particles of the battery. Additional parameters such as the electrode thickness and particle shape can also affect the electrochemical and mechanical performance of the battery. Balancing the electrochemical and mechanical phenomena in order to achieve a desired outcome can be done via a formal design optimization approach. Design optimization aims to improve an objective, such as increasing the capacity of the battery at a given discharge rate, while satisfying constraints, for example, placing limits on the maximum stress in the electrode particles. This chapter reviews previous work on design optimization of batteries and overviews the design optimization methodology developed and key contributions from the author's publications - Refs. [40, 41] (Appendices C and D).

3.1 Design Optimization of Lithium Batteries

Previous work on improving battery performance has been performed on both the cell and battery pack level. At the pack level, studies have focused on thermal [13, 81, 47, 50] and power management,[53] strategies. Cell level optimization studies are generally severely limited in number of design variables due to complexity and computational cost of the battery models.[69, 31, 12, 65, 64] Du *et al.*[31] used surrogate models to study the influence of parameters such as cycling rate and particle size on the specific energy and power of a battery cell identifying the Pareto-optimal

relationship between specific energy and power in the cell and quantified the cell performance in terms of the ratio of discharge time to diffusion time. Chen *et al.*[12] studied the relationship between electronic and ionic conductivities and the specific energy of the cathode. Srinivasan and Newman[69] increased the specific energy of an iron phosphate lithium-ion cell over a range of discharge rates through manipulation of the porosity and thickness of the cathode while maintaining the capacity ratio between the anode and cathode constant. This study employed the multi-scale porous electrode battery model described in Chapter 2 and parameter sweeps over the two design variables to determine optimal designs. The previous design studies above rely primarily on intuition, experience, and parameter sweeps, but do not employ directly a formal optimization approach for designing battery cells.

Ramadesigan *et al.*[65] employed a formal gradient-based design optimization method to reduce the Ohmic drop, thus increasing the capacity, of a cell by varying the porosity distribution in the cathode in five distinct regions (design variables). This study showed that formal design optimization can be used to improve battery performance but was limited in number of design variables due to the computational cost of the model. Follow up work by De *et al.*[25] utilized a reformulated version of this model with improved computational efficiency to optimize electrode thicknesses and porosities simultaneously for increased energy in the battery. Most recently, Xue *et al.*[80] presented a numerical framework to maximize cell energy density while satisfying requirements for specific power density for the porous electrode cell models[59, 36]. Twelve design variables were investigated, these included the cycling rate, electrode thicknesses, porosities, and particle sizes, separator thickness, cycling rate, and material properties of electrode diffusivity and conductivity. Optimization was performed via a gradient-based design optimization method; the gradients of the objective and constraints with respect to the design variables computed via a complex-step approximation method. This approach is computationally expensive, requiring $\sim$26 to 62 hours to converge depending on the power density requirement. Optimal results converged to the smallest electrode particle size and separator thickness.

In the author's work, the number of design variables is essentially unlimited due to the

development and use of a multi-scale adjoint sensitivity analysis method. This approach is flexible, allowing for different types of objectives, constraints, and types of design variables without compromising the accuracy of the overall model.

3.2 Gradient-Based Design Optimization With Adjoint Sensitivity Analysis

The optimization studies for batteries described in the previous section are limited in number of design variables due to the computational cost of the models used, specifically in the computation of the sensitivities of the objective and constraints to the design variables. The ability to include additional design variables allows for investigation of the interplay between multiple design variables and to fully resolve the shape of an optimal structure. In the author's work, a design optimization methodology with adjoint sensitivity analysis was developed to efficiently handle a large number of design variables.

Gradient-based design optimization is employed to minimize an objective, Z, subject to inequality constraints, $\mathcal{G}_j$, by varying continuous design variables, $\mathbf{s} \in \Re^{N_s}$:

$$\begin{aligned} \min_{\mathbf{s}} \; & Z(\mathbf{x},\mathbf{y},\mathbf{s}) = \int \mathcal{F}(\mathbf{x},\mathbf{y},\mathbf{s})\, dt \\ \text{s.t. } & \mathcal{G}_j(\mathbf{x},\mathbf{y},\mathbf{s}) = \int \mathcal{G}(\mathbf{x},\mathbf{y},\mathbf{s})\, dt \leq 0 \quad j = 1 : N_g \\ & s_i^L \leq s_i \leq s_i^U \quad i = 1 : N_s, \end{aligned} \tag{3.1}$$

where $\mathbf{x}$ represents the state variables and $\mathbf{y}$ the micro-scale state variables. The objective and constraints are differentiable functions that depend on both state and design variables. The time-integral formulation allows accounting for both average performance measures and quantities at distinct points in time. The lower and upper bounds for the optimization variables are denoted by s_i^L and s_i^U, respectively.

This design optimization problem is solved by a nonlinear programming method that requires the gradients of the objective and constraints with respect to the design variables.[72] The computational complexity of the multi-scale battery model and potentially large number of design variables necessitates the use of analytical sensitivities in which the sensitivities are calculated based on the

set of discrete solutions to the finite element problem. In Appendix C (Ref [41]) the derivation of the multi-scale, transient, adjoint sensitivity equations is presented. This formulation allows for optimization criteria which are electrochemical or mechanical in nature, and design variables that can include macro- and micro-scale criteria such as the local electrode porosity, electrode thickness, and local micro-scale particle size. The mathematical structure of the multi-scale transient, adjoint sensitivity equations allows for decomposing the fully coupled problem into multiple, independent, smaller problems at two scales. Therefore the proposed adjoint sensitivity analysis method is applicable to spatially and temporally well-resolved multi-scale problems with a large number of design variables. In Appendix C (Ref [41]), the computational savings of this adjoint sensitivity approach is compared to finite differencing. The sensitivities of an objective and 80 constraints to 120 design variables were calculated in 5 minutes as compared to $\sim$20 hours using numerical finite differencing. In Appendices C and D, this approach is used to maximize the capacity of a lithium battery by locally varying the porosities and particle radii in the electrodes.

Chapter 4

Conclusion and Future Work

This dissertation focused on understanding and simulating the interplay between electrochemical and mechanical phenomena in lithium batteries. A multi-scale model including electrochemical and mechanical effects was developed. Gradient-based design optimization was used to find optimal electrode structures to improve the performance of the battery through functionally graded electrodes. The first publication, Appendix A, extended an existing multi-scale, electrochemical battery model to include mechanical effects at both macro- and micro-scales. The second publication, Appendix B, focused on the micro-scale particle model as applied to silicon anodes. A subsequent study extended the model further to include surface stress effects, resulting in upper and lower bounds on particle size, Fig. 2.3. A gradient-based design optimization approach was employed to maximize the battery capacity. Development of multi-scale adjoint sensitivity equations in the third publication, Appendix C, allowed for an essentially unlimited number of design variables as compared to at most 12 design variables studied in previous battery optimization studies[80]. This design optimization approach was used in the last publication, Appendix D, to maximize the usable capacity of the battery over a range of discharge rates while limiting stress levels in the electrode particles. Results showed that the highest rate discharge drives the design which is dominated by Li^+ transport rates. Results showed an improvement of up to 61% relative to the initial design by manipulating the local electrode porosity and particle radii. These results illustrate the utility of computational design optimization as an efficient tool to aid in battery design.

Future work can be broadly divided into extensions of the multiscale battery model and ad-

ditional optimization studies. Inclusion of thermal effects [54], SEI layer formation[68, 18], and additional degradation from side reactions[19] will affect the electrochemical and mechanical performance of the battery. The model is limited by lack of data for the dependence of material properties on concentration profiles and stress state[63], and exclusion of more complex phenomena such as non-Fickian diffusion, the effects of chemical potential on stress, finite strains, and large plastic deformations[10, 85, 24]. These phenomena could be incorporated into this modeling framework. Additionally, studying the effect of electrochemical cycling and including the dependence of the macro-scale porosity on the swelling of the electrode particles with lithium insertion is recommended. Recommended future optimization studies include: incorporation of a broader range of design variables, such as electrode thicknesses and material properties; investigation of faster discharge rates; and inclusion of cycling and degradation effects. Design optimization could also be employed to determine optimal charging profiles in which the charge rate varies with time depending on the state of charge of the battery. Additionally, this approach also be employed to curve-fit simulated discharge curves to experimental results to assist in determining material properties.

Bibliography

[1] K.E. Aifantis and J.P. Dempsey. Stable crack growth in nanostructured li-batteries. Journal of Power Sources, 143(1):203–211, 2005.

[2] K.E. Aifantis and S.A. Hackney. An ideal elasticity problem for li-batteries. J Mech Behav Mater, 14:41327, 2003.

[3] K.E. Aifantis, S.A. Hackney, and J.P. Dempsey. Design criteria for nanostructured li-ion batteries. Journal of Power Sources, 165(2):874 – 879, 2007.

[4] Pankaj Arora, Marc Doyle, Antoni S. Gozdz, Ralph E. White, and John Newman. Comparison between computer simulations and experimental data for high-rate discharges of plastic lithium-ion batteries. Journal of Power Sources, 88:219–231, 2000.

[5] Loic Baggetto, Rogier A. H. Niessen, Fred Roozeboom, and Peter H. L. Notten. High energy density all-solid-state batteries: A challenging concept towards 3d integration. Adv. Funct. Mater., 18:10571066, 2008.

[6] Allen J. Bard and Larry R. Faulkner. Electrochemical Methods. John Wiley and Sons, Inc, 2 edition, 2001.

[7] Y. Benveniste. A new approach to the application of mori-tanakas theory in composite materials. Mech. Materials, 6:147–157, 1987.

[8] Y. Benveniste and GJ Dvorak. On a correspondence between mechanical and thermal effects in two-phase composites. In Micromechancis and Inhomogeneity. Springer, New York, 1990.

[9] Gerardine G. Botte, Venkat R. Subramanian, and R. E. White. Mathematical modeling of secondary lithium batteries. Electrochimica Acta, 45(15-16):2595–2609, 2000.

[10] A.F. Bower, P.R. Guduru, and V.A. Sethuraman. A finite strain model of stress, diffusion, plastic flow, and electrochemical reactions in a lithium-ion half-cell. Journal of the Mechanics and Physics of Solids, 59:804–828, 2011.

[11] Candace K. Chan, Hailin Peng, Gao Liu, Kevin McIlwrath, Xiao Feng Zhang, Robert A. Huggins, and Yi Cui. High-performance lithium battery anodes using silicon nanowires. Nature Nanotechnology, 3:31–35, 2008.

[12] Y.-H. Chen, C. W. Wang, X. Zhang, and Ann Marie Sastry. Porous cathode optimization for lithium cells: Ionic and electronic conductivity, capacity, and selection of materials. Journal of Power Sources, 195:2851–2862, 2010.

[13] Yufei Chen and James W. Evans. Thermal analysis of lithium polymer electrolyte batteries by a two dimensional model–thermal behaviour and design optimization. Electrochimica Acta, 39(4):517 – 526, 1994.

[14] Y. T. Cheng and Mark W. Verbrugge. The influence of surface mechanics on diffusion induced stresses within spherical nanoparticles. Journal of Applied Physics, 104(8):083521, 2008.

[15] Yang-Tse Cheng and Mark W. Verbrugge. Evolution of stress within a spherical insertion electrode particle under potentiostatic and galvanostatic operation. Journal of Power Sources, 190(2):453–460, 2009.

[16] Timothy E. Chin, Urs Rhyner, Yukinori Koyama, Steven R. Hall, and Yet-Ming Chiang. Lithium rechargeable batteries as electromechanical actuators. Electrochemical and Solid-State Letters, 9:A134–A138, 2006.

[17] Thomas Christen and Martin W. Carlen. Theory of ragone plots. Journal of Power Sources, 91(2):210 – 216, 2000.

[18] John Christensen and John Newman. A mathematical model for the lithium-ion negative electrode solid electrolyte interphase. Journal of The Electrochemical Society, 151(11):A1977–A1988, 2004.

[19] John Christensen and John Newman. Cyclable lithium and capacity loss in li-ion cells. Journal of the Electrochemical Society, 152(4):818–829, 2005.

[20] John Christensen and John Newman. A mathematical model of stress generation and fracture in lithium manganese oxide. Journal of the Electrochemical Society, 153(6):1019–1030, 2006.

[21] John Christensen and John Newman. Stress generation and fracture in lithium insertion materials. Journal of Solid State Electrochemistry, 10(5):293–319, 2006.

[22] R. F. Cook. Strength and sharp contact fracture of silicon. J. Mater. Sci., 141:841–872, 2006.

[23] Li-Feng Cui, Riccardo Ruffo, Candace K. Chan, Hailin Peng, and Yi Cui. Crystalline-amorphous coreshell silicon nanowires for high capacity and high current battery electrodes. Nano Letters, 9(1):491–495, 2009.

[24] Zhiwei Cui, Feng Gao, and Jianmin Qu. A finite deformation stress-dependent chemical potential and its applications to lithium ion batteries. Journal of the Mechanics and Physics of Solids, 60:1280–1295, 2012.

[25] Sumitava De, Paul W.C. Northrop, Venkatasailanathan Ramadesigan, and Venkat R. Subramanian. Model-based simultaneous optimization of multiple design parameters for lithium-ion batteries for maximization of energy density. Journal of Power Sources, 227(0):161–170, 2013.

[26] Christopher M DeLuca, Kurt Maute, and Martin L. Dunn. Effects of electrode particle morphology on stress generation in silicon during lithium insertion. Journal of Power Sources, 196(22):9672–9681, 2011.

[27] Rutooj Deshpande, Mark Verbrugge, Yang-Tse Cheng, John Wang, and Ping Liu. Battery cycle life prediction with coupled chemical degradation and fatigue mechanics. Journal of the Electrochemical Society, 159(10):A1730–A1738, 2012.

[28] Marc Doyle. Design and Simulation of Lithium Rechargeable Batteries. PhD thesis, University of California, Berkeley, 1995.

[29] Marc Doyle, Thomas F. Fuller, and John Newman. Modeling of galvanostatic charge and discharge of the lithium/polymer/insertion cell. Journal of the Electrochemical Society, 140(6):1526–33, June 1993.

[30] Marc Doyle and John Newman. The use of mathematical modeling in the design of lithium/polymer battery systems. Electrochimica Acta, 40:2191–2196, 1995.

[31] W. Du, A. Gupta, X. Zhang, and Ann Marie Sastry. Effect of cycling rate, particle size and transport properties on lithium-ion cathode performance. International Journal of Heat and Mass Transfer, 53:3552–3561, 2010.

[32] Frédéric Feyel. Multiscale fe2 elastoviscoplastic analysis of composite structures. Computational Materials Science, 16(1-4):344–354, 1999.

[33] Frédéric Feyel. A multilevel finite element method (fe2) to describe the response of highly non-linear structures using generalized continua. Computer Methods in Applied Mechanics and Engineering, 192(28-30):3233–3244, 2003.

[34] Frédéric Feyel and Jean-Louis Chaboche. Fe2 multiscale approach for modelling the elasto-viscoplastic behaviour of long fibre sic/ti composite materials. Computer Methods in Applied Mechanics and Engineering, 183(3-4):309–330, 2000.

[35] Thomas F. Fuller, Marc Doyle, and John Newman. Relaxation phenomena in lithium-ion-insertion cells. J. Electrochem. Soc., 141(4):982–990, April 1994.

[36] Thomas F. Fuller, Marc Doyle, and John Newman. Simulation and optimization of the dual lithium ion insertion cell. Journal of the Electrochemical Society, 141(1):1–10, 1994.

[37] R. Edwin Garcia and Yet-Ming Chiang. Spatially resolved modeling of microstructurally complex battery architectures. Journal of the Electrochemical Society, 154(9):856–864, 2007.

[38] R. Edwin Garcia, Yet-Ming Chiang, W. Craig Carter, Pimpa Limthongkul, and Catherine M. Bishop. Microstructural modeling and design of rechargeable lithium-ion batteries. Journal of the Electrochemical Society, 152(1):255–263, 2005.

[39] Stephanie Golmon, Kurt Maute, and Martin L. Dunn. Numerical modeling of electrochemical-mechanical interactions in lithium polymer batteries. Computers & Structures, 87(23-24):1567 – 1579, 2009.

[40] Stephanie Golmon, Kurt Maute, and Martin L. Dunn. Multi-scale design optimization of lithium batteries using adjoint sensitivity analysis. International Journal for Numerical Methods in Engineering, 92(5):475–494, April 2012.

[41] Stephanie Golmon, Kurt Maute, and Martin L. Dunn. A design optimization methodology for li^+ batteries. Journal of Power Sources, in press, corrected proof 2013.

[42] Stephanie Golmon, Kurt Maute, Se-Hee Lee, and Martin L. Dunn. Stress generation in silicon particles during lithium insertion. Applied Physics Letters, 97(3), 2010.

[43] Mino Green, Elizabeth Fielder, Bruno Scrosati, Mario Wachtler, and Judith Serra Moreno. Structured silicon anodes for lithium battery applications. Electrochemical and Solid-State Letters, 6(5):A75–A79, 2003.

[44] W. B. Gu and C. Y. Wang. Thermal-electrochemical modeling of battery systems. Journal of The Electrochemical Society, 147(8):2910–2922, 2000.

[45] W.B. Gu, C.Y. Wang, S.M. Li, M.M. Geng, and B.Y. Liaw. Modeling discharge and charge characteristics of nickel-metal-hydride batteries. Electrochimica Acta, 44(25):4525 – 4541, 1999.

[46] R.A. Huggins and W.D. Nix. Decrepitation model for capacity loss during cycling of alloys in rechargeable electrochemical systems. Solid State Ionics, 6:57–63, 2000.

[47] Anthony Jarrett and Il Yong— Kim. Design optimization of electric vehicle battery cooling plates for thermal performance. Journal of Power Sources, 196(23):10359–10368, 2011.

[48] P. Kanouté, D. Boso, J. Chaboche, and B. Schrefler. Multiscale methods for composites: A review. Archives of Computational Methods in Engineering, 16:31–75, 2009.

[49] Uday Kasavajjula, Chunsheng Wang, and A. John Appleby. Nano- and bulk-silicon-based insertion anodes for lithium-ion secondary cells. Journal of Power Sources, 163(2):1003 – 1039, 2007.

[50] Gi-Heon Kim, A. Pesaran, and R. Spotnitz. A three-dimensional thermal abuse model for lithium-ion cells. J. Power Sources (Switzerland), 170(2):476–89, 2007.

[51] Gi-Heon Kim, Kandler Smith, Kyu-Jin Lee, Shriram Santhanagopalan, and Ahmad Pesaran. Multi-domain modeling of lithium-ion batteries encompassing multi-physics in varied length scales. Journal of the Eletrochemical Society, 158(8):A995 – A969, 2011.

[52] Hyunjung Kim, Byunghee Han, Jaebum Choo, and Jaephil Cho. Three-dimensional porous silicon particles for use in high-performance lithium secondary batteries. J. Angew. Chem., Int. Ed., 47:10151–10154, 2008.

[53] Min-Joong Kim and Huei Peng. Power management and design optimization of fuel cell/battery hybrid vehicles. Journal of Power Sources, 165(2):819 – 832, 2007.

[54] Karthikeyan Kumaresan, Godfrey Sikha, and Ralph E. White. Thermal model for a li-ion cell. Journal of The Electrochemical Society, 155(2):A164–A171, 2008.

[55] Hong Li, Xuejie Huang, Liquan Chen, Zhengang Wu, and Yong Liang. A high capacity nano-si composite anode material for lithium rechargeable batteries. Electrochemical and Solid-State Letters, 2(11):547–549, 1999.

[56] Christian Miehe, J. Schotte, and M. Lambrecht. Homogenization of inelastic solid materials at finite strains based on incremental minimization principles. application to the texture analysis of polycrystals. Journal of the Mechanics and Physics of Solids, 50(10):2123–2167, 2002.

[57] Christian Miehe, Jörg Schröder, and Jan Schotte. Computational homogenization analysis in finite plasticity simulation of texture development in polycrystalline materials. Computer Methods in Applied Mechanics and Engineering, 171(3-4):387–418, 1999.

[58] T. Mori and K. Tanaka. Average stress in matrix and average elastic energy of materials with misfitting inclusions. Acta Metallurgica, 21:571–574, 1973.

[59] John Newman and Karen E. Thomas. Electrochemical Systems. Wiley-Interscience, 3 edition, 2004.

[60] T. Pereira, R. Scaffaro, Z. Guo, S. Nieh, J. Arias, and H.T. Hahn. Performance of thin-film lithium energy cells under uniaxial pressure. Advaned Engineering Materials, 10(4):393–9, 2008.

[61] T. Pereira, R. Scaffaro, S. Nieh, J. Arias, Z. Guo, and H.T. Hahn. The performance of thin-film li-ion batteries under flexural deflection. Journal of Micromechanics and Microengineering, 16:2714–21, 2006.

[62] Tony Pereira, Zhanhu Guo, S. Nieh, J. Arias, and H. Thomas Hahn. Embedding thin-film lithium energy cells in structural composites. Composites Science and Technology, 68:1935–41, 2008.

[63] Yue Qi and Stephen J. Harris. In situ observation of strains during lithiation of a graphite electrode. Journal of the Eletrochemical Society, 157(6):A741 – A747, 2010.

[64] Saeed Khaleghi Rahimian, Sean Rayman, and Ralph E. White. Optimal charge rates for a lithium ion cell. Journal of Power Sources, 196:10297–10304, 2011.

[65] Venkatasailanathan Ramadesigan, Ravi N. Methekar, Folarin Latinwo, Richard D. Braatz, and Venkat R. Subramanian. Optimal porosity distribution for minimized ohmic drop across a porous electrode. Journal of The Electrochemical Society, 157(12):A1328–A1334, 2010.

[66] Patrice Simon and Yury Gogotsi. Materials for electrochemical capacitors. Nat Mater, 7(11):845–854, 11 2008/11//print.

[67] A. J. Smith, J. C. Burns, S. Trussler, and J. R. Dahn. Precision measurements of the coulombic efficiency of lithium-ion batteries and of electrode materials for lithium-ion batteries. Journal of The Electrochemical Society, 157(2):A196–A202, 2010.

[68] R. Spotnitz. Simulation of capacity fade in lithium-ion batteries. J. Power Sources (Switzerland), 113(1):72–80, 2003.

[69] Venkat Srinivasan and John Newman. Design and optimization of a natural graphite/iron phosphate lithium-ion cell. Journal of the Electrochemical Society, 151(10):1530–1538, 2004.

[70] David E. Stephenson, Erik M. Hartman, John N. Harb, and Dean R. Wheeler. Modeling of particle-particle interactions in porous cathodes for lithium-ion batteries. Journal of The Electrochemical Society, 154(12):A1146–A1155, 2007.

[71] Wan Suwito, Martin L. Dunn, Shawn J. Cunningham, and David T. Read. Elastic moduli, strength, and fracture initiation at sharp notches in etched single crystal silicon microstructures. Journal of Applied Physics, 85(7):3519–3534, 1999.

[72] Krister Svanberg. A class of globally convergent optimization methods based on conservative convex separable approximations. SIAM J. on Optimization, 12(2):555–573, 2002.

[73] J.P. Thomas and M.A. Qidwai. The design and application of multifunctional structure-battery materials systems. JOM, pages 18–24, March 2005.

[74] Karen E. Thomas and John Newman. Thermal modeling of porous insertion electrodes. Journal of the Electrochemical Society, 150(2):176–92, 2003.

[75] Chia-Wei Wang and Ann Marie Sastry. Mesoscale modeling of a li-ion polymer cell. Journal of the Electrochemical Society, 154(11):1035–1047, 2007.

[76] Deyu Wang, Xiaodong Wu, Zhaoxiang Wang, and Liquan Chen. Cracking causing cyclic instability of lifepo4 cathode material. Journal of Power Sources, 140(1):125–128, 2005.

[77] Haifeng Wang, Young-Il Jang, Biying Huang, Donald R. Sadoway, and Yet-Ming Chiang. Tem study of electrochemical cycling-induced damage and disorder in licoo[sub 2] cathodes for rechargeable lithium batteries. Journal of The Electrochemical Society, 146(2):473–480, 1999.

[78] K. West, T. Jacobsen, and S. Atlung. Modeling of porous insertion electrodes with liquid electrolyte. J. Electrochem. Soc., 129(7):1480–1485, July 1982.

[79] Martin Winter and Ralph J. Brodd. What are batteries, fuel cells, and supercapacitors? Chemical Reviews, 104(10):4245–4269, 2004.

[80] Nansi Xue, Wenbo Du, Amit Gupta, Wei Shyy, Ann Marie Sastry, and Joaquim R. R. A. Martins. Optimization of a single lithium-ion battery cell with a gradient-based algorithm. Journal of The Electrochemical Society, 160(8):A1071–A1078, 2013.

[81] Li-Jun Yu, Ming-Jun Qin, Peng Zhu, and Li Yang. Numerical simulation and optimization of nickel-hydrogen batteries. Journal of Power Sources, 179(2):848 – 853, 2008.

[82] Dong Zhang, Branko N. Popov, and Ralph E. White. Modeling lithium intercalation of a single spinel particle under potentiodynamic control. Journal of The Electrochemical Society, 147(3):831–838, 2000.

[83] Xiangchun Zhang, Ann Marie Sastry, and Wei Shyy. Intercalation-induced stress and heat generation within single lithium-ion battery cathode particles. Journal of the Electrochemical Society, 155(7):542–52, 2008.

[84] Xiangchun Zhang, Wei Shyy, and Ann Marie Sastry. Numerical simulation of intercalation-induced stress in li-ion battery electrode particles. Journal of the Electrochemical Society, 154(10):910–916, 2007.

[85] Kejie Zhao, Matt Pharr, Shengqiang Cai, Joost J. Vlassak, and Zhigang Suo. Large plastic deformation in high-capacity lithium-ion batteries caused by charge and discharge. Journal of the American Ceramic Society, 94(S1):S226–S235, 2011.

Appendix A

Publication: Numerical modeling of electrochemical-mechanical interactions in lithium polymer batteries

Computers and Structures 87 (2009) 1567–1579

Contents lists available at ScienceDirect

Computers and Structures

journal homepage: www.elsevier.com/locate/compstruc

Numerical modeling of electrochemical–mechanical interactions in lithium polymer batteries

Stephanie Golmon [a], Kurt Maute [a,*], Martin L. Dunn [b]

[a] Department of Aerospace Engineering, University of Colorado, Boulder, CO, United States
[b] Department of Mechanical Engineering, University of Colorado, Boulder, CO, United States

ARTICLE INFO

Article history:
Received 9 January 2009
Accepted 3 August 2009
Available online 5 September 2009

Keywords:
Multi-scale modeling
Finite element method
Homogenization
Porous electrode theory

ABSTRACT

This paper presents a multi-scale finite element approach for lithium batteries to study electrochemical–mechanical interaction phenomena at macro- and micro-scales. The battery model consists of a lithium foil anode, a separator, and a porous cathode that includes solid active materials and a liquid electrolyte. We develop a multi-scale approach to analyze the surface kinetics and electrochemical–mechanical phenomena within a single spherical particle of the active material. Homogenization techniques relate parameters in the micro-scale particle model to those in the macro-scale model describing the lithium ion transport, electric potentials and mechanical response based on porous electrode theory.

1. Introduction

Today, lithium batteries have the highest energy storage density of any secondary (rechargeable) battery technology [1]. However, their current use is limited to relatively low power applications such as cell phones and other small, portable electronics. Electrical systems requiring high voltages and/or currents such as battery packs in hybrid-electric vehicles still use traditional, heavy, lead-acid battery technology due to lower cost, longer lifetimes, and increased safety as failure in lithium batteries can be dramatic such as the laptop battery fires that occurred recently. Failure can be due to thermal runaway, internal shorting, and mechanical degradation of the electrodes. Lithium rechargeable batteries suffer in particular from a limited lifetime in comparison to other rechargeable chemistries, being limited to 100–150 charge–discharge cycles versus the 300 cycles achieved by other technologies [1]. This shortened lifecycle is due to deposits formed on the surface of the electrode during cycling [1], and possibly due to mechanical degradation of the electrode particles [2]. To understand the latter degradation phenomena, modeling and predicting the stresses in the electrode particles due to external mechanical loads and internal chemical processes is needed. The importance of understanding the interaction between chemical and mechanical phenomena in batteries is further highlighted when incorporating lithium batteries into structural composites to increase their storage-to-weight ratio. Such concepts have recently been advocated for aerospace systems dominated by weight constraints [3]. However, embedding a battery into a composite induces mechanical loads on the battery during manufacturing and operation.

In order to address the concerns of the relatively short lifecycle and safety problems in lithium batteries as well as to integrate batteries into structural composites, detailed understanding and mathematical modeling of the electrochemical and mechanical behavior and failure mechanisms of the batteries are needed. Balancing the trade-offs between structural and electrochemical performance is requisite in order to achieve these goals. To this end, in this paper we develop a coupled mathematical model of electrochemical and mechanical effects in lithium batteries.

The mechanisms causing capacity fade and failure of lithium batteries were studied by Wang et al. [2] who experimentally showed that capacity fade of lithium batteries after 60 cycles is linked to crack growth in the electrode. Wang et al. [4] found for $LiCoO_2$ cathodes that the active material particles are not uniformly strained during cycling and that the cycling can lead to fracture of the particles. Additional work on manganese cathodes has been performed by Thackeray et al. [5] and Aifantis and Hackney [6]. Several studies have focused on modeling the stress and crack formation in a single electrode particle. Huggins and Nix [7] developed a one-dimensional model to predict stresses and fracture in electrodes undergoing volume changes. Their model predicts a terminal particle size below which particles are not expected to crack. Aifantis and Dempsey [8] have modeled the crack formation in electrodes using facture mechanics. Christensen and Newman [9] predicted for a single spherical particle stress generation and

* Corresponding author. Address: Department of Aerospace Engineering Sciences, University of Colorado, CB 429, Boulder, CO 80301-0429, United States. Tel.: +1 303 735 2103; fax: +1 303 492 4990.
E-mail address: maute@colorado.edu (K. Maute).

0045-7949/$ - see front matter © 2009 Elsevier Ltd. All rights reserved.
doi:10.1016/j.compstruc.2009.08.005

fracture in lithium insertion compounds finding that particles are more likely to fracture when used in high-power applications. Christensen and Newman [10] also modeled the effects for a spherical particle of lithium manganese oxide, predicting that the intercalation-induced stress can exceed the strength of the particles. Aifantis et al. [11] used fracture mechanics to predict when an electrode particle will fracture, finding that smaller particles are preferable. Zhang et al. [12] studied intercalation-induced stress in $LiMn_2O_4$ particles, treating the intercalation-induced stress analogously to thermal stress and extending the spherical model to ellipsoidal particles.

Only few experimental studies incorporating batteries into structures and studying the effect of external mechanical loads have been performed. Thomas and Qidwai [3] have placed commercial lithium batteries in the wings of microair vehicles (MAV) resulting in improved range of the MAV. In their mechanical model of structurally integrated batteries, Thomas and Qidwai [3] assumed that the effects of electrochemical–mechanical interactions are negligible. Pereira et al. have studied experimentally the effects of flexural deflection [13] and uniaxial pressure [14] on lithium thin film batteries. Their observations suggest that up until structural failure of the battery, the electrochemical performance of the battery is not significantly affected by external mechanical loads. The same authors showed in a subsequent paper [15] that the same batteries could be successfully incorporated into a carbon fiber composite lay-up without degrading the battery performance and improving the mechanical properties of the composite. Much of the previous work on modeling lithium batteries has focused solely on electrochemical phenomena such as in the work of West et al. [16] and Doyle et al. [17] who model a porous electrode and in the work of Wang and Sastry [18] where the cathode microstructure is modeled. Garcia et al. [19,20] include mechanical effects in their model and study the performance of various nano-structured electrode layouts using dilute solution theory.

The goal of this study is to develop a numerical model to predict the electrochemical–mechanical interactions in structurally integrated lithium batteries subject to external mechanical loads, in order to understand and quantify the effects of electrochemical and mechanical parameters on performance and eventually, on failure mechanisms in these batteries. Resolving directly all length scales involved in the analysis of a battery, in particular modeling every cathode particle individually, leads to an impractical computational burden. Therefore, our approach is based on porous electrode theory and a multi-scale finite element formulation.

1.1. Electrochemical–mechanical interaction

When discharging a battery, electrons flow from the anode through an external electrical circuit and back to the cathode. The electric work done in the circuit leads to a drop in the electrical potential difference between the anode and cathode. A simple layout of a lithium battery includes a negative (anodic) current collector, a lithium foil anode, a gel or liquid electrolyte, a porous intercalation cathode, and a positive (cathodic) current collector. The external positive and negative terminals are connected to the current collectors. The cathode consists of two phases, a porous solid, active material and a liquid electrolyte that fills the pores. In the simplest case, the anode is a lithium foil while in modern batteries and secondary (rechargeable) batteries porous graphitic intercalation compounds are used as anode material systems. Research is ongoing to develop anodes with larger storage capacity. For the case of a porous anode, the anode is modeled the same way as the cathode. This model can be applied to any battery system that uses a single electrolyte. To structurally integrate the battery, it is sandwiched between two structural layers which results in an interlaminate stress applied to the battery. A representative configuration of a structurally integrated battery is depicted in Fig. 1.

When an external electrical load is applied, lithium (Li) is oxidized into Li^+ ions and electrons at the anode–separator interface, Γ_{AS}. The electrons flow through the current collector and the external circuit back to the positive current collector and into the cathode active material. Meanwhile, the Li^+ ions enter the solution phase of the separator and are carried by migration and diffusion across the separator–cathode interface, Γ_{SC}, to the cathode active material. At the surface of the active material particles, Li^+ ions are reduced and neutral Li diffuses into the cathode particles. To charge a secondary lithium battery, these processes reverse. As Li intercalates into the cathode active material particles, the particles swell resulting in both particle- and battery-level strains and stresses; for the Mn_2O_4 cathode discussed in this paper, the particles can swell up to 6.5% [12]. External mechanical loads also cause battery- and particle-level stresses and affect the uptake of Li by the particles in the cathode.

1.2. Proposed model

In this study we present a numerical approach for modeling the electrochemical–mechanical interactions in lithium batteries. To design and predict the performance of batteries subject to external

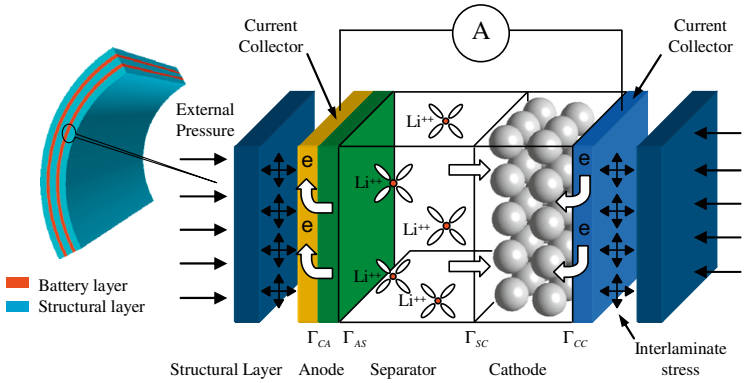

Fig. 1. Schematic of a structurally integrated lithium battery.

mechanical loads, our model accounts for the influence of electrochemical parameters such as discharge rate, liquid volume fraction in the cathode, active material particle size, and mechanical boundary conditions from the interlaminate stress, on both electrochemical and mechanical performance. This model predicts the effects of external loads and allows one to assessing the trade-offs between integration versus non-integration of the battery into a structural composite as well as suggest ways to improve overall battery design.

As the performance of lithium batteries involves multiple length scales, our approach is based on a multi-scale finite element formulation of the electrochemical–mechanical interactions. At the battery-level, or macro-scale, we model the Li^+ ion movement within the electrolyte and the resulting current and potential of the electrolyte, the potential of the solid cathode material, and the battery-level deformations. Within the cathode region, there are both solid active material and liquid electrolyte phases. Rather than modeling every individual cathode particle and the interactions between these particles, we analyze a representative single active material particle wherever information about the active material is needed in the macro-scale problem. We refer to this single particle model as the micro-scale. We model the lithium concentration throughout the particle, the stress state, and the displacements within the particle. Our numerical framework is based on an implicit Euler backward scheme and a Galerkin finite element model to discretize the macro- and micro-scale processes in time and space. Homogenization is used to relate the processes at the macro- and micro-scales.

The reminder of this paper is organized as follows: first we present a mathematical model of a lithium battery at multiple length scales and describe its numerical implementation for a one-dimensional macroscopic battery model. We verify our numerical framework by comparison with previous, experimentally verified, mathematical models. Lastly, we present results for the electrochemical and mechanical effects of varying the discharge current density, the active material particle radius, the volume fraction in the porous electrode, and the external mechanical boundary conditions due to interlaminate stress. For convenience, a list of all symbols used in this paper is provided in Appendix A.

2. Numerical modeling of batteries

Numerical models predicting the transport and reaction processes in batteries have been presented by Doyle et al. [17] who modeled the electrochemical phenomena using porous electrode theory and a finite-volume method. These models have shown good agreement with experimental discharge experiments but do not account for mechanical effects in the battery. Garcia et al. [19] developed a two-dimensional micro-scale model describing the mechanical effects of discharging and charging a battery based on dilute solution theory. The model is solved using a finite element scheme in space and a finite difference scheme in time. Initially, Garcia et al. [19] included only the separator and cathode; later Garcia and Chiang [20] extended this model and included an intercalation anode as well. Different nanostructures for the electrodes were investigated showing that the shorter the distance between the electrodes, the better the battery performs.

Wang and Sastry [18] developed a three-dimensional micro-scale model predicting the electrochemical performance of batteries with random and periodic micro-scale cathode layouts by modeling every cathode particle. Stress effects, both internal and external, are not included in this model. Zhang et al. [12] accounted for the effects of internal stresses due to lithium intercalation for single active material particles but ignore possible surface traction due to constraint by the surrounding aggregate in the electrode and/or due to external mechanical loads. They considered both spherical and ellipsoidal particles and showed that for spherical particles, larger particle size and discharge currents result in higher stress; and for ellipsoidal particles, large aspect ratios decrease the intercalation-induced stress for particles of a constant volume. Recently, Zhang et al. [21] extended their particle model to include heat generation during charge and discharge; resistive heating was found to be the most significant heat generation source at the particle-level.

2.1. Multi-scale modeling of structurally integrated batteries

The electrochemical and mechanical performance of Li batteries strongly depends on the interaction between macro-scale and micro-scale phenomena, in particular within the porous cathode. However, directly resolving all scales and modeling all particles in the cathode is not practical. Instead we incorporate the micro-scale effects into the macro-scale problem through homogenization approaches and constitutive models that are derived from homogenization methods. Three length scales can be distinguished: at the *macro-scale*, transport processes and mechanical deformations in the entire battery layer are modeled; at the *micro-scale*, a single active material particle in the cathode is modeled; and at the *meso-scale*, homogenization methods based on particle aggregates relate the micro- and macro-scales.

Our macro-scale model is based on porous electrode theory [22,23] and concentrated solution theory [22,23] predicting electrochemical processes in the separator and cathode. With porous electrode theory, the cathode is treated as a superposition of two continuous phases—the solid material including the active material, binders and conductive additives, and the pore-filling liquid electrolyte. The liquid volume fraction of the cathode is called the porosity, ε, ($\varepsilon = V_l/V$). In the separator region of the battery there is no solid phase, so $\varepsilon = 1$. We extend the porous electrode theory to account for elastic and inelastic deformations due external loads and electrochemical eigenstrains. In this study, we do not model the structural layers surrounding the battery, and instead apply generic mechanical boundary conditions that with proper interpretation can be taken to represent the effect of the surrounding layers. We also assume that the lithium foil anode is perfectly rigid and therefore only model the separator and cathode regions. At the micro-scale, a single particle is modeled based on the work of Zhang et al. [12]. To relate the micro- and macro-scales, meso-scale homogenization methods are used.

The macroscopic response is characterized by the Li^+ ion concentration in the liquid phase, c_l, the electric potential of the liquid phase, ϕ_2, the electric potential of the solid phase, ϕ_1, and the macroscopic displacements, $\mathbf{u}$. The intercalation of Li^+ ions from the electrolyte into the particles is represented by an effective macroscopic pore wall flux, j_{eff}. The associated swelling of the particles results in a macroscopic electrochemical eigenstrain $\mathbf{e}^{ch}$.

At the micro-scale, a single representative active material particle is examined. The micro-scale variables include the microscopic lithium concentration in the particle, c_s, the microscopic displacements, u, and the hydrostatic stress field, σ_h. The rate of diffusion into the particle and subsequent particle swelling depends on the microscopic pore wall flux, j_s and the mechanical surface traction on the particle, P_s.

At the meso-scale, homogenization methods are used to relate the macroscopic and microscopic variables. The micro-scale pore wall flux, j_s, is dependent on the macro-scale variables, c_l, ϕ_1, and ϕ_2 and the micro-scale Li concentration at the particle surface, $c_{s,surf}$, through a micro-scale surface kinetics model. The micro-scale surface pressure exerted on the particle surface, P_s, is dependent on the macro-scale and micro-scale displacements, $\mathbf{u}$, and u through meso-scale homogenization of the mechanical variables.

The macro-scale effective pore wall flux, j_{eff}, is dependent on the micro-scale pore wall flux, j_s, through meso-scale homogenization of the electrochemical variables. The macro-scale chemically induced eigenstrain, $\mathbf{e}^{ch}$, is dependent on both the macro-scale displacement, $\mathbf{u}$, and micro-scale displacements, u through meso-scale homogenization of the mechanical variables. The interdependency between macro- and micro-scale variables is illustrated in Fig. 2. Note that the micro-scale boundary conditions for the micro-scale model depend on both macro- and micro-scale variables.

2.2. Macro-scale equations

The electrochemical transport of Li^+ ions through the electrolyte and the current carried by the solid and liquid phases are described by three equations:

$$\varepsilon\frac{\partial c_l}{\partial t}+\nabla\cdot\mathbf{N}+\frac{1}{F}\frac{\partial t_+^0}{\partial c_l}\mathbf{i}_2\cdot\nabla c_l-(1-t_+^0)j_{eff}=0 \tag{1}$$

$$\nabla\cdot\mathbf{i}_1+F\,j_{eff}=0 \tag{2}$$

$$\nabla\cdot\mathbf{i}_2-F\,j_{eff}=0 \tag{3}$$

with the following constitutive equations:

$$\mathbf{N}=-D_{eff}\nabla c_l \tag{4}$$

$$\mathbf{i}_1=-\lambda\nabla\phi_1 \tag{5}$$

$$\mathbf{i}_2=-\kappa_{eff}\left[\nabla\phi_2-\frac{RT}{F}(1-t_+^0)\nabla\ln c_l\right] \tag{6}$$

Eq. (1) describes the transport of Li^+ ions through the electrolyte with $\mathbf{N}$ being the Li^+ ion flux. Faraday's constant is denoted by F. The ions are carried by both migration and diffusion effects. This equation includes two source terms to account for the migration due to the current $\mathbf{i}_2$ carried by the electrolyte and for the effect of Li ions leaving the electrolyte and intercalating into the solid material. The transference number, t_+^0, is the percentage of the current in the solution carried by the Li^+ ion rather than the anions in solution; the transference number is in general a function of the lithium ion concentration, c_l. As Li^+ ions leave the electrolyte and enter the solid material, this creates an effective pore wall flux, j_{eff}. The currents $\mathbf{i}_1$ and $\mathbf{i}_2$ in the solid and liquid phases are governed by Eqs. (2) and (3) with source terms to account for the effects of Li entering and exiting the phases. In the solid phase, Ohm's law (5) relates the current and electric potential. In the liquid phase, the constitutive relationship is defined by a modified Ohm's law (6) that accounts for the effect of Li^+ ion concentration on the current. Within the cathode region, the effective electrolyte diffusivity and conductivity are reduced from their values when no solid is present. A homogenization approach (the Bruggeman relations) is used to model the transport properties in the porous electrode [23]:

$$D_{eff}=\varepsilon D_2 \tag{7}$$

$$\kappa_{eff}=\varepsilon^{3/2}\kappa_\infty \tag{8}$$

The above model was introduced by Doyle et al. [17]. We have reformulated their model in terms of field and constitutive equations in order to facilitate the numerical treatment of the model. To account for electrochemical–mechanical coupling phenomena, we extended this electrochemical model to include mechanical deformations:

$$\nabla\cdot\boldsymbol{\sigma}+\mathbf{b}=\mathbf{0} \tag{9}$$

assuming the following linear constitutive and kinematic relationships:

$$\boldsymbol{\sigma}=\mathbf{C}:(\mathbf{e}-\mathbf{e}_{ch}),\quad \mathbf{e}=\frac{1}{2}(\nabla\mathbf{u}+\nabla\mathbf{u}^T) \tag{10}$$

where $\boldsymbol{\sigma}$ is the macroscopic stress tensor, $\mathbf{b}$ the vector of body forces, $\mathbf{C}$ the elasticity tensor, $\mathbf{e}^{ch}$ the electrochemical eigenstrain tensor, and $\mathbf{e}$ the total macroscopic strain tensor due to the macroscopic displacements, $\mathbf{u}$.

We model a current-controlled (galvanostatic) discharge process. We assume that there are no resistive loses in the Li foil anode and therefore for every electron that leaves the anode, a Li^+ ion enters the electrolyte. At the anode–separator interface, Γ_{AS}, the anode is modeled through a boundary condition of an influx of Li^+ ions and the requirement that all the current be carried by the electrolyte. This results in Dirichlet boundary conditions on the current carried by the solid and liquid phases and a Neumann boundary condition on the Li^+ ion flux. A Galvanic process is assumed to relate the current discharged to the number of lithium atoms that disassociate at the boundary yielding the Li^+ ion flux. At the cathode–current collector interface, Γ_{CC}, lithium cannot leave the battery, so the Li^+ ion flux is zero, and the solid cathode material carries all the current. We model two mechanical configurations through an elastic model, which is either fixed at both ends or has an external pressure applied at the anode–separator interface, Γ_{AS}. These boundary conditions are summarized in Table 1.

We start our simulations assuming an initially uniform Li^+ concentration. The potential in the electrolyte is zero and the potential in the solid phase is the open circuit potential, U', which depends on the initial Li concentration in the active particles. The battery is initially undeformed. These initial conditions are summarized as follows:

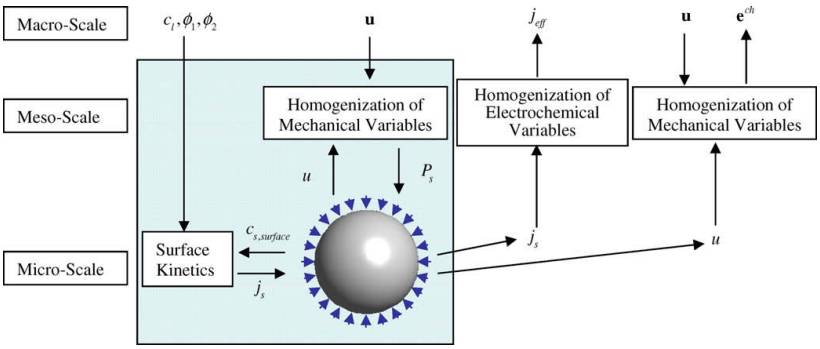

Fig. 2. Interdependency of macro- and micro-scales.

Table 1
Boundary conditions for macro-scale equations.

Boundary condition	Anode–separator interface Γ_{AS}	Cathode–current collector interface Γ_{CC}
Li^+ ion flux	$\mathbf{N} = \frac{I(1-t_+^0)}{F}$	$\nabla c_l = 0$
Current in solid particles	$\mathbf{i}_1 = \mathbf{0}$	$\mathbf{i}_1 = \mathbf{I}$
Current carried by electrolyte	$\mathbf{i}_2 = \mathbf{I}$	$\mathbf{i}_2 = \mathbf{0}$
Mechanical constraints	$\mathbf{u} = 0 / \boldsymbol{\sigma} \cdot \mathbf{n} = \mathbf{p}_{lm}$	$\mathbf{u} = \mathbf{0}$

$$c_l = c_{l,0} \tag{11}$$

$$\phi_2 = 0 \tag{12}$$

$$\phi_1 = U'(c_{s,0}) \tag{13}$$

$$\mathbf{u} = 0 \tag{14}$$

where $c_{l,0}$ and $c_{s,0}$ are initial lithium concentrations in the liquid and solid phases.

2.3. Micro-scale equations

The micro-scale particle model is based on the work of Zhang et al. [12] where diffusion-induced stress in a particle is treated analogously to thermal stress. Zhang et al. solve the equations assuming zero surface traction on the particle and with a constant pore wall flux. In this study we place the particle within the cathode matrix. This requires accounting for particle–matrix and particle–particle interactions, both of which result in surface tractions. While the micro-scale governing equations presented subsequently are the same as in Zhang et al. [12], in our model the boundary conditions change significantly. Also, the pore wall flux into the cathode particles changes at different locations throughout the cathode and is modeled by the Butler–Volmer equation which depends on both micro- and macro-scale variables. The Butler–Volmer equation is widely used in electrochemistry to express the reaction kinetics at the particle surface as the difference between the cathodic and anodic currents [22,24].

The diffusion of Li within the particle is governed by [12]:

$$\frac{\partial c_s}{\partial t} + \nabla \cdot \mathbf{J} = 0 \tag{15}$$

and the static equilibrium for the particle in the absence of body forces is [12]:

$$\sigma_{ij,i} = 0 \tag{16}$$

with the following constitutive and kinematic equations [12,17]:

$$\mathbf{J} = -D_s\left(\nabla c_s - \frac{\Omega c_s}{RT}\nabla \sigma_h\right) \tag{17}$$

$$\sigma_h = (\sigma_{11} + \sigma_{22} + \sigma_{33})/3 \tag{18}$$

$$\sigma_{ij} = \frac{E}{1+v}\varepsilon_{ij} + \left(\frac{Ev}{(1+v)(1-2v)}\varepsilon_{kk} - \frac{E\Omega}{2(1-2v)}c_s\right)\delta_{ij},$$
$$\varepsilon_{ij} = \frac{1}{2}\left(\frac{\partial u_i}{\partial x_j} + \frac{\partial u_j}{\partial x_i}\right) \tag{19}$$

Note that the Li^+ ion flux (17) only depends on the spatial gradient of the hydrostatic stress, $\nabla\sigma_h$, but not on the value of σ_h. The Li^+ ion flux at the particle surface is described by a Butler–Volmer model [17]:

$$BV(c_l, \phi_1, \phi_2, c_{s,surf}) - Fj_s = 0 \tag{20}$$

with

$$BV(c_l, \phi_1, \phi_2, c_s) = i_0\left[c_s \exp\left(\frac{\alpha_A F}{RT}(\eta - U'(c_s))\right) - (c_T - c_s)\exp\left(-\frac{\alpha_C F}{RT}(\eta - U'(c_s))\right)\right],$$
$$i_0 = Fk_2(c_{\max} - c_l)^{\alpha_C}(c_l)^{\alpha_A}, \quad \eta = \phi_1 - \phi_2 \tag{21}$$

The macro-scale response influences the micro-scale model through the boundary conditions at the particle surface. Stresses within the electrode come from two sources: inhomogeneous swelling of the cathode upon intercalation of lithium and from any applied external load. Micro- and macro-scale stresses are related via homogenization of the mechanical response; for this we use the Mori–Tanaka Theory [25] described in Section 2.4. At the macro-scale, the loads are propagated through the battery via Eq. (9). From the meso-scale homogenization procedure, the micro-scale mechanical surface pressure (23) exerted on the particle as a function of macro- and micro-scale displacements is calculated. Macro-scale electrochemical effects are felt by the micro-scale through the Butler–Volmer surface boundary condition (20). As the particle size is sufficiently small such that the macro-scale variables do not vary significantly over the size of a particle, we assume a uniform Li^+ ion flux and pressure at the surface of the particle:

$$\mathbf{J} = j_s \tag{22}$$

$$P_{ni} = \sigma_{ai}\hat{\mathbf{n}} \tag{23}$$

We further assume a uniform initial Li concentration, $c_{s,0}$, in the particle:

$$c_s = c_{s,0} \tag{24}$$

The micro-scale particle-level effects are related to the macro-scale through the homogenization methods described below.

2.4. Meso-scale homogenization methods

The microscopic pore wall flux is related to the macroscopic pore wall flux assuming a uniform flux for all particles in a unit volume of the cathode [23]:

$$j_{eff} = \frac{3(1-\varepsilon)}{R_s} j_s \tag{25}$$

Micro- and macro-scale mechanical properties are related using the Mori–Tanaka (M–T) effective-field theory [25]. This homogenization approach accounts for the interaction of spherical particles (solid phase) within a matrix host (liquid phase). It has been successfully used in a number of multiphysics settings where it has been shown to agree well with experiments for effective elastic properties [26], piezoelectric properties [27], thermal expansion [28], the macroscopic stress–strain curve with a plastically-deforming matrix [29], and estimates of internal stresses in individual particles [30]. Here we use the approach to generate estimates for the effective elastic properties and overall chemical eigenstrains of the aggregate as well as average stresses in the particles due to diffusion and mechanical loads. At the macro-scale, the effective elasticity tensor, $\mathbf{C}_{eff}$, for the cathode is given by [31,32]:

$$\mathbf{C}_{eff} = \mathbf{C}_m + (1-\varepsilon)(\mathbf{C}_s - \mathbf{C}_m)\mathbf{A}_s \tag{26}$$

with

$$\mathbf{A}_s = \mathbf{A}_D[\varepsilon\mathbf{I} + (1-\varepsilon)\mathbf{A}_D]^{-1} \tag{27}$$

$$\mathbf{A}_D = [\mathbf{I} + \mathbf{S}\mathbf{C}_m^{-1}(\mathbf{C}_s - \mathbf{C}_m)]^{-1} \tag{28}$$

where $\mathbf{C}_s$ and $\mathbf{C}_m$ are the stiffness matrices for the solid and liquid (matrix) phases, $\mathbf{I}$ is the identity matrix, and $\mathbf{S}$ is Eshelby's tensor, which is a function of the aspect ratio of the particle and the Poisson's ratio of the matrix phase.

Based on the M–T, model the surface pressure exerted on a spherical particle is a function of the macroscopic total strain, $\mathbf{e}$, and the macroscopic electrochemical eigenstrain, $\mathbf{e}^{ch}$ [31,32]:

$$\mathbf{P}_{ni} = (\mathbf{b}_s + \mathbf{B}_s\mathbf{C}_{eff}(\mathbf{e} - \mathbf{e}^{ch}))\hat{\mathbf{n}} \tag{29}$$

with

$$\mathbf{b}_s = (\mathbf{I} - \mathbf{B}_s)\left(\mathbf{C}_m^{-1} - \mathbf{C}_s^{-1}\right)(\mathbf{e}_s^{ch} - \mathbf{e}_m^{ch}) \tag{30}$$

$$\mathbf{B}_s = \mathbf{B}_D[\varepsilon\mathbf{I} + (1-\varepsilon)\mathbf{B}_D]^{-1} \tag{31}$$

$$\mathbf{B}_D = \mathbf{C}_s\left[\mathbf{I} + \mathbf{S}\mathbf{C}_m^{-1}(\mathbf{C}_s - \mathbf{C}_m)\right]^{-1}\mathbf{C}_m^{-1} \tag{32}$$

The macroscopic eigenstrain $\mathbf{e}^{ch}$ is computed as follows:

$$\mathbf{e}^{ch} = \mathbf{e}_m^{ch} + (1-\varepsilon)(\mathbf{e}_s^{ch} - \mathbf{e}_m^{ch}) + (1-\varepsilon)\left(\mathbf{C}_s^{-1} - \mathbf{C}_m^{-1}\right)\mathbf{b}_s \tag{33}$$

where $\mathbf{e}_m^{ch}$ and $\mathbf{e}_s^{ch}$ are the chemically induced strains in the matrix and solid phases. We calculate $\mathbf{e}_s^{ch}$ from the solution to the micro-scale problem and assume that there is no swelling of the matrix phase of the cathode due to the Li^+ ion concentration, i.e., $\mathbf{e}_m^{ch} = 0$. The macroscopic total strain, $\mathbf{e}$, is a function of the macroscopic displacements (10). Therefore, the stress exerted on the particle surface, P_{ni}, is a function of the total macroscopic strain and the microscopic strain of the particles. This interdependency results in a nonlinear model at the micro-scale with micro-scale boundary conditions on the surface pressure and pore wall flux both of which depend on the macro-scale properties.

3. Numerical implementation

Because the distance across the battery from the anode to the cathodic current collector is significantly smaller than the overall size of a typical battery, we idealize the problem to one-dimension. In our model, $x = 0$ corresponds to the anode–separator interface, Γ_{AS}, $x = \delta_s$ to the separator–cathode interface, Γ_{SC}, and $x = \delta_s + \delta_+$ to the cathode–current collector interface, Γ_{CC}. At the macro-scale, the idealization to one-dimension is straight-forward. At the micro-scale, the three-dimensional problem is idealized to one-dimension by assuming a spherical configuration and that the spatial variation of the macroscopic variables can be neglected locally at the micro-scale. The surface pressure exerted on the particle comes from the meso-scale homogenization, and the surface lithium flux is described by the Butler–Volmer equation.

At the macro-scale, we discretize Eqs. (1), (2), (3), and (9) in time by an implicit Euler backwards scheme and in space by a standard Galerkin finite element approach. The resulting discretized form of the macro-scale field equations is:

$$\begin{aligned}\mathbf{R}_{c_l}: \quad & \frac{1}{\Delta t}\int_\Omega N^T \varepsilon N(\hat{c}_l^{n+1} - \hat{c}_l^n)d\Omega \\ & + \int_\Omega \left(B^T\mathbf{N} + N^T\frac{1}{F}\frac{\partial t_+^0}{\partial c_l^{n+1}}N\hat{\mathbf{i}}_2 B\hat{c}_l^{n+1} - N^T(1-t_+^0)Nj_{eff}\right)d\Omega \\ & + \frac{I(1-t_+^0)}{F}\Big|_{x=0} = \mathbf{0}\end{aligned} \tag{34}$$

$$\mathbf{R}_{i_1}: \quad \int_\Omega (-B^T\mathbf{i}_1^+ N^T F\hat{N}\hat{j}_{eff})d\Omega + \mathbf{I}|_{x=\delta_s+\delta_+} = \mathbf{0} \tag{35}$$

$$\mathbf{R}_{i_2}: \quad \int_\Omega (-B^T\mathbf{i}_2 N^T F\hat{N}\hat{j}_{eff})d\Omega + \mathbf{I}|_{x=0} = \mathbf{0} \tag{36}$$

$$\mathbf{R}_u: \quad \int_\Omega (-B^T\boldsymbol{\sigma} + N^T N\hat{\mathbf{b}})d\Omega + \mathbf{p}_{lm}|_{x=0} = \mathbf{0} \tag{37}$$

with:

$$\mathbf{N} = -D_{eff}B\hat{c}_l^{n+1} \tag{38}$$

$$\mathbf{i}_1 = -\lambda B\hat{\phi}_1^{n+1} \tag{39}$$

$$\mathbf{i}_2 = -\kappa_{eff}\left[B\hat{\phi}_2^{n+1} - \frac{RT}{F}(1-t_+^0)\frac{1}{N\hat{c}_l^{n+1}}B\hat{c}_l^{n+1}\right] \tag{40}$$

$$\boldsymbol{\sigma} = \mathbf{C}_{eff}(\mathbf{e} - \mathbf{e}_{ch}), \quad \mathbf{e} = B\hat{\mathbf{u}}^{n+1} \tag{41}$$

where N is the shape function vector and B is the discretized differential operator. The integrals are evaluated by standard Gauss quadrature. The above equations are combined to yield the following dynamic residual equations:

$$\mathbf{R}_{dyn} = \frac{1}{\Delta t}\mathbf{M}\cdot(\hat{\mathbf{x}}^{n+1} - \hat{\mathbf{x}}^n) + \mathbf{R}(\hat{\mathbf{x}}^{n+1}) = 0 \tag{42}$$

where the vector $\hat{\mathbf{x}}$ collects all macroscopic state variables, $\hat{c}_l,\ \hat{\phi}_1,\ \hat{\phi}_2,\ \hat{\mathbf{u}}$, and the superscript n denotes the time increment. At each time step, Eq. (42) is solved by Newton's method. For the sake of numerical efficiency and robustness, we derive the Jacobian of the residual equations, $\mathbf{J}_{dyn}$, analytically. Because $\mathbf{e}_{ch}$ and j_{eff} depend on $c_l,\ \phi_1,\ \phi_2$, and $\mathbf{u}$, the Jacobian is fully populated and depends on the micro-scale state variables; the evaluation of $\mathbf{J}_{dyn}$ will be outlined later.

In order to compute the effective pore wall flux j_{eff} and the chemical eigenstrains $\mathbf{e}^{ch}$, at every Gauss point we solve a separate micro-scale problem for given values of the macroscopic variables. In this study, Eqs. (15) and (16) are solved assuming a spherical particle geometry. This assumption simplifies the micro-scale calculations to one-dimension. However, our computational framework could be easily augmented to treat particles of any shape. The continuous micro-scale equations for a spherical particle are given in spherical coordinates in Appendix B. Combining an Euler backward scheme and a Galerkin approach to discretize the micro-scale problem in time and space, the discretized governing equations in spherical coordinates are:

$$\begin{aligned}\mathbf{R}_{c_s}: \quad & \frac{1}{\Delta t}\int_r N^T 4\pi(N\hat{r})^2 N(\hat{c}_s^{n+1} - \hat{c}_s^n)dr \\ & + \int_r B^T 4\pi(N\hat{r})^2\mathbf{J}dr - 4\pi R_s^2 j_s|_{r=Rs} = \mathbf{0}\end{aligned} \tag{43}$$

$$\mathbf{R}_u: \quad \int_r (-B^T 4\pi(N\hat{r})^2\sigma_r - N^T 8\pi(N\hat{r})\sigma_t)dr + 4\pi R_s^2 P_s|_{r=R_s} = \mathbf{0} \tag{44}$$

$$\mathbf{R}_{BV}: \quad BV\left(c_l^{n+1}, \phi_1^{n+1}, \phi_2^{n+1}, c_{s,surface}^{n+1}\right) - Fj_s = \mathbf{0} \tag{45}$$

with

$$\mathbf{J} = -D_s\left(B\hat{c}_s^{n+1} - \frac{\Omega}{RT}N\hat{c}_s^{n+1}B\hat{\sigma}_h^{n+1}\right) \tag{46}$$

$$\begin{aligned}\sigma_r &= \frac{E}{(1+\nu)(1-2\nu)}\left((1-\nu)B\hat{u}^{n+1} + 2\nu\frac{N\hat{u}^{n+1}}{N\hat{r}} - \frac{\Omega}{3}N\hat{c}_s^{n+1}(1+\nu)\right) \\ \sigma_t &= \frac{E}{(1+\nu)(1-2\nu)}\left(\nu B\hat{u}^{n+1} + \frac{N\hat{u}^{n+1}}{N\hat{r}} - \frac{\Omega}{3}N\hat{c}_s^{n+1}(1+\nu)\right)\end{aligned} \tag{47}$$

$$\begin{aligned}&BV\left(c_l^{n+1}, \phi_1^{n+1}, \phi_2^{n+1}, c_{s,surface}^{n+1}\right) \\ &\quad = i_0\left[Nc_{s,surface}^{n+1}\exp\left(\frac{\alpha_A F}{RT}\left(\eta - U'\left(N\hat{c}_{s,surface}^{n+1}\right)\right)\right)\right. \\ &\quad\quad \left. -\left(c_T - N\hat{c}_{s,surface}^{n+1}\right)\exp\left(-\frac{\alpha_C F}{RT}\left(\eta - U'\left(N\hat{c}_{s,surface}^{n+1}\right)\right)\right)\right], \\ &\quad i_0 = Fk_2\left(c_{\max} - c_l^{n+1}\right)^{\alpha_C}\left(c_l^{n+1}\right)^{\alpha_A}, \quad \eta = \phi_1^{n+1} - \phi_2^{n+1}\end{aligned} \tag{48}$$

where the radial position $r = 0$ is the center of the particle and $r = R_s$ is the particle surface. The macroscopic variables $c_l,\ \phi_1$, and ϕ_2 defined at a Gauss point of the macro-scale model are

considered constant within the micro-scale model. The micro-scale model is advanced in time synchronously with the macro-scale problem.

To simplify the numerical treatment of the nonlinear flux boundary conditions, we introduce the micro-scale pore wall flux, j_s, as an independent variable and consider the Butler–Volmer equation (45) as part of the governing equations. Furthermore, to limit the order of spatial derivatives in the diffusion equations (43) and (46) to first order, the hydrostatic stress is introduced as an independent field and the hydrostatic stress equation is satisfied in a weak sense:

$$R_{\sigma_h}: \quad \int_r \left(N^T 4\pi (N\hat{r})^2 N\hat{\sigma}_h^{n+1} - N^T 4\pi (N\hat{r})^2 (\sigma_r + 2\sigma_t)/3 \right) dr \tag{49}$$

To consistently approximate displacements and hydrostatic stress and to avoid numerical instabilities, the order of polynomial interpolation for the micro-scale displacements needs to be larger than for the hydrostatic stress. For this study, quadratic elements are used for the displacements and concentrations while linear elements are used for the hydrostatic stress interpolation.

The particle surface pressure depends on the macroscopic total strain and the microscopic volumetric strain through Eqs. (29)–(33). For spherical particles, the microscopic chemically induced eigenstrain of the solid particles, $\mathbf{e}_s^{ch}$, is equal to the volumetric strain of the solid particles, $\mathbf{e}_V$ which depends only on the displacement at the surface of the particle:

$$\mathbf{e}_V = \frac{1}{3}\left(\frac{\left(R_s + u_{surf}^{n+1}\right)^3}{R_s^3} - 1 \right) \tag{50}$$

The homogenized macroscopic electrochemical eigenstrain $\mathbf{e}^{ch}$ is calculated from $\mathbf{e}_V$ using Eq. (33) with $\mathbf{e}_s^{ch} = \mathbf{e}_V$. The conversion from micro-scale pore wall flux j_s to the effective macro-scale flux j_{eff} is given by the homogenization model of Eq. (25).

For solving the nonlinear subproblems at each time step at the macro- and micro-scale, we use analytically derived Jacobians. In order to evaluate the macro-scale Jacobian, $\mathbf{J}_{dyn}$, the derivatives of the micro-scale variables j_s and $\mathbf{e}^{ch}$ with respect to the macro-scale state variables c_l, ϕ_1, ϕ_2, and $\mathbf{u}$ are required. The macroscopic variables c_l, ϕ_1, and ϕ_2, are only present in the micro-scale model through the Butler–Volmer equation (20). The macroscopic displacements, $\mathbf{u}$, are only present in the boundary condition of the elastic residual (16) though the surface pressure. Differentiating the Butler–Volmer equation with respect to c_l, ϕ_1, and ϕ_2 and the elastic residual with respect to $\mathbf{u}$, we can compute the required derivative of j_s with respect to the macroscopic variables. Details of this algorithm are given in Appendix C. The derivatives of electrochemical eigenstrain $\mathbf{e}^{ch}$ with respect to the macro-scale variables are slightly more involved and require the following expansion:

$$\frac{\partial \mathbf{e}_{ch}}{\partial n} = \frac{\partial \mathbf{e}_{ch}}{\partial \mathbf{e}_V}\frac{\partial \mathbf{e}_V}{\partial u_{surf}}\frac{\partial u_{surf}}{\partial n}, \quad \text{for } n = c_s, \phi_1, \phi_2 \tag{51}$$

$$\frac{\partial \mathbf{e}_{ch}}{\partial \mathbf{u}} = \frac{\partial \mathbf{e}_{ch}}{\partial \mathbf{e}_V}\frac{\partial \mathbf{e}_V}{\partial u_{surf}}\frac{\partial u_{surf}}{\partial \mathbf{u}} \tag{52}$$

The derivatives $\partial \mathbf{e}_{ch}/\partial \mathbf{e}_V$ and $\partial \mathbf{e}_V/\partial u_{surf}$ can be found by differentiating Eqs. (33) and (50), respectively. The evaluation of the derivatives of the displacements at the particle surface with respect to the macroscopic variables is given in Appendix C.

4. Verification

We verify our macro- and micro-scale models separately using published data. While our model is not specific for any particular material systems, for verification purposes we model a lithium foil anode, PEO—$LiCF_3SO_3$ electrolyte, and either a TiS_2 or Mn_2O_4 cathode active material. Other materials systems with binary electrolytes can be modeled given their electrochemical and mechanical properties. The material and geometric parameters along with the discretization parameters and convergence criteria used in the following simulations are given in Tables 2 and 3.

We verify our micro-scale problem by comparison with the results of Zhang et al. [12]. We compare our model for a single Mn_2O_4 particle of radius $R_s = 5$ μm with zero surface traction and a constant discharge current of $I = 10$ A/m^2, which corresponds to a surface pore wall flux of $j_s = 10$ A/m^2/F. The particle is discretized by 30 elements. Piecewise quadratic interpolations are used to approximate the lithium concentration and displacements and a piecewise linear interpolation is used for the hydrostatic stress. The evolution of the lithium concentration c_s in the particle is simulated for 1000 s with a time step $\Delta t = 25$ s.

Zhang et al. [12] compare their diffusion–stress coupling model (17) to the classical diffusion equation:

$$\mathbf{J} = -D_s \nabla c_s \tag{53}$$

They find that including the stress effect in Eq. (17) enhances the diffusion through the particle resulting in smaller Li concentration

Table 2
Material parameters.

Symbol	Value	Unit	Reference
PEO—$LiCF_3SO_3$ *electrolyte*			
$c_{l,\max}$	3920	mol/m^3	[17]
$c_{l,0}$	1000	mol/m^3	[17]
D_l	7.5×10^{-13}	m^2/s	[17]
κ_∞	6.5×10^{-3}	S/m	
t_+^0	$0.0107907 + 1.48837 \times 10^{-4}\, c_l$	–	[17]
$\partial t_+^0/\partial c_l$	1.48837×10^{-4}		[17]
TiS_2 *cathode*			
$c_{s,\max}$	29,000	mol/m^3	[17]
$c_{s,0}$	299	mol/m^3	[17]
D_s	5.0×10^{-13}	m^2/s	[17]
σ_s	10^4	S/m	[17]
Mn_2O_4 *cathode*			
$c_{s,\max}$	22,900	mol/m^3	[12]
$c_{s,0}$	4351	mol/m^3	[12]
D_s	7.08×10^{-15}	m^2/s	[12]
σ_s	10^4	S/m	
E	10^9	Pa	[12]
υ	0.3	–	[12]
Ω	3.497×10^{-6}	m^3/mol	[12]

Table 3
Geometric and discretization parameters and convergence criteria.

Symbol	Value	Unit	Reference
Nominal setup for PEO—$LiCF_3SO_3$, TiS_2 *system*			
R_s	5	μm	[17]
ε	0.3	–	[17]
I	12.1	A/m^2	[17]
Mechanical boundary condition	Fixed ends		
Nominal setup for PEO—$LiCF_3SO_3$, Mn_2O_2 *system*			
R_s	5	μm	[12]
ε	0.3	–	
I	12.1	A/m^2	
Mechanical boundary condition	Fixed ends		
Macro-scale problem			
Number of elements for separator			20
Number of elements for cathode			40
Newton convergence tolerance			1e−5
Micro-scale problem			
Number of elements			30
Newton convergence tolerance			1e−5

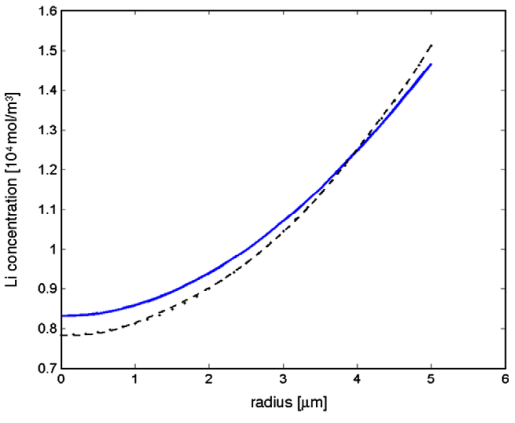

Fig. 3. Li concentration in a single particle at $t = 1000$ s; solid line: the stress-enhanced diffusion model; dashed line: classical diffusion model.

gradients. Our results, shown in Fig. 3, are indistinguishable from those of Zhang et al. [12].

To verify our macro-scale model, we compare our results with those of Doyle et al. [17] for a discharge current-controlled simulation of a one-dimensional battery model. The battery consists of a lithium foil anode, a separator of width $\delta_s = 50$ μm, and a cathode of width $\delta_+ = 100$ μm and volume fraction $\varepsilon = 0.3$. The material system includes a PEO—$LiCF_3SO_3$ electrolyte and TiS_2 cathode particles with $R_s = 1$ μm. The micro-scale diffusion of Li into the cathode particle is modeled by Eq. (53) and solved semi-analytically [17]. The separator is discretized by 20 and the cathode by 40 elements of uniform length. All macro-scale variables c_l, ϕ_1, ϕ_2, and $\mathbf{u}$ are approximated by piecewise linear interpolations. The time step ranges from $\Delta t = 1$ to 10s.

In Fig. 4, we plot the lithium concentration c_l over the normalized distance from the anode, $x/(\delta_s + \delta_+)$, at different instances in time. Overall our simulation results agree well with ones of Doyle et al. [17]. However in the first few seconds, the evolutions of the Li^+ ion concentration differ slightly as shown in Fig. 5. Our model predicts deeper levels of Li^+ ion depletion at the separator–cathode interface, Γ_{SC}. This discrepancy is due to differences in the numerical solution procedure. Doyle et al. [17] use a finite-volume approach and add artificial diffusion via an upwinding scheme to

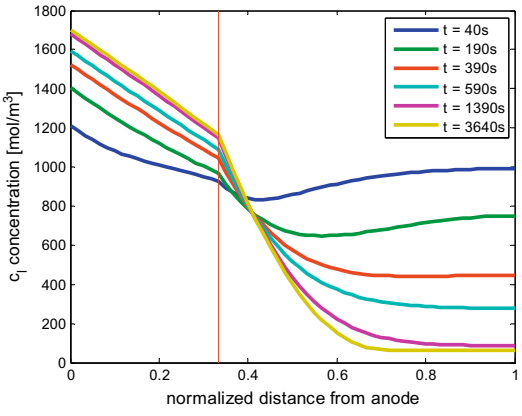

Fig. 4. Evolution of Li^+ concentration in electrolyte over time.

stabilize the results at the separator–cathode interface, Γ_{SC}. We do not observe any instability at this interface in our finite element formulation and therefore do not apply any artificial diffusion.

5. Numerical study of electrochemical–mechanical interaction phenomena

Our computational framework can be readily used to study electrochemical–mechanical interactions within the battery. To illustrate this capability, we revisit the one-dimensional battery model described above and simulate again a single current-controlled discharge process. Here we consider a different material system consisting of PEO—$LiCF_3SO_3$ electrolyte and Mn_2O_4 cathode. This particular material system is chosen due to the availability of material parameters; other systems can be modeled given the material properties. This cathode material system experiences a volume change of up to 6.5% upon lithium insertion [12]. The nominal setup for this system is summarized in Tables 2 and 3.

By varying the electrochemical parameters of the cathode particle radius, the porosity of the cathode, and the discharge current density, we study how the electrochemical properties affect both electrochemical and mechanical performance. Similarly, by changing the mechanical boundary conditions and applying external mechanical loads of different magnitudes, we study the influence of mechanical parameters on the battery performance. We can only partially verify our numerical studies due to a lack of published experimental and numerical studies on the effect of applied pressures on the battery performance.

5.1. Effect of discharge current density

Figs. 6 and 7 show the effects of different discharge current densities on the electrochemical performance of the battery. As expected, a higher current density leads to a lower utilization of the active material and therefore lower capacity. Utilization is the ratio of the actual over the maximum Li concentration that can intercalate into the active cathode material. In Fig. 6 we plot the potential difference between the battery electrodes versus the average utilization of the active cathode material. At higher current densities the voltage drops at lower utilizations, which is agreement with Doyle et al. [17], and results in higher Li concentration gradients in the cathode material, as seen in Fig. 7. At higher discharge rates the active material closest to the separator–cathode interface, Γ_{SC}, saturates with Li faster than the active material farther from the interface. At lower currents, the utilization across the cathode is more even.

Higher Li concentrations result in higher microscopic stresses. At any time step, the maximum radial stress in the spherical particles is always located at the center of the particle. Subsequently, we refer to the radial stress at the particle center as the peak radial stress. In Fig. 8, the maximum of the peak radial stress, which is the maximum over time of the peak radial stress, reached during discharge up to an average utilization of 0.3936 is plotted for different current densities. Larger discharge currents also result in greater maximum macroscopic electrochemical eigenstrains over time as seen in Fig. 9. Note the distributions of the macroscopic electrochemical eigenstrains follow the ones of the averaged Li concentration in the solid particles.

5.2. Effect of particle size

Motivated by increasing capabilities to synthesize engineered cathode materials, we study the effects of the particle size on the electrochemical and mechanical performance. Simulations with particle sizes ranging from 1 to 20 μm were performed. For this

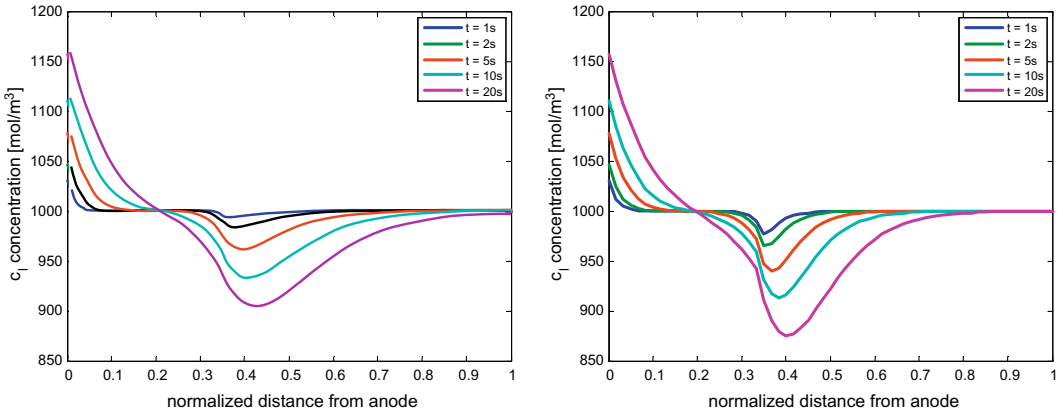

Fig. 5. Evolution of Li^+ concentration in electrolyte for $t \leqslant 20$ s; left: results of Doyle et al. [17]; right: results predicted by numerical framework presented in this paper.

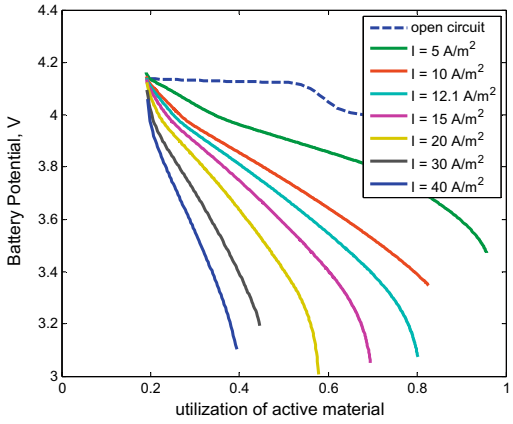

Fig. 6. Discharge characteristics for different discharge current densities.

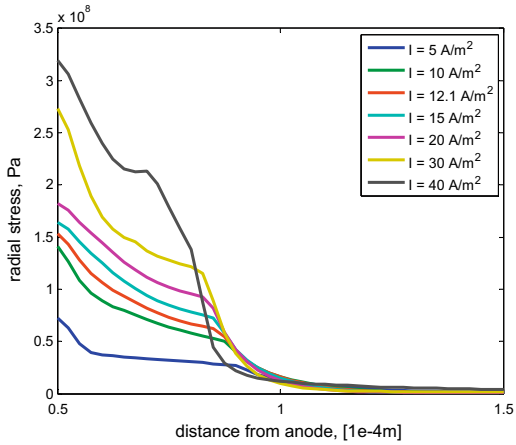

Fig. 8. Maximum peak radial stress in the particles over time when discharged from 0.19 to 0.3936 average utilization.

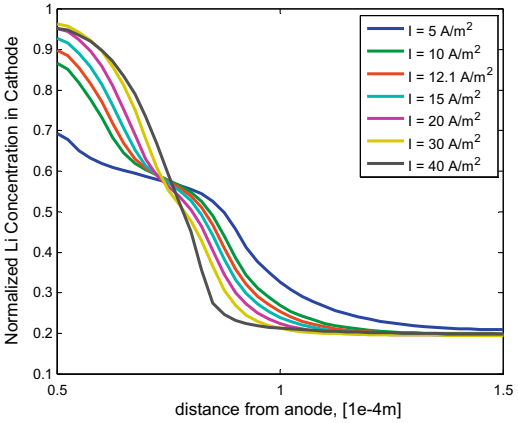

Fig. 7. Normalized lithium concentration profiles at average utilization of 0.3936.

portion of the study, the volume fraction, ε, is kept constant at 0.3 and the particle size is varied, therefore the overall electrochemical capacity of the battery is unchanged. Our results show that smaller particle sizes give better electrochemical performance, characterized by the dependency of the battery voltage on the utilization of the solid cathode material, as shown in Fig. 10. Smaller particles also experience lower peak radial stresses over time, as shown in Fig. 11. This is in qualitative agreement with Wang and Sastry's simulations [18] which show a decrease in performance with larger particle sizes, and with Aifantis, Hackney, and Dempsey's work [11] which predicts that smaller particle sizes will be less susceptible to failure due to cracking.

5.3. Effect of porosity of the cathode

The porosity, ε, the liquid volume fraction in the cathode, affects the battery in terms of overall capacity and utilization of the active material. If the porosity is high, the energy capacity of the battery is lower because there is less active material into which Li can intercalate. In this case the active cathode material particles uptake

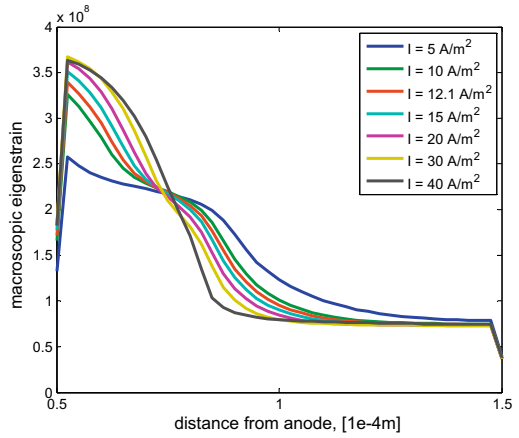

Fig. 9. Maximum macroscopic electrochemical eigenstrain over time in the cathode during discharge from 0.19 to 0.3936 average utilization.

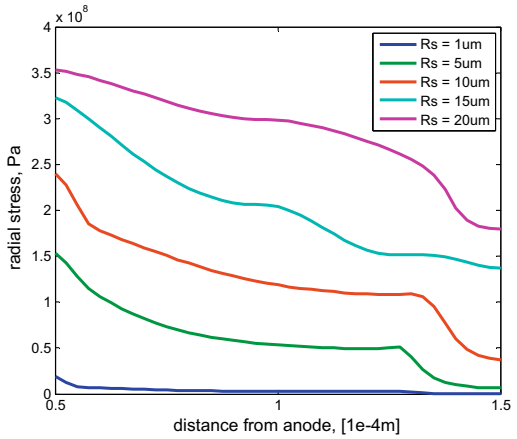

Fig. 11. Maximum peak radial stress in the cathode particles over time during discharge from 0.19 to 0.7 average utilization.

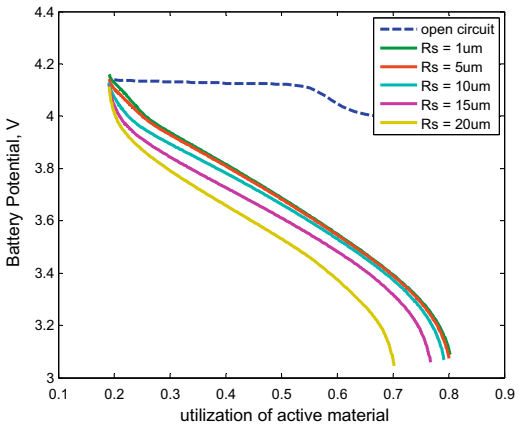

Fig. 10. Battery potential over utilization of cathode material for different particle sizes.

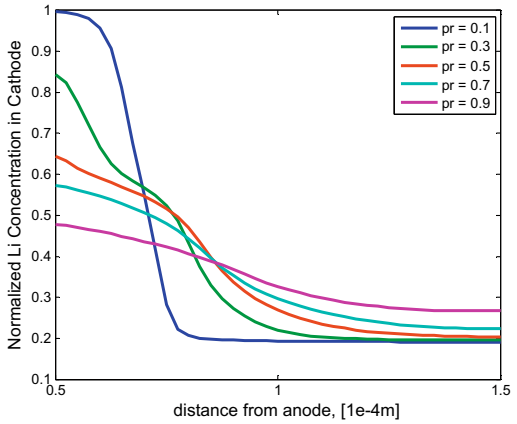

Fig. 12. Normalized Li concentration in cathode for different porosities at average utilization of the cathode material of 0.35.

Li^+ ions fairly evenly as seen in Fig. 12. However, if the porosity of the battery is too low, Li^+ ions do not effectively move through the liquid phase to the deeper regions of the cathode and higher gradients in Li concentration will be found across the cathode. In this case, the higher gradients prohibit full utilization of the cathode, so the increased theoretical capacity of the battery is not reached. The lower porosity also leads to higher macroscopic eigenstrains across the battery cathode as seen in Fig. 13.

5.4. Effect of mechanical boundary conditions

We compute the macro- and micro-scale response of our battery model for varying mechanical boundary conditions. We study two cases: (a) the battery is clamped at both ends, and (b) an external pressure is applied at the anode–separator interface, Γ_{AS}, and the cathode–current collector interface, Γ_{CC}, is clamped. Pressure values of ±10 MPa and ±100 MPa are considered.

In the case of spherical particles, our model predicts that there is no influence of the interlaminate stress on the electrochemical performance of the battery. As pointed out earlier, the micro-scale diffusion equation (17) depends only on the gradient of the hydrostatic stress. The predicted insensitivity of the electrochemical performance with respect to external mechanical loading conditions is in qualitative agreement with the experimental work of Periea et al. [15].

However, the dependency of macro- and micro-scale stresses across the battery on the mechanical boundary conditions cannot be ignored, as they will contribute to failure mechanisms in the battery. As is expected, greater interlaminate stress correlates to higher strains and stresses across the battery as seen in Figs. 14 and 15.

6. Conclusions

We have developed a multi-scale finite element model of the electrochemical and mechanical interactions in lithium batteries subject to external mechanical loads. At the macro-scale, we have extended Doyle and Newman's electrochemical porous electrode model to account for elastic deformations. At the micro-scale we have accounted for differences in Li^+ ion flux into the particles due to interfacial surface conditions using the Butler–Volmer

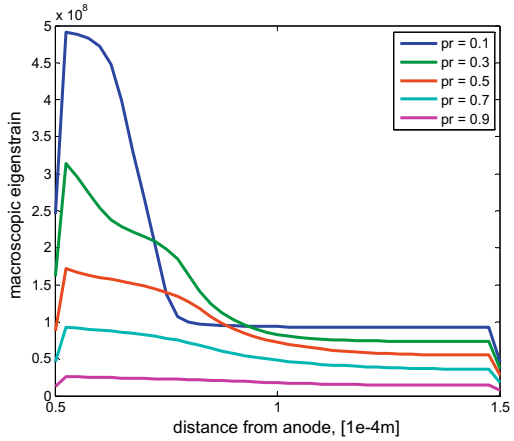

Fig. 13. Maximum macroscopic eigenstrain in the cathode over time when discharged from 0.19 to 0.35 average utilization.

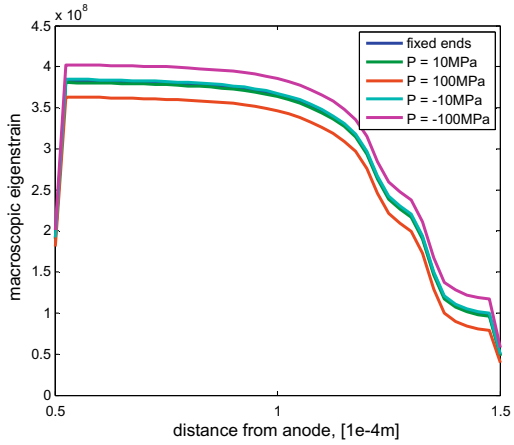

Fig. 14. Maximum macroscopic eigenstrain in cathode over time for different mechanical boundary conditions when discharged from 0.19 to 0.7 average utilization.

equation and for surface pressures exerted on the particles by the composite cathode matrix. We have introduced a meso-scale aggregate model to relate micro- and macro-scale mechanical effects. The macro- and micro-scale models are discretized in time by an implicit Euler backward scheme and in space by a Galerkin finite element method. The nonlinear macro- and micro-scale subproblems are solved by Newton's method using analytically derived Jacobians.

We have verified our macro- and micro-scale models separately through comparison with previously published simulation results. The potential of our multi-scale model was demonstrated by numerical studies on the influence of electrochemical and mechanical parameters on the battery performance. Our simulation results are in agreement with related simulation results and experimental studies, which predict better electrochemical performance and lower particle-level stresses for smaller cathode particle sizes

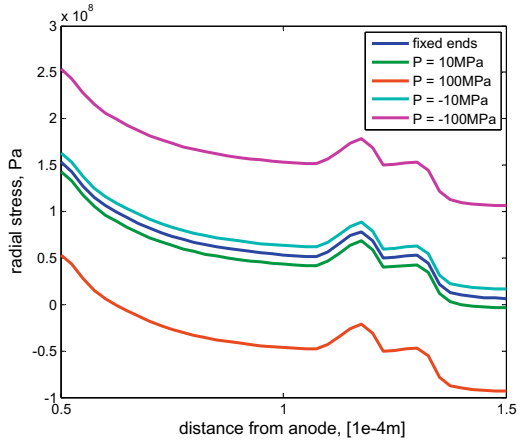

Fig. 15. Maximum peak radial stress in cathode particles over time, plotted over the cathode, when battery is discharged from 0.19 to 0.7 average utilization.

[11,12], and no influence of mechanical boundary conditions on electrochemical performance [15].

The numerical implementation and studies presented in this paper were limited to spherical cathode particles and single current-controlled discharge processes, neglecting accumulated stresses due to cycling of the battery. However, our numerical framework already allows the simulation of discharge–charge cycles and can be easily augmented to include more complex particle geometries. Currently, we are extending this framework to account for thermal effects at both macro- and micro-scale.

Acknowledgements

The authors gratefully acknowledge the support of the Air Force Office of Scientific Research MURI (grant F9550-06-1-0326) "Energy Harvesting and Storage Systems for Future Aerovehicles", monitored by Dr. B.L. Lee, and the support of the National Science Foundation under Grant CMMI 0729520. The first author acknowledges the support of the National Science foundation under the Graduate Research Fellowship Program. Any opinions, findings, and conclusions or recommendations expressed in this material are those of the authors and do not necessarily reflect the views of the Air Force Office of Scientific Research or the National Science Foundation.

Appendix A. List of symbols

Symbol	Units	Description
A_s, B_s, b_s		Concentration factors (Mori–Tanaka theory)
B	–	Derivatives of the shape function vector
$\mathbf{b}$	Pa	Body force
$\mathbf{C}$	Pa	Homogenized elasticity tensor
$\mathbf{C}_s$, $\mathbf{C}_m$	Pa	Isotropic elastic stiffness matrix for solid and liquid phases
c_l	mol/m^3	Concentration of lithium in electrolyte
$c_{\max}$	mol/m^3	Max concentration in polymer
c_s	mol/m^3	Concentration of lithium in solid particles

(*continued on next page*)

Appendix A. (*continued*)

Symbol	Units	Description
c_T	mol/m^3	Max concentration in solid
D_l	m^2/s	Diffusion coefficient of electrolyte
D_s	m^2/s	Diffusion coefficient of lithium in the solid
E	Pa	Young's modulus of solid particles
$\mathbf{e}$	–	Macroscopic strains due to macroscopic displacements
$\mathbf{e}^{ch}$	–	Chemically induced eigenstrain
$\mathbf{e}_V$	–	Volumetric strain of a particle
F	C/mol	Faraday's constant
I	A/m^2	Superficial current density
$\mathbf{i}_1$	A/m^2	Current density in solid phase
$\mathbf{i}_2$	A/m^2	Current density in liquid phase
j_{eff}	mol/m^2 s	Macro-scale effective pore wall flux
j_s	mol/m^2 s	Micro-scale pore wall flux
k_2	m^4/mol s	Reaction rate constant at cathode/polymer interface
$\mathbf{N}$	mol/m^2/s	Lithium ion flux in the electrolyte
N	–	Shape Function vector
P_s	Pa	Surface pressure exerted on a particle
$\mathbf{p}_{lm}$	Pa	Surface pressure
R	J/mol/K	Universal gas constant
R_s	m	Radius of cathode particles
r	m	Micro-scale distance from center of cathode particle
$\mathbf{S}$		Eshelby's tensor
T	K	Temperature
t	s	Time
t_+^0	–	Lithium ion transference number
U'	V	Open circuit potential
$\mathbf{u}$	m	Macroscopic displacements
u	m	Microscopic displacements within a particle
V	m^3	Total volume
V_l	m^3	Volume of liquid phase
x	m	Distance from anode
$\alpha_A,\ \alpha_C$	–	Anodic and cathodic transfer coefficients
δ_s	m	Thickness of separator
δ_+	m	Thickness of composite cathode
ε	–	Porosity, liquid volume fraction
ε_{ij}	–	Microscopic strain
ϕ_1	V	Potential in solid phase
ϕ_2	V	Potential in liquid phase
η	V	Surface overpotential
κ_{eff}	S/m	Effective conductivity of electrolyte
κ_∞	S/m	Conductivity of electrolyte, nothing else present
λ	S/m	Conductivity of solid matrix
ν	–	Poisson's ratio for solid particles
Ω	m^3/mol	Partial molar volume
Γ_{CA}		Current collector–anode interface
Γ_{AS}		Anode–separator interface
Γ_{SC}		Separator–cathode interface
Γ_{SC}		Cathode–current collector interface
$\boldsymbol{\sigma}$	Pa	Macroscopic stress
σ	Pa	Microscopic stress
σ_h	Pa	Hydrostatic stress

Appendix B. Micro-scale equations in spherical coordinates

We summarize the micro-scale equations in spherical coordinates which are used in our numerical implementation. The micro-scale governing equations are:

$$\frac{\partial c_s}{\partial t}+\left(\nabla_r+\frac{2}{r}\right)\mathbf{J}=0 \tag{54}$$

$$\frac{d\sigma_r}{dr}+\frac{2}{r}(\sigma_r-\sigma_t)=0 \tag{55}$$

$$\sigma_h-(\sigma_r+2\sigma_t)/3=0 \tag{56}$$

with the corresponding constitutive equations:

$$\mathbf{J}=-D_s\left(\nabla_r c_s-\frac{\Omega c_s}{RT}\nabla_r\sigma_h\right) \tag{57}$$

$$\sigma_r=\frac{E}{(1+\nu)(1-2\nu)}\left((1-\nu)\nabla u+2\nu\frac{u}{r}-\frac{\Omega}{3}\tilde{c}_s(1+\nu)\right) \tag{58}$$

$$\sigma_t=\frac{E}{(1+\nu)(1-2\nu)}\left(\frac{u}{r}+\nu\nabla u-\frac{\Omega}{3}\tilde{c}_s(1+\nu)\right) \tag{59}$$

The boundary conditions at the particle surface, $r=R_s$, are:

$$\mathbf{J}=j_s \tag{60}$$

$$\sigma_r=P_s \tag{61}$$

$$BV(c_l,\phi_1,\phi_2,c_{s,surf})-Fj_s=0 \tag{62}$$

where $BV(c_l,\phi_1,\phi_2,c_{s,surf})$ is defined as in Eq. (21). The boundary conditions at the particle center, $r=0$, are:

$$\nabla_r c_s=0 \tag{63}$$

$$u=0 \tag{64}$$

Appendix C. Jacobian of micro-scale problem and derivatives of micro-scale variable with respect to macro-scale variables

The Jacobian of the micro-scale problem is simplified to show only variables describing surface phenomena and includes the following terms:

$$\mathbf{J}=\begin{bmatrix}\frac{\partial R_{c_s}}{\partial c_s} & 0 & \frac{\partial R_{c_s}}{\partial \sigma_h} & \frac{\partial R_{c_s}}{\partial j_s}\\ \frac{\partial R_u}{\partial c_s} & \frac{\partial R_u}{\partial u} & 0 & \frac{\partial R_u}{\partial j_s}\\ \frac{\partial R_{\sigma_h}}{\partial c_s} & \frac{\partial R_{\sigma_h}}{\partial u} & \frac{\partial R_{\sigma_h}}{\partial \sigma_h} & \frac{\partial R_{\sigma_h}}{\partial j_s}\\ \frac{\partial R_{BV}}{\partial c_s} & \frac{\partial R_{BV}}{\partial u} & \frac{\partial R_{BV}}{\partial \sigma_h} & \frac{\partial R_{BV}}{\partial j_s}\end{bmatrix} \tag{65}$$

In order to find values for the derivatives of the micro-scale variables with respect to macro-scale variables, $n=c_l,\ \phi_1,\ \phi_2$ and $\mathbf{u}$, the following systems of linear equations are solved:

$$\mathbf{J}\begin{bmatrix}\frac{\partial c_s}{\partial n}\\ \frac{\partial u_{surf}}{\partial n}\\ \frac{\partial \sigma_h}{\partial n}\\ \frac{\partial j_s}{\partial n}\end{bmatrix}=-\begin{bmatrix}0\\0\\0\\ \frac{\partial R_{BV}}{\partial n}\end{bmatrix} \tag{66}$$

$$\mathbf{J}\begin{bmatrix}\frac{\partial c_s}{\partial \mathbf{u}}\\ \frac{\partial u_{surf}}{\partial \mathbf{u}}\\ \frac{\partial \sigma_h}{\partial \mathbf{u}}\\ \frac{\partial j_s}{\partial \mathbf{u}}\end{bmatrix}=-\begin{bmatrix}0\\ \frac{\partial R_u}{\partial \mathbf{u}}\\0\\0\end{bmatrix} \tag{67}$$

where the derivatives $\partial R_{BV}/\partial n$ with $n = c_l,\ \phi_1,\ \phi_2$ and $\partial R_u/\partial \mathbf{u}$ are found analytically.

References

[1] Winter M, Brodd RJ. What are batteries, fuel cells, and supercapacitors? Chem Rev 2004;104(10):4245–69.
[2] Wang D et al. Cracking causing cyclic instability of $LiFePO_4$ cathode material. J Power Sources 2005;140(1):125–8.
[3] Thomas JP, Qidwai MA. The design and application of multifunctional structure-battery materials systems. JOM 2005;57(3):18–24.
[4] Wang H et al. TEM study of electrochemical cycling-induced damage and disorder in $LiCoO_2$ cathodes for rechargeable lithium batteries. J Electrochem Soc 1999;146(2):473–80.
[5] Thackeray MM et al. Advances in manganese-oxide composite electrodes for lithium-ion batteries. J Mater Chem 2005;15:2257–67.
[6] Aifantis KE, Hackney SA. An ideal elasticity problem for Li-batteries. J Mech Behav Mater 2003;14:413–27.
[7] Huggins RA, Nix WD. Decrepitation model for capacity loss during cycling of alloys in rechargeable electrochemical systems. Solid State Ionics 2000;6:57–63.
[8] Aifantis KE, Dempsey JP. Stable crack growth in nanostructured Li-batteries. J Power Sources 2005;143(1):203–11.
[9] Christensen J, Newman J. Stress generation and fracture in lithium insertion materials. J Solid State Electrochem 2006;10(5):293–319.
[10] Christensen J, Newman J. A mathematical model of stress generation and fracture in lithium manganese oxide. J Electrochem Soc 2006;153(6):1019–30.
[11] Aifantis KE, Hackney SA, Dempsey JP. Design criteria for nanostructured Li-ion batteries. J Power Sources 2007;165:874–9.
[12] Zhang X, Shyy W, Sastry AM. Numerical simulation of intercalation-induced stress in Li-ion battery electrode particles. J Electrochem Soc 2007;154(10):910–6.
[13] Pereira T et al. The performance of thin-film Li-ion batteries under flexural deflection. J Micromech Microeng 2006;16(12):2714–21.
[14] Pereira T et al. Performance of thin-film lithium energy cells under uniaxial pressure. Adv Eng Mater 2008;10(4):393–9.
[15] Pereira T et al. Embedding thin-film lithium energy cells in structural composites. Compos Sci Technol 2008;68(7–8):1935–41.
[16] West K, Jacobsen T, Atlung S. Modeling of porous insertion electrodes with liquid electrolyte. J Electrochem Soc 1982;129(7):1480–5.
[17] Doyle M, Fuller TF, Newman J. Modeling of galvanostatic charge and discharge of the lithium/polymer/insertion cell. J Electrochem Soc 1993;140(6):1526–33.
[18] Wang C, Sastry AM. Mesoscale modeling of a Li-ion polymer cell. J Electrochem Soc 2007;154(11):1035–47.
[19] Garcia RE et al. Microstructural modeling and design of rechargeable lithium-ion batteries. J Electrochem Soc 2005;152:255–63.
[20] Garcia RE, Chiang Y. Spatially resolved modeling of microstructurally complex battery architectures. J Electrochem Soc 2007;154(9):856–64.
[21] Zhang X, Sastry AM, Shyy W. Intercalation-induced stress and heat generation within single lithium-ion battery cathode particles. J Electrochem Soc 2008;155(7):542–52.
[22] Newman J, Thomas-Alyea KE. Electrochemical systems. Hoboken: Wiley; 2004.
[23] Doyle M. Design and simulation of lithium rechargeable batteries. PhD thesis, Department of Chemical Engineering, University of California, Berkeley; 1995.
[24] Bard AJ, Faulkner LR. Electrochemical methods. Hoboken: John Wiley and Sons; 2001.
[25] Mori T, Tanaka K. Average stress in matrix and average elastic energy of materials with misfitting inclusions. Acta Metall 1973;21:571–4.
[26] Dunn ML, Ledbetter H. Thermal expansion of textured polycrystalline aggregates. J Appl Phys 1995;78:1583–8.
[27] Dunn ML, Taya M. Micromechanics predictions of the effective electroelastic moduli of piezoelectric composites. Int J Solid Struct 1993;30:161–75.
[28] Dunn ML et al. Elastic constants of textured short fiber composites. J Mech Phys Solid 1996;44:1509–41.
[29] Dunn ML, Ledbetter H. Elastic–plastic behavior of textured short fiber composites. Acta Mater 1997;45:3327–40.
[30] Gall K et al. Internal stress storage in shape memory polymer nanocomposites. Appl Phys Lett 2004;85:290–2.
[31] Benveniste Y. A new approach to the application of Mori–Tanaka's theory in composite materials. Mech Mater 1987;6:147–57.
[32] Benveniste Y, Dvorak GJ. On a correspondence between mechanical and thermal effects in two-phase composites. Micromechancis and inhomogeneity. New York: Springer; 1990.

Appendix B

Publication: Stress generation in silicon particle during lithium insertion

APPLIED PHYSICS LETTERS **97**, 033111 (2010)

Stress generation in silicon particles during lithium insertion

Stephanie Golmon,[1,a)] Kurt Maute,[1,b)] Se-Hee Lee,[2] and Martin L. Dunn[2]
[1]*Department of Aerospace Engineering Sciences, University of Colorado, CB 429, Boulder, CO 80301–0429, USA*
[2]*Department of Mechanical Engineering, University of Colorado at Boulder, USA*

(Received 28 April 2010; accepted 8 June 2010; published online 21 July 2010)

Using a fully-coupled diffusion-elasticity model with Butler–Volmer surface kinetics, we simulate the insertion of lithium into spherical silicon particles. Simulations predict the evolution of concentration, displacements, and stresses in the particles during the first insertion of Li. The particle response depends strongly on the reaction kinetics and the resulting stresses can be above the tensile failure stress of silicon depending on the particle size and discharge rate. © *2010 American Institute of Physics*. [doi:10.1063/1.3458707]

Rechargeable lithium ion batteries are particularly attractive due to their high gravimetric and volumetric energy density, high operating voltage, low self-discharge rate, and the lack of memory effects. Traditional lithium ion batteries employ carbonaceous anodes with a capacity of 372 mA hg^{-1}. The most attractive candidate to replace carbonaceous anodes is silicon which has the highest known capacity, in excess of 4000 mA hg^{-1}.[1,2] A drawback with silicon is that a volume expansion on the order of 300% (Ref. 3) to 400% (Ref. 4) occurs upon Li insertion due to the formation of LiSi alloys, a process thought to culminate in $Li_{22}Si_5$ where each Si atom accommodates 4.4 Li atoms.[5] Stresses associated with these large volume changes have been cited as the cause of cracking and pulverization of Si electrodes that leads to loss of electrical contact and capacity fade during cycling.[2] Mechanistic details regarding the cyclic degradation that leads to capacity fade, are not well developed, and many papers simply state that it is related to the large volume change that results upon Li insertion.

A number of observations exist that suggest silicon anodes with morphology of nanometer scale dimensions are more robust than anodes with larger-dimension morphology with regard to cyclic degradation. For example, Li *et al.*[6] showed that composite anodes with Si particles in the 50–100 nm range have better cycling performance than those in the micrometer range. Another line of inquiry has shown that arrays of Si nanowires exhibit cycling performance with no degradation.[7] A third example showed that nanoporous Si architectures result in capacity retention that exceeds that of nanoscale particles and nanowires.[8] Presumably the improvement that results from nanoscale architectures is related to the stresses developed during cycling. In this paper we take a step toward developing an understanding of the interaction between Si morphology size and stress generation during Li cycling.

Christensen and Newman studied diffusion induced stresses under constant current and Butler–Volmer current conditions[9] as well as stress and fracture in $Li_yMn_2O_4$.[10] Zhang *et al.*[11,12] studied Li insertion in Mn_2O_4 with a fully-coupled electrochemical and mechanical model with lithium influx governed by a constant current and through Butler–Volmer surface kinetics. Cheng and Verbrugge[13,14] developed analytical models for diffusion-induced stresses for both galvanostatic and potentiostatic operation of cells, however this model does not capture the influence of surface reactions, or account for the influence of stress on diffusion.

Here we simulate the development of stresses in a spherical Si particle using a continuum model that describes the fully-coupled mechanics and diffusion during Li insertion. The influx of Li is modeled by a Butler–Volmer model that describes the electrochemical reaction kinetics at the Si particle/electrode interface. These results are used to form a parameter map of the maximum tensile stress as a function of discharge rate and particle size, in order to provide guidelines for the design of cracking-resistant electrodes. We focus on the first insertion of lithium into silicon in order to quantify the initial development of the stresses. We do not consider the impact of degradation mechanisms that occur upon Li cycling; these stresses are beyond the scope of our present study.

We idealize the electrode particles as spherically symmetric particles embedded in a host electrolyte. The effects of the host electrolyte enter the model through the particle surface kinetics. We take the Si particles to be isotropic, deform in a linearly elastic manner, and we neglect surface stress effects;[15–17] all of these assumptions can be removed with a more sophisticated analysis. Reaction kinetics at the particle/electrolyte surface are described by a Butler–Volmer model.[18,19] This describes the influx of Li as a function of time and overpotential. The subsequent transport of Li through the spherical particle is modeled as a diffusion process. As Li ions diffuse through the Si lattice the particle is strained. In spherical coordinates the coupled diffusion and displacements are described by:[11]

$$\frac{\partial c}{\partial t} + \left(\nabla_r + \frac{2}{r}\right)\mathbf{J} = 0, \tag{1}$$

$$\frac{d\sigma_r}{dr} + \frac{2}{r}(\sigma_r - \sigma_t) = 0, \tag{2}$$

$$\sigma_h - (\sigma_r + 2\sigma_t)/3 = 0. \tag{3}$$

Equation (1) describes the diffusion process where c is the concentration of Li ions and $\mathbf{J}$ is the Li ion flux. Equation (2) describes the elastic deformation where σ_r, σ_t, and σ_h are the

[a)]Electronic mail: stephanie.golmon@colorado.edu.
[b)]Electronic mail: kurt.maute@colorado.edu.

radial, tangential, and hydrostatic stresses that occur during the spherically-symmetric deformation. We take the elasticity to be quasistatic because the time scale for elastic deformation is far shorter than that for diffusion. The full coupling between diffusion and elasticity is reflected in the constitutive equations:

$$\mathbf{J} = -D\left(\nabla_r c - \frac{\Omega c}{R_g T}\nabla_r \sigma_h\right), \tag{4}$$

$$\sigma_r = \frac{E\left[(1-\nu)\nabla u + 2\nu\frac{u}{r} - \frac{\Omega}{3}c(1+\nu)\right]}{(1+\nu)(1-2\nu)}, \tag{5}$$

$$\sigma_t = \frac{E\left[\frac{u}{r} + \nu\nabla u - \frac{\Omega}{3}c(1+\nu)\right]}{(1+\nu)(1-2\nu)}. \tag{6}$$

Here D is the diffusion coefficient of Li in Si, E and ν are Young's modulus and Poisson's ratio of Si, respectively. The material parameters are taken to be constant and independent of concentration, although this restriction could be removed in a straightforward manner. In Eq. (4) R_g is the gas constant, T is the absolute temperature which is assumed to be constant, and Ω is the Li ion partial molar volume.

At the center of the particle, $u=0$ and $\mathbf{J}=0$; the surface of the particle is taken to be traction free. The ion flux at the particle surface is dictated by the kinetics of the electrochemical reaction and described by a Butler–Volmer equation:[20]

$$\mathbf{J} = \frac{i_0}{F}\left[\exp\left\{\frac{\alpha_A F}{R_g T}[\eta - U(c/c_{\max})]\right\} - \exp\left\{\frac{\alpha_C F}{R_g T}[\eta - U(c/c_{\max})]\right\}\right], \tag{7}$$

$$i_0 = Fk(c_l)^{\alpha_A}(c_{\max} - c)^{\alpha_A}(c)^{\alpha_C}. \tag{8}$$

In Eqs. (7) and (8), F is the Faraday constant, c_l is the concentration of lithium in the surrounding electrolyte, k is the interfacial charge transfer reaction constant, η is the electric potential difference between the silicon and matrix, and $U(c/c_{\max})$ is the open circuit electric potential of lithium in silicon as a function of normalized concentration. We take c_l, k, and T to be constant in our simulations. The diffusion-elasticity model is discretized by a finite element approach and an Euler backward time marching scheme.[21] Mesh and time-step refinement studies to ensure convergence were performed.

Simulations reported in this paper are for the first insertion of Li into Si and are driven by a linearly-varying electric potential η. A range of particle radii and potential sweep rates are investigated and the development of stresses is monitored. The electric potential is controlled by a potential sweep rate, v; i.e., $\eta=\eta_0-vt$ for $vt<\eta_0$ and $\eta=0$ for $vt>\eta_0$. The difference between the applied potential and equilibrium open circuit potential drives the electrochemical reaction at the particle surface to generate a current flux at the particle surface. Parameters used in our simulations are given in Table I. For the first insertion of lithium into silicon, the open circuit potential is interpolated from experimental results of Baggetto *et al.*[3] The value for k in the Butler–Volmer equation was found by fitting simulations of cyclic voltammagrams for planar films to experimental results[3] with the goal of matching the location and slope of the initial increase in current influx during Li insertion. Consistent with Baggetto *et al.*,[3] here we take $c_{\max}$ to occur at $Li_{15}Si_4$ with a 300% volume expansion upon full insertion of Li. The model is initialized with a uniform concentration of $c_0=0.01c_{\max}$, corresponding uniform swelling, and potential of $\eta_0=U(c_0)$. All calculations are performed in reference to the undeformed body. Simulations are carried out until the particle reaches 96% utilization (the average concentration of Li in Si normalized by $c_{\max}$).

TABLE I. Parameters for silicon and Butler–Volmer model.

Symbol	Value	Units	References
D	10^{-16}	m^2/s	22
E	112.4	GPa	23
ν	0.28	⋯	23
ρ	2.33	g/cm^3	5
$c_{\max}$	311 053	mol/m^3	Calculated[a]
Ω	4.265×10^{-6}	m^3/mol	Calculated[b]
c_l	1000	mol/m^3	
k	1×10^{-13} [c]	$m^{5/2}\ s^{-1}\ mol^{-1/2}$	
T	300	K	
α_A, α_C	0.5	⋯	
F	96 487	C/mol	
R_g	8.3143	J/mol/K	

[a]Calculated using the density and atomic weight of Si, and assuming 3.75 Li/Si.
[b]Calculated from $\Omega=3\varepsilon/c_{\max}$ where ε is the predicted strain from a 300% volume expansion of 0.442.
[c]Found by fitting cyclic voltammagrams to experimental results.[3]

Figure 1 explores the spatial and temporal variation in the concentration and stress fields during lithium insertion. The applied overpotential decreases linearly, until it reaches zero, and then is maintained at zero [Fig. 1(a)]. The resulting current influx into the particle [Fig. 1(b)] varies with time

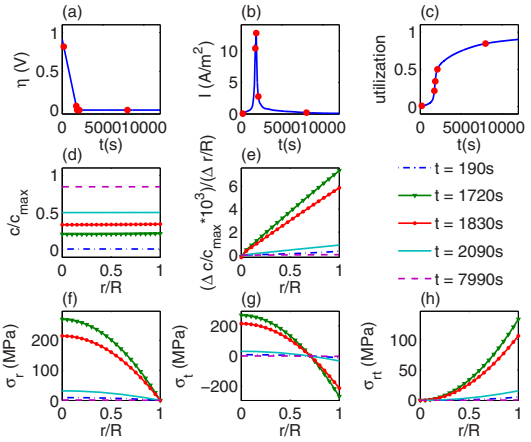

FIG. 1. (Color online) (a) Applied overpotential, η, (b) current, I, and (c) particle utilization, as a function of time. (d) $c/c_{\max}$, (e) $(\Delta c/c_{\max})/(\Delta r/R)$, (f) radial stress, σ_r, (g) tangential stress, σ_t, and (h) shear stress, σ_{rt}, profiles across the radius of a $R=1$ μm particle at different times for a potential sweep rate of $v=-0.5$ mV/s. The time instances shown in plots (d)–(h) correspond to the times marked with dots in plots (a)–(c).

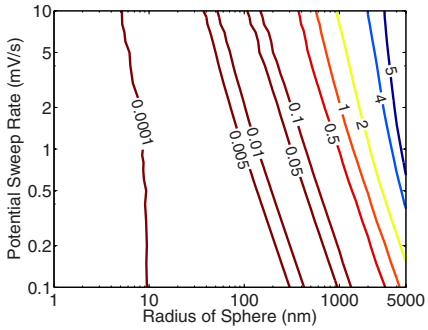

FIG. 2. (Color online) Maximum magnitude of tensile stress (over time) as a function of potential sweep rate and particle radius.

and drives the overall utilization of the particle [Fig. 1(c)]. The timescales of Li insertion into and subsequent diffusion within the sphere are such that the spatial distribution of lithium in the sphere remains nearly constant at all times [Fig. 1(d)], however there is a gradient in the concentration, with higher concentrations at the particle surface than at the center [Fig. 1(e)]. The insertion of lithium gives rise to stresses that vary with position and time [Figs. 1(f)–1(h)].

During Li insertion, the radial stress in the Si particle is always tensile, maximum at the center of the particle, and decreases monotonically to zero at the particle surface. The tangential stress on the other hand is compressive at the surface and tensile in the interior of the particle; it is equal to the radial stress at the center where the particle is in a state of hydrostatic tension and the magnitude is a maximum at the surface. The shear stress vanishes at the center of the particle and increases as the surface is approached. All three stresses peak at the same time, shortly before the maximum current is reached, and then decrease with continued Li insertion. As the concentration increases in the material near the surface, it swells with respect to the material near the center of the particle, i.e., there is a mismatch in strain. Material just inside the surface that has yet to swell constrains material at the surface from swelling freely, which results in tensile stress near the center of the particle. When the rate of Li insertion rises [Fig. 1(b)], lithium enters the particle at the surface significantly faster than it can diffuse through the particle, i.e., the process is reaction dominated. This causes the local concentration gradient and thus the mismatch in strain to increase. As the concentration becomes more uniform, the strain mismatch within the particle decreases and so do the stresses.

Figure 2 shows the influence of the particle size and potential sweep rate on the maximum (over time) tensile stress at the particle center. A contour line of 1 GPa (the tensile failure stress of silicon is in the range of 1–4 GPa (Refs. 24–26) is seen at the right of the plot and can be considered to separate two regions of a failure map. Points above and to the right of this line describe configurations that would be expected to fail, while those below and to the left of the line would be expected to be safe. This is consistent with experimental observations where smaller particles (in the nanometer-scale) have been shown to be more resistant to cracking than larger ones.[6] These results also suggest, as do experiments, that for high potential sweep rate applications, it is more important to use smaller particles. The stresses are lower in smaller particles because the increased surface to volume ratio results in a more uniform lithium concentration throughout the particle; the lower concentration gradient results in lower stresses. These results are for the extreme case of a particle that is permitted to expand freely. If the particle is constrained by a host matrix during insertion, the stresses will increase. We note, though, that this discussion, along with the analysis, has not considered surface stress effects which can be significant for nanometer-scale particles,[13,15] dependancies of the material parameters on phase-changes in the silicon, and on concentration and stress, and the effect of a surrounding matrix that may mechanically constrain the particle. If Li is extracted from an initially full particle, the processes reverse with stresses approximately equal in magnitude and of opposite sign.

The authors gratefully acknowledge the support of the Air Force Office of Scientific Research MURI (Grant No. F9550-06-1-0326) monitored by Dr. B. L. Lee, the National Science Foundation under CMMI Grant No. 0729520, and the first author acknowledges the support of a Graduate Research Fellowship from the National Science Foundation.

[1] M. Green, E. Fielder, B. Scrosati, M. Wachtler, and J. S. Moreno, Electrochem. Solid-State Lett. **6**, A75 (2003).
[2] U. Kasavajjula, C. Wang, and A. J. Appleby, J. Power Sources **163**, 1003 (2007).
[3] L. Baggetto, R. A. H. Niessen, F. Roozeboom, and P. H. L. Notten, Adv. Funct. Mater. **18**, 1057 (2008).
[4] C. K. Chan, H. Peng, G. Liu, K. McIlwrath, X. F. Zhang, R. A. Huggins, and Y. Cui, Nat. Nanotechnol. **3**, 31 (2008).
[5] B. A. Boukamp, G. C. Lesh, and R. A. Huggins, J. Electrochem. Soc. **128**, 725 (1981).
[6] H. Li, X. Huang, L. Chen, Z. Wu, and Y. Liang, Electrochem. Solid-State Lett. **2**, 547 (1999).
[7] L.-F. Cui, R. Ruffo, C. K. Chan, H. Peng, and Y. Cui, Nano Lett. **9**, 491 (2009).
[8] H. Kim, B. Han, J. Choo, and J. Cho, Angew. Chem., Int. Ed. **47**, 10151 (2008).
[9] J. Christensen and J. Newman, J. Solid State Electrochem. **10**, 293 (2006).
[10] J. Christensen and J. Newman, J. Electrochem. Soc. **153**, A1019 (2006).
[11] X. Zhang, W. Shyy, and A. M. Sastry, J. Electrochem. Soc. **154**, A910 (2007).
[12] X. Zhang, A. M. Sastry, and W. Shyy, J. Electrochem. Soc. **155**, 542 (2008).
[13] Y.-T. Cheng and M. W. Verbrugge, J. Appl. Phys. **104**, 083521 (2008).
[14] Y.-T. Cheng and M. W. Verbrugge, J. Power Sources **190**, 453 (2009).
[15] P. Sharma, S. Ganti, and N. Bhate, Appl. Phys. Lett. **82**, 535 (2003).
[16] J. Diao, K. Gall, and M. L. Dunn, Nature Mater. **2**, 656 (2003).
[17] J. Diao, K. Gall, and M. L. Dunn, J. Mech. Phys. Solids **52**, 1935 (2004).
[18] A. J. Bard and L. R. Faulkner, *Electrochemical Methods*, 2nd ed. (Wiley, New York, 2001).
[19] J. Newman and K. E. Thomas, *Electrochemical Systems*, 3rd ed. (Wiley, New York, 2004).
[20] D. Zhang, B. N. Popov, and R. E. White, J. Electrochem. Soc. **147**, 831 (2000).
[21] S. Golmon, K. Maute, and M. L. Dunn, Comput. Struc. **87**, 1567 (2009).
[22] N. Ding, J. Xu, Y. X. Yao, G. Wegner, X. Fang, C. H. Chen, and I. Lieberwirth, Solid State Ionics **180**, 222 (2009).
[23] "Matweb material property data," http://www.matweb.com/search/DataSheet.aspx?MatGUID=7d1b56e9e0c54ac5bb9cd433a0991e27&ckck=1
[24] *CRC Handbook of Chemistry and Physics*, 81st ed., edited by D. P. Lide (CRC, Boca-Raton, Florida, 2000).
[25] W. Suwito, M. L. Dunn, S. J. Cunningham, and D. T. Read, J. Appl. Phys. **85**, 3519 (1999).
[26] R. F. Cook, J. Mater. Sci. **41**, 841 (2006).

Appendix C

Publication: Multi-Scale Design Optimization of Lithium Ion Batteries with Adjoint Sensitivity Analysis

INTERNATIONAL JOURNAL FOR NUMERICAL METHODS IN ENGINEERING
Int. J. Numer. Meth. Engng 2012; **92**:475–494
Published online 7 June 2012 in Wiley Online Library (wileyonlinelibrary.com). DOI: 10.1002/nme.4347

Multiscale design optimization of lithium ion batteries using adjoint sensitivity analysis

Stephanie Golmon[1], Kurt Maute[1,*,†] and Martin L. Dunn[2]

[1]*Department of Aerospace Engineering, University of Colorado, Boulder, CO, USA*
[2]*Department of Mechanical Engineering, University of Colorado, Boulder, CO, USA*

SUMMARY

The capacity of lithium ion batteries can be improved through the use of functionally graded electrodes. Here, we present a computational framework for optimizing the layout of electrodes using a multiscale lithium ion battery cell model. The model accounts for nonlinear transient transport processes and mechanical deformations at multiple scales. A key component of the optimization methodology is the formulation of the adjoint sensitivity equations of the multiscale battery model. The efficient solution of the adjoint equations relies on the decomposition of the multiscale problem into multiple, computationally small problems associated with the individual realizations of the microscale model. This decomposition method is shown to significantly reduce the computational time needed for sensitivity analysis versus numerical finite differencing. The potential of the proposed optimization framework is illustrated with numerical problems involving both macroscale and microscale performance criteria and design variables. The usable capacity of a lithium ion battery cell is maximized while limiting the stress level in the electrode particles through manipulation of the local porosities and particle radii. The optimization results suggest that optimal functionally graded electrodes improve the performance of a battery cell over using uniform porosity and particle radius distributions. Copyright © 2012 John Wiley & Sons, Ltd.

Received 12 May 2011; Revised 6 January 2012; Accepted 5 April 2012

KEY WORDS: multiscale modeling; homogenization; finite element method; adjoint sensitivity analysis; stress–diffusion coupling

1. INTRODUCTION

In an increasingly mobile, energy-dependent society, there is a growing demand for more reliable, higher energy density, and longer lifetime batteries. Lithium-ion (Li^+) batteries are among the highest theoretical energy storage densities of modern batteries but are plagued with significantly shorter lifetimes when compared with other battery chemistries [1]. The performance and degradation of Li^+ batteries strongly depends on both electrochemical and mechanical phenomena. Figure 1 shows the layout of a typical Li^+ battery cell. When the battery is discharged, Li in the anode is oxidized into lithium ions, Li^+, and electrons. The electrons flow through the external circuit to the cathode while the ions enter the electrolyte and are carried by diffusion and migration to the cathode, where the ions are reduced. In most batteries, the electrodes are porous composites made of active insertion compounds, binders, and conductive additives, with liquid electrolyte filling the pores. The liquid volume fraction in the electrode is referred to as porosity, typically ranging between 30% and 50%. In the electrode, Li intercalates into the active material that causes the material to swell. Depending on the electrode material, this swelling ranges from 6.5% for Mn_2O_4 cathode material to 300%–400% for Si anode materials [2–4] and results in stresses that can lead to cracking of the

*Correspondence to: Kurt Maute, Center for Aerospace Structures, University of Colorado, CB 429, Boulder, CO 80301-0429, USA.
†E-mail: maute@colorado.edu

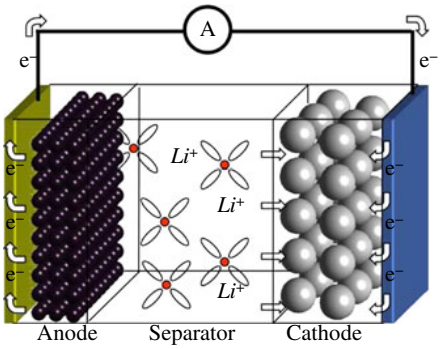

Figure 1. Battery cell.

active material particles. Experimental studies have linked capacity fade of batteries to crack growth in the electrodes [5] and shown that nonuniform straining of the particles within the electrode can lead to fracture of the particles [6].

The battery performance can be improved by altering design and discharge parameters [7]. Manipulation of parameters such as discharge rate, electrode thickness, porosity, and size and shape of the electrode particles can affect the overall behavior of the battery and the internal stress levels. As the battery performance depends on nonlinear transient processes at multiple length-scales, designing by intuition is difficult. To support the engineer in designing battery cells, we propose a formal design optimization methodology to find optimal electrode layouts. Our approach combines numerical models to predict the battery performance with mathematical optimization schemes to drive the cell design.

Much of the previous work on improving the performance of batteries has focused on battery pack rather than a single battery cell design, considering thermal [8, 9] and power management [10] effects. To enhance the battery performance at the cell level, the specific energy was increased by studying the relationship between porosity and electronic and ionic conductivities [11]. The ohmic drop across the cell was reduced by fine tuning the porosity distributions in the electrodes [12]. Du *et al.* [13] used surrogate models to study the influence of several parameters including the cycling rate and particle size on the specific energy and power of a battery cell and to identify the Pareto-optimal relationship between specific energy and power of the cell. All of the above design studies rely primarily on intuition, experience, and parameter sweeps but do not employ directly a formal optimization approach for designing battery cells.

Our goal is to develop a computational framework for optimizing the electrode structure of a battery cell to improve the electrochemical and mechanical performances. The behavior of Li^+ batteries is an interesting multiscale, multiphysics problem, in which the electrochemical and mechanical phenomena are coupled, transient and nonlinear. Macroscale phenomena include Li^+ transport, electric potentials, and mechanical deformations across the battery cell. These phenomena are strongly coupled with the response of the active electrode particles at the microscale. Directly resolving the length-scales relevant for describing the electrochemical and mechanical performances of a battery cell leads to a large computational burden. Instead, we use a multiscale modeling approach, assuming a separation of length-scales between macroscale and microscales. For the model presented here, a separation of time scales is not needed as the Li^+ transport at both the macroscale and microscale occurs at similar rates. Mesoscale homogenization methods are used to account for the interactions between particles and relate the macroscale and microscale phenomena.

To handle a potentially large number of design variables, we consider gradient-based design optimization schemes to minimize an objective, Z, subject to inequality constraints, G_j, by varying

DOI: 10.1002/nme

continuous design variables, $\mathbf{s} \in \Re^{N_s}$:

$$\begin{aligned} \min_{\mathbf{s}} \; & Z(\mathbf{x}, \mathbf{y}, \mathbf{s}) = \int \mathcal{F}(\mathbf{x}, \mathbf{y}, \mathbf{s}) \, \mathrm{d}t \\ \text{s.t. } & G_j(\mathbf{x}, \mathbf{y}, \mathbf{s}) = \int \mathcal{G}_j(\mathbf{x}, \mathbf{y}, \mathbf{s}) \, \mathrm{d}t \leqslant 0 \quad j = 1 : N_g \\ & s_i^L \leqslant s_i \leqslant s_i^U \quad i = 1 : N_s, \end{aligned} \tag{1}$$

where $\mathbf{x}$ represents the macroscale state variables and $\mathbf{y}$ the microscale state variables. The objective and constraints are differentiable functions that depend on both state and design variables. The time-integral formulation allows accounting for both average performance measures and quantities at distinct points in time. The lower and upper bounds for the optimization variables are denoted by s_i^L and s_i^U, respectively.

The design optimization problem is solved by a nonlinear programming method that requires the gradients of the objective and constraints with respect to the design variables. The computational complexity of the multiscale battery model necessitates the use of analytical sensitivities. In this paper, we develop the multiscale, transient, adjoint sensitivity equations, in which the optimization criteria can characterize electrochemical or mechanical phenomena such as the battery potential and stress levels in the electrode. Design variables can include both macroscale and microscale parameters such as the local macroscale electrode porosities and microscale particle radii. The mathematical structure of the multiscale, transient, adjoint sensitivity equations, allows for decomposing the fully coupled problem into multiple, independent, and smaller problems at two scales. Therefore, the proposed adjoint sensitivity analysis method is applicable to spatially and temporally well-resolved multiscale problems with a large number of design variables. We will show that the adjoint approach significantly reduces the computational costs of computing design sensitivities versus finite differencing.

The remainder of this paper is organized as follows. The multiscale model is presented in Section 2. In Section 3, we derive the multiscale adjoint sensitivity equations. In Section 4, we present numerical results for battery optimization using both macroscale and microscale design criteria and variables.

2. MULTISCALE BATTERY MODEL

The multiscale framework presented in this paper is built upon a coupled electrochemical–mechanical model of Li^+ batteries. This model extends the electrochemical battery model developed by Doyle *et al.* [14–18], which uses porous electrode theory to account for microscale effects [18, 19]. We extend this model to account for elastic and inelastic deformations due to external mechanical loads and electrochemical eigenstrains. The response of the electrode particles is described by the coupled stress–diffusion model of Zhang *et al.* [2] and accounts for electrochemical surface reactions. Discharge curves generated by the electrochemical portion of this model have been qualitatively compared with experimental studies showing similar results.[14]

The aforementioned battery model problem involves two distinct length-scales: the macroscale includes transport processes and mechanical deformation of the anode, the separator/electrolyte, and cathode; and the microscale considers a single representative active material particle in the cathode. An overview of numerical multiscale modeling methods can be found in Kanoute *et al.* [20]. Our numerical battery model follows the work of Miehe *et al.* [21, 22] and Feyel [23–25], using finite element models at both the macroscale and microscales bridged by volume averaging homogenization methods [26–28]. At a given material point in the macroscale model, the local, volume averaged response of the microscale model is evaluated. Here, we build upon our previous work on multiscale battery modeling [7] and extend our original model to include surface stress effects. As we will show later, surface stress effects need to be considered when optimizing the size of electrode particles to avoid nonphysical solutions that incorrectly favor vanishing particle sizes. In the following subsections, we summarize the key elements of our multiscale battery model

DOI: 10.1002/nme

to keep this paper self-contained and to allow for the derivation of the multiscale adjoint sensitivity analysis presented in Section 3. A summary of symbols used is given in the Appendix A.

2.1. Governing equations at the macroscale

At the macroscale, we model the Li^+ concentration in the electrolyte, c_l, the electric potentials in the solid, ϕ_1, and liquid, ϕ_2, phases, and the displacements, $\mathbf{u}$. To simplify the macroscale model, we consider only a half cell and replace the anode by a Li foil which is modeled via flux and current boundary conditions at the separator-anode interface. The diffusion and migration of Li^+ in the electrolyte are described by

$$R_{c_l}: \int_\Omega \delta c_l \, \varepsilon \frac{\partial c_l}{\partial t} \mathrm{d}\Omega - \int_\Omega \delta \nabla c_l \, \mathbf{N} \mathrm{d}\Omega + \int_\Omega \delta c_l \left(\frac{1}{F} \frac{\partial t_+^0}{\partial c_l} \, \mathbf{i_2} \cdot \nabla c_l - (1 - t_+^0) \, j_{\text{eff}} \right) \mathrm{d}\Omega - \int_{\Gamma_{x_A}} \delta c_l \frac{\mathbf{I}(1 - t_+^0)}{F} \, \hat{\mathbf{n}} \, \mathrm{d}\Gamma_{x_A} = 0, \tag{2}$$

where $\mathbf{N}$ is the diffusive flux, t_+^0 is the Li^+ transference number, F is the Faraday constant, and Γ_{x_A} denotes the boundary at the anode–separator interface. The third term accounts for the migration of ions and the volume averaged flux of Li^+, j_{eff}, from the electrolyte into the electrode particles. The last term stems from a Neumann boundary condition that models the influx of ions at the anode–separator interface due to a prescribed current, $\mathbf{I}$.

The potential in the solid phase is governed by Ohm's law:

$$R_{\phi_1}: -\int_\Omega \delta \nabla \phi_1 \, \mathbf{i}_1 \mathrm{d}\Omega + \int_\Omega \delta \phi_1 \, F \, j_{\text{eff}} \mathrm{d}\Omega + \int_{\Gamma_{x_C}} \delta \phi_1 \, \mathbf{I} \, \hat{\mathbf{n}} \, \mathrm{d}\Gamma_{x_C} = 0, \tag{3}$$

where Γ_{x_C} denotes the boundary at the cathode–current collector interface. The source term accounts for the effects of Li entering and exiting the solid phase, whereas the last term stems from a Neumann boundary condition for the influx of electrons at the cathode–current collector interface. Similarly, the liquid potential is governed by a modified Ohm's law accounting for the dependence of the current on the Li^+ concentration:

$$R_{\phi_2}: -\int_\Omega \delta \nabla \phi_2 \, \mathbf{i}_2 \mathrm{d}\Omega - \int_\Omega \delta \phi_2 \, F j_{\text{eff}} \mathrm{d}\Omega + \int_{\Gamma_{x_A}} \delta \phi_2 \, \mathbf{I} \, \hat{\mathbf{n}} \, \mathrm{d}\Gamma_{x_A} = 0. \tag{4}$$

To define a reference liquid potential, a Dirichlet boundary condition is imposed at the separator–cathode interface, fixing the liquid potential at zero.

The macroscale mechanical response is assumed to be linear elastic using a volume-averaged eigenstrain model to account for the swelling of the active electrode particles:

$$R_{\mathbf{u}}: \int_\Omega \delta \mathbf{e} \, \boldsymbol{\sigma} \, \mathrm{d}\Omega = 0, \tag{5}$$

where $\boldsymbol{\sigma}$ and $\mathbf{e}$ are the macroscopic stress and strain tensors, respectively. The displacements are fixed at zero at Γ_{x_A} and Γ_{x_C}.

Constitutive equations for the macroscale model include the diffusive flux, electric and ionic currents, and stress and strains:

$$\mathbf{N} = -D_{\text{eff}} \nabla c_l, \tag{6}$$

$$\mathbf{i}_1 = -\lambda \nabla \phi_1, \tag{7}$$

$$\mathbf{i}_2 = -\kappa_{\text{eff}} \left(\nabla \phi_2 - \frac{RT}{F} (1 - t_+^0) \nabla, \ln(c_l) \right), \tag{8}$$

$$\boldsymbol{\sigma} = \mathbf{C}_{\text{eff}} \, (\mathbf{e} - \mathbf{e}_{\text{ch}}), \quad \mathbf{e} = \frac{1}{2} \left(\nabla \mathbf{u} + \nabla \mathbf{u}^T \right), \tag{9}$$

DOI: 10.1002/nme

where D_{eff} is the effective macroscale diffusion coefficient of Li^+ in the electrolyte, λ is the electric conductivity of the solid particles, κ_{eff} is the effective ionic conductivity of the electrolyte, $\mathbf{C}_{\text{eff}}$ is the homogenized elasticity tensor, and $\mathbf{e}_{\text{ch}}$ is the volume-averaged chemically induced eigenstrain due to the aggregate swelling.

2.2. Governing equations at the microscale

At the microscale, we consider a single spherical particle of active material embedded in an electrolyte host. We assume that the macroscale concentration, potential, and displacement fields are spatially constant in the electrolyte surrounding the particle. This results in uniform boundary conditions on the particle and allows for simplification of the problem to one dimension using spherical coordinates. Considering more general models with other particle geometries is straightforward [29]. The single particle is modeled on the basis of the work of Zhang *et al.* [2] and extended to include Butler–Volmer surface kinetics and surface pressure. The microscale state variables include the microscopic Li concentration in the particle, c_{s}, the microscopic radial displacements, u_{r}, the hydrostatic stress field, σ_{h}, and the microscopic pore wall flux, j_{s}.

The concentration and deformation fields in the particle are described by the following diffusion and linear static mechanical models:

$$R_{c_{\text{s}}}: \int_r 4\pi r^2 \left(\delta c_{\text{s}} \frac{\partial c_{\text{s}}}{\partial t}\right) \mathrm{d}r - \int_r 4\pi r^2 \left(\delta \nabla_{\text{r}} c_{\text{s}} \mathbf{J}\right) \mathrm{d}r + 4\pi R_{\text{s}}^2 j_{\text{s}} = 0, \tag{10}$$

$$R_{u_{\text{r}}}: \int_r 4\pi r^2 \delta \nabla u_{\text{r}} \sigma_R \mathrm{d}r + \int_r \delta u_{\text{r}} 8\pi r \sigma_T \mathrm{d}r - 4\pi R_{\text{s}}^2 P_{\text{micro}} = 0, \tag{11}$$

with the following constitutive equations:

$$\mathbf{J} = -D_{\text{s}} \left(\nabla_{\text{r}} c_{\text{s}} - \frac{\Omega_{\text{Li}} c_{\text{s}}}{RT} \nabla_{\text{r}} \sigma_{\text{h}}\right), \tag{12}$$

$$\sigma_{\text{R}} = \frac{E_{\text{s}}}{(1+\nu)(1-2\nu)} \left((1-\nu)\nabla_{\text{r}} u_{\text{r}} + 2\nu \frac{u_{\text{r}}}{r} - \frac{\Omega_{\text{Li}}}{3} c_{\text{s}}(1+\nu)\right), \tag{13}$$

$$\sigma_{\text{T}} = \frac{E_{\text{s}}}{(1+\nu)(1-2\nu)} \left(\frac{u_{\text{r}}}{r} + \nu \nabla_{\text{r}} u_{\text{r}} - \frac{\Omega_{\text{Li}}}{3} c_{\text{s}}(1+\nu)\right). \tag{14}$$

The stress–diffusion coupling increases with the Li partial molar volume, Ω_{Li}. Accounting for the spherical symmetry, the displacement at the center of the particle is fixed at zero.

The Li^+ flux at the particle surface, j_{s}, is described by the Butler–Volmer surface kinetics model that depends on both the macroscopic Li^+ concentration and electric potentials as well as the microscopic Li concentration at the particle surface:

$$F\ j_{\text{s}} - i_0 \left[c_{\text{s}|\text{r}=R_{\text{s}}}\ e^{k_1} - \left(c_{\text{s,max}} - c_{\text{s}|\text{r}=R_{\text{s}}}\right)\ e^{k_2}\right] = 0, \tag{15}$$

with

$$k_1 = \frac{\alpha_{\text{A}} F}{RT} \left(\eta - U'(c_{\text{s}|\text{r}=R_{\text{s}}})\right), \tag{16}$$

$$k_2 = -\frac{\alpha_{\text{C}} F}{RT} \left(\eta - U'(c_{\text{s}|\text{r}=R_{\text{s}}})\right), \tag{17}$$

$$i_0 = F k_2 \left(c_{\text{l,max}} - c_{\text{l}}\right)^{\alpha_{\text{C}}} \left(c_{\text{l}}\right)^{\alpha_{\text{A}}}, \tag{18}$$

$$\eta = \phi_1 - \phi_2. \tag{19}$$

DOI: 10.1002/nme

The surface pressure at the particle surface includes contributions from swelling neighboring particles, P_{h}, which is found via a homogenization method (Section 2.3), and from surface stress, P_{SS}:

$$P_{\mathrm{micro}} = P_{\mathrm{h}} + P_{\mathrm{SS}}. \tag{20}$$

For spherical particles, the pressure due to the surface stress effect can be written as follows:[30]

$$P_{\mathrm{SS}} = -2\frac{\tau_0 + K^{\mathrm{s}}\varepsilon_{\mathrm{t}}\,|_{r=R_{\mathrm{s}}}}{R_{\mathrm{s}}}, \tag{21}$$

where τ_0 is the deformation-independent surface tension, K^s is the surface modulus, and ε_t is the tangential strain, which in spherical coordinates is

$$\varepsilon_{\mathrm{t}} = \frac{u_{\mathrm{r}}}{r}. \tag{22}$$

To simplify the numerical implementation by limiting the spatial derivatives in the diffusion Equations (10) and (12) to first order, we introduce the hydrostatic stress as an independent field. The hydrostatic stress equation is satisfied in a weak sense:

$$R_{\sigma_{\mathrm{h}}}: \int_r 4\pi r^2 \delta\sigma_{\mathrm{h}} \left(\sigma_{\mathrm{h}} - \left(\sigma_{\mathrm{R}} + 2\sigma_{\mathrm{T}}\right)/3\right) \mathrm{d}r = 0. \tag{23}$$

2.3. Mesoscale homogenization

To bridge the microscale and macroscale models, the mechanical phenomena are homogenized via Mori–Tanaka aggregate theory [26], and Bruggeman relations [14, 18] are used to upscale transport properties. The effective pore wall flux, j_{eff}, in the macroscale equations is related to the microscale pore wall flux, j_{s}, through

$$j_{\mathrm{eff}} = \frac{3(1-\varepsilon)}{R_{\mathrm{s}}} j_{\mathrm{s}}. \tag{24}$$

The effective properties D_{eff} and κ_{eff} are modeled via Bruggeman relations based on the diffusion coefficient, D_{l}, and the conductivity, κ_∞, of the bulk electrolyte:

$$D_{\mathrm{eff}} = \varepsilon D_{\mathrm{l}}, \tag{25}$$

$$\kappa_{\mathrm{eff}} = \varepsilon^{3/2}\kappa_\infty. \tag{26}$$

The Mori–Tanaka homogenization model [26–28] couples the microscale particle deformations and the resulting surface pressure, P_{h}, with the macroscale chemical eigenstrain, $\mathbf{e}_{\mathrm{ch}}$. Accounting for the swelling of neighboring particles, the microscale surface pressure is

$$P_{\mathrm{h}} = \left(\mathbf{b}_{\mathrm{s}} + \mathbf{B}_{\mathrm{s}}\mathbf{C}_{\mathrm{eff}}\left(\mathbf{e} - \mathbf{e}_{\mathrm{ch}}\right)\right)\hat{\mathbf{n}}, \tag{27}$$

where $\mathbf{e}_{\mathrm{ch}}$ is defined as

$$\mathbf{e}_{\mathrm{ch}} = (1-\varepsilon)\,\mathbf{e}_{\mathrm{V}} + (1-\varepsilon)\left(\mathbf{C}_{\mathrm{s}}^{-1} - \mathbf{C}_{\mathrm{l}}^{-1}\right)\mathbf{b}_{\mathrm{s}}, \tag{28}$$

with

$$\mathbf{b}_{\mathrm{s}} = (\mathbf{I} - \mathbf{B}_{\mathrm{s}})\left(\mathbf{C}_{\mathrm{l}}^{-1} - \mathbf{C}_{\mathrm{s}}^{-1}\right)\mathbf{e}_{\mathrm{V}}, \tag{29}$$

$$\mathbf{B}_{\mathrm{s}} = \mathbf{B}_D\left(\varepsilon\mathbf{I} + (\mathbf{I}-\varepsilon)\mathbf{B}_D\right)^{-1}, \tag{30}$$

$$\mathbf{B}_D = \mathbf{C}_{\mathrm{s}}\left(\mathbf{I} + \mathbf{S}\mathbf{C}_{\mathrm{l}}^{-1}\left(\mathbf{C}_{\mathrm{s}}^{-1} - \mathbf{C}_{\mathrm{l}}^{-1}\right)\right)^{-1}\mathbf{C}_{\mathrm{l}}^{-1}. \tag{31}$$

The microscale volumetric strain, $\mathbf{e}_{\mathrm{V}}$ is found via

$$\mathbf{e}_{\mathrm{V}} = \frac{1}{3}\left(\frac{\left(R_{\mathrm{s}} + u_{\mathrm{r}=R_{\mathrm{s}}}\right)^3}{R_{\mathrm{s}}^3} - 1\right). \tag{32}$$

Note that in the aforementioned homogenization model, we assume there is no chemically induced strain in the electrolyte.

DOI: 10.1002/nme

2.4. Spatial and temporal discretization

The design and operation of a typical Li^+ battery cell allows for the following simplifications of the multiscale battery model. The distance through the thickness of a battery cell from the anode to cathodic current collector is significantly smaller than the overall size of a typical Li^+ battery cell, which allows for an idealization of the problem to one dimension at the macroscale. In a typical charge or discharge process, the diffusion processes at both length-scales operate on comparable time scales; therefore, a separation in time scales is not needed.

At both scales, we discretize the governing equations in space using finite elements and in time with an implicit Euler backwards scheme [7]. Within the cathode, separate microscale problems are solved at the macroscale integration points. The microscale problems are independent of each other, only coupled through the macroscale model. The resulting discretized governing equations can be written in compact form as follows:

$$\mathbf{R}_{\mathbf{x}}^{n+1} : \mathbf{M}_{\mathbf{x}}^{n+1} \left(\mathbf{x}^{n+1} - \mathbf{x}^{n}\right) / \Delta t + \mathbf{R}_{\mathbf{x},st}^{n+1} \left(\mathbf{x}^{n+1}, \mathbf{y}^{n+1}\right) = \mathbf{0}, \tag{33}$$

$$\mathbf{R}_{\mathbf{y}_i}^{n+1} : \mathbf{M}_{\mathbf{y}_i}^{n+1} \left(\mathbf{y}_i^{n+1} - \mathbf{y}_i^{n}\right) / \Delta t + \mathbf{R}_{\mathbf{y}_i,st}^{n+1} \left(\mathbf{y}_i^{n+1}, \mathbf{x}^{n+1}\right) = \mathbf{0},\ i = 1 : N_{\mathrm{m}}, \tag{34}$$

where $\mathbf{R}_{\mathbf{x}}^{n+1}$ represents the macroscale residual Equations, (2)–(5), and $\mathbf{R}_{\mathbf{y}_i}^{n+1}$ collects the microscale residual Equations, (10), (11), and (23); the vector of all macroscale variables at time n is $\mathbf{x}^n$, and the vector of variables for a single microscale problem, i, at time n is $\mathbf{y}_i^n$. The vector of all microscale variables at time n, $\mathbf{y}^n$, collects the vectors of microscale states for all microscale problems, $\mathbf{y}^n = \left[\mathbf{y}_1^n,\ \mathbf{y}_2^n,\ \ldots, \mathbf{y}_{N_{\mathrm{m}}}^n\right]$, where N_{m} is the number of microscale problems. $\mathbf{M}_{\mathbf{x}}^{n+1}$ and $\mathbf{M}_{\mathbf{y}_i}^{n+1}$ are the macroscale and microscale capacitance matrices, and $\mathbf{R}_{\mathbf{x},st}^{n+1}$ and $\mathbf{R}_{\mathbf{y}_i,st}^{n+1}$ are the macroscale and microscale static contributions to the residual equations.

The aforementioned system of equations can be solved either by advancing macroscale and microscales simultaneously or via a staggered approach in which the microscale state variables are considered functions of the macroscale state variables, that is, $\mathbf{y}_i^n(\mathbf{x}^n)$. For the forward problem, the staggered approach is used as it naturally leads to a separation of the problem into multiple smaller microscale problems and facilitates parallel computing schemes. At every time step, Newton's method is used to solve for $\mathbf{x}^{n+1}$ at the macroscale; within every macroscale Newton iteration, the microscale problems are solved for $\mathbf{y}_i^{n+1}$ also by Newton's method. For computational efficiency, the macroscale and microscale Jacobians of the governing Equations (33) and (34) are derived analytically.

3. ADJOINT SENSITIVITY ANALYSIS

In time-discrete form, the optimization problem, (1), can be written as follows:

$$\begin{aligned} \min_{\mathbf{s}}\ & Z\left(\tilde{\mathbf{x}}, \tilde{\mathbf{y}}, \mathbf{s}\right) = \sum_{n=0}^{N_{\mathrm{t}}} \mathcal{F}^n\left(\mathbf{x}^n, \mathbf{y}^n, \mathbf{s}\right) dt \\ s.t.\ & G_j\left(\tilde{\mathbf{x}}, \tilde{\mathbf{y}}, \mathbf{s}\right) = \sum_{n=0}^{N_{\mathrm{t}}} \mathcal{G}_j^n\left(\mathbf{x}^n, \mathbf{y}^n, \mathbf{s}\right) dt \leqslant 0\ \ \forall\ j = 1 : N_{\mathrm{g}}, \end{aligned} \tag{35}$$

where the macroscale and microscale state variables, $\mathbf{x}^n$ and $\mathbf{y}^n$, satisfy the governing Equations (33) and (34) at time steps $n = 1 : N_t$. The vector $\tilde{\mathbf{x}}$ collects macroscale variables at all times, and the vector $\tilde{\mathbf{y}}$ collects all microscale variables of all time steps:

$$\begin{aligned} \tilde{\mathbf{x}} &= \left[\mathbf{x}^0, \mathbf{x}^1, \ldots, \mathbf{x}^{N_{\mathrm{t}}}\right] \\ \tilde{\mathbf{y}} &= \left[\mathbf{y}^0, \mathbf{y}^1, \ldots, \mathbf{y}^{N_{\mathrm{t}}}\right]. \end{aligned} \tag{36}$$

The gradients $\mathrm{d}Z/\mathrm{d}s_i$ and $\mathrm{d}G_j/\mathrm{d}s_i$ are needed for gradient-based optimization. We compute these gradients by deriving and solving the adjoint sensitivity equations of the multiscale battery model described in Section 2.

DOI: 10.1002/nme

For the sensitivity analysis, it is more convenient to treat the macroscale and microscale variables as independent instead of using the staggered approach that is used for the forward analysis. We derive the design sensitivities explicitly for the objective, Z; the analysis for the constraints, G_j, is analogous.

$$\frac{\mathrm{d}Z}{\mathrm{d}s_i} = \frac{\partial Z}{\partial s_i} + \begin{bmatrix} \dfrac{\partial Z}{\partial \tilde{\mathbf{x}}} \\ \dfrac{\partial Z}{\partial \tilde{\mathbf{y}}} \end{bmatrix}^T \begin{bmatrix} \dfrac{\mathrm{d}\tilde{\mathbf{x}}}{\mathrm{d}s_i} \\ \dfrac{\mathrm{d}\tilde{\mathbf{y}}}{\mathrm{d}s_i} \end{bmatrix} \quad i = 1 : N_\mathrm{s}. \tag{37}$$

We evaluate the sensitivities at dynamic equilibrium; therefore, the macroscale and microscale residuals vanish for all time steps:

$$\begin{bmatrix} \tilde{\mathbf{R}}_{\tilde{\mathbf{x}}} \\ \tilde{\mathbf{R}}_{\tilde{\mathbf{y}}} \end{bmatrix} = \begin{bmatrix} \mathbf{0} \\ \mathbf{0} \end{bmatrix}, \tag{38}$$

where the vectors $\tilde{\mathbf{R}}_{\tilde{\mathbf{x}}}$ and $\tilde{\mathbf{R}}_{\tilde{\mathbf{y}}}$ are arranged as in (36). Differentiating the state Equation (38) with respect to s_i leads to

$$\begin{bmatrix} \dfrac{\mathrm{d}\tilde{\mathbf{R}}_{\tilde{\mathbf{x}}}}{\mathrm{d}s_i} \\ \dfrac{\mathrm{d}\tilde{\mathbf{R}}_{\tilde{\mathbf{y}}}}{\mathrm{d}s_i} \end{bmatrix} = \begin{bmatrix} \mathbf{0} \\ \mathbf{0} \end{bmatrix} \Longrightarrow \begin{bmatrix} \dfrac{\partial \tilde{\mathbf{R}}_{\tilde{\mathbf{x}}}}{\partial s_i} \\ \dfrac{\partial \tilde{\mathbf{R}}_{\tilde{\mathbf{y}}}}{\partial s_i} \end{bmatrix} + \begin{bmatrix} \dfrac{\partial \tilde{\mathbf{R}}_{\tilde{\mathbf{x}}}}{\partial \tilde{\mathbf{x}}} & \dfrac{\partial \tilde{\mathbf{R}}_{\tilde{\mathbf{x}}}}{\partial \tilde{\mathbf{y}}} \\ \dfrac{\partial \tilde{\mathbf{R}}_{\tilde{\mathbf{y}}}}{\partial \tilde{\mathbf{x}}} & \dfrac{\partial \tilde{\mathbf{R}}_{\tilde{\mathbf{y}}}}{\partial \tilde{\mathbf{y}}} \end{bmatrix} \begin{bmatrix} \dfrac{\mathrm{d}\tilde{\mathbf{x}}}{\mathrm{d}s_i} \\ \dfrac{\mathrm{d}\tilde{\mathbf{y}}}{\mathrm{d}s_i} \end{bmatrix} = \begin{bmatrix} \mathbf{0} \\ \mathbf{0} \end{bmatrix}. \tag{39}$$

We symbolically solve for $[\mathrm{d}\tilde{\mathbf{x}}/\mathrm{d}s_i \ \mathrm{d}\tilde{\mathbf{y}}/\mathrm{d}s_i]^T$ and substitute the result into (37) yielding the sensitivity equation in terms of the macroscale and microscale governing equations:

$$\frac{\mathrm{d}Z}{\mathrm{d}s_i} = \frac{\partial Z}{\partial s_i} - \begin{bmatrix} \dfrac{\partial Z}{\partial \tilde{\mathbf{x}}} \\ \dfrac{\partial Z}{\partial \tilde{\mathbf{y}}} \end{bmatrix}^T \begin{bmatrix} \dfrac{\partial \tilde{\mathbf{R}}_{\tilde{\mathbf{x}}}}{\partial \tilde{\mathbf{x}}} & \dfrac{\partial \tilde{\mathbf{R}}_{\tilde{\mathbf{x}}}}{\partial \tilde{\mathbf{y}}} \\ \dfrac{\partial \tilde{\mathbf{R}}_{\tilde{\mathbf{y}}}}{\partial \tilde{\mathbf{x}}} & \dfrac{\partial \tilde{\mathbf{R}}_{\tilde{\mathbf{y}}}}{\partial \tilde{\mathbf{y}}} \end{bmatrix}^{-1} \begin{bmatrix} \dfrac{\partial \tilde{\mathbf{R}}_{\tilde{\mathbf{x}}}}{\partial s_i} \\ \dfrac{\partial \tilde{\mathbf{R}}_{\tilde{\mathbf{y}}}}{\partial s_i} \end{bmatrix}. \tag{40}$$

If the number of optimization variables, N_s, exceeds the number of constraints, N_g, the sensitivity Equation (40) can be solved efficiently by the adjoint approach. Introducing the macroscale and microscale adjoint states, $\boldsymbol{\lambda}_{\tilde{\mathbf{x}}}$ and $\boldsymbol{\lambda}_{\tilde{\mathbf{y}}}$:

$$\begin{bmatrix} \dfrac{\partial \tilde{\mathbf{R}}_{\tilde{\mathbf{x}}}}{\partial \tilde{\mathbf{x}}} & \dfrac{\partial \tilde{\mathbf{R}}_{\tilde{\mathbf{x}}}}{\partial \tilde{\mathbf{y}}} \\ \dfrac{\partial \tilde{\mathbf{R}}_{\tilde{\mathbf{y}}}}{\partial \tilde{\mathbf{x}}} & \dfrac{\partial \tilde{\mathbf{R}}_{\tilde{\mathbf{y}}}}{\partial \tilde{\mathbf{y}}} \end{bmatrix}^T \begin{bmatrix} \boldsymbol{\lambda}_{\tilde{\mathbf{x}}} \\ \boldsymbol{\lambda}_{\tilde{\mathbf{y}}} \end{bmatrix} = \begin{bmatrix} \dfrac{\partial Z}{\partial \tilde{\mathbf{x}}} \\ \dfrac{\partial Z}{\partial \tilde{\mathbf{y}}} \end{bmatrix}, \tag{41}$$

the sensitivity Equation (40) becomes

$$\frac{\mathrm{d}Z}{\mathrm{d}s_i} = \frac{\partial Z}{\partial s_i} - \begin{bmatrix} \boldsymbol{\lambda}_{\tilde{\mathbf{x}}} \\ \boldsymbol{\lambda}_{\tilde{\mathbf{y}}} \end{bmatrix}^T \begin{bmatrix} \dfrac{\partial \tilde{\mathbf{R}}_{\tilde{\mathbf{x}}}}{\partial s_i} \\ \dfrac{\partial \tilde{\mathbf{R}}_{\tilde{\mathbf{y}}}}{\partial s_i} \end{bmatrix}. \tag{42}$$

The adjoint states are computed by expanding (41) into time steps and integrating the discrete adjoint problem backwards in time:

$$\begin{bmatrix} \mathbf{J}_{\mathbf{x}}^n & \dfrac{\partial \mathbf{R}_{\mathbf{x},st}^n}{\partial \mathbf{y}^n} \\ \dfrac{\partial \mathbf{R}_{\mathbf{y},st}^n}{\partial \mathbf{x}^n} & \mathbf{J}_{\mathbf{y}}^n \end{bmatrix}^T \begin{bmatrix} \boldsymbol{\lambda}_{\mathbf{x}}^n \\ \boldsymbol{\lambda}_{\mathbf{y}}^n \end{bmatrix} = \begin{bmatrix} \dfrac{\partial \mathcal{F}^n}{\partial \mathbf{x}^n} \\ \dfrac{\partial \mathcal{F}^n}{\partial \mathbf{y}^n} \end{bmatrix} + \begin{bmatrix} \dfrac{M_{\mathbf{x}}^{n+1}}{\Delta t} & \mathbf{0} \\ \mathbf{0} & \dfrac{M_{\mathbf{y}}^{n+1}}{\Delta t} \end{bmatrix}^T \begin{bmatrix} \boldsymbol{\lambda}_{\mathbf{x}}^{n+1} \\ \boldsymbol{\lambda}_{\mathbf{y}}^{n+1} \end{bmatrix}, \tag{43}$$

DOI: 10.1002/nme

where $\mathbf{J}_{\mathbf{x}}^n = M_{\mathbf{x}}^n/\Delta t + \partial \mathbf{R}_{\mathbf{x},st}^n/\partial \mathbf{x}^n$ and $\mathbf{J}_{\mathbf{y}}^n = M_{\mathbf{y}}^n/\Delta t + \partial \mathbf{R}_{\mathbf{y},st}^n/\partial \mathbf{y}^n$ are the dynamic macroscale and microscale Jacobians. These matrices are rebuilt using the states computed and stored in the forward problem. We solve the system of (43) for $\boldsymbol{\lambda}_{\mathbf{x}}^n$ by first eliminating $\boldsymbol{\lambda}_{\mathbf{y}}^n$:

$$\boldsymbol{\lambda}_{\mathbf{x}}^n = \left[\left(\mathbf{J}_{\mathbf{x}}^n\right)^T - \mathbf{c}_1\right]^{-1} \left(\frac{\partial \mathcal{F}^n}{\partial \mathbf{x}^n} + \left(\frac{M_{\mathbf{x}}^{n+1}}{\Delta t}\right)^T \boldsymbol{\lambda}_{\mathbf{x}}^{n+1} - \mathbf{c}_2\right), \tag{44}$$

where

$$\mathbf{c}_1 = \left(\frac{\partial \mathbf{R}_{\mathbf{y},st}^n}{\partial \mathbf{x}^n}\right)^T \left(\left(\mathbf{J}_{\mathbf{y}}^n\right)^T\right)^{-1} \left(\frac{\partial \mathbf{R}_{\mathbf{x},st}^n}{\partial \mathbf{y}^n}\right)^T, \tag{45}$$

$$\mathbf{c}_2 = \left(\frac{\partial \mathbf{R}_{\mathbf{y},st}^n}{\partial \mathbf{x}^n}\right)^T \left(\left(\mathbf{J}_{\mathbf{y}}^n\right)^T\right)^{-1} \left(\frac{\partial \mathcal{F}^n}{\partial \mathbf{y}^n} + \left(\frac{M_{\mathbf{y}}^{n+1}}{\Delta t}\right)^T \boldsymbol{\lambda}_{\mathbf{y}}^{n+1}\right). \tag{46}$$

The calculation of the matrices $\mathbf{c}_1$ and $\mathbf{c}_2$ requires solving linear systems of the size of all microscale state variables. The computational burden associated with this step can be reduced owing to the independence of the microscale problems. The microscale problems are only coupled through the macroscale model; consequently, the matrices $\mathbf{J}_{\mathbf{y}}^n$ and $\mathbf{M}_{\mathbf{y}}^n$ are block diagonal with each block being the microscale dynamic Jacobian, $\mathbf{J}_{\mathbf{y}_i}^n$, and capacitance matrix, $\mathbf{M}_{\mathbf{y}_i}^n$, for a single microscale problem, i:

$$\mathbf{J}_{\mathbf{y}}^n = \begin{bmatrix} \mathbf{J}_{\mathbf{y}_1}^n & \mathbf{0} & \dots & \mathbf{0} \\ \mathbf{0} & \mathbf{J}_{\mathbf{y}_2}^n & \dots & \mathbf{0} \\ \vdots & \vdots & \ddots & \vdots \\ \mathbf{0} & \mathbf{0} & \dots & \mathbf{J}_{\mathbf{y}_{N_\mathrm{m}}}^n \end{bmatrix}, \quad \mathbf{M}_{\mathbf{y}}^n = \begin{bmatrix} \mathbf{M}_{\mathbf{y}_1}^n & \mathbf{0} & \dots & \mathbf{0} \\ \mathbf{0} & \mathbf{M}_{\mathbf{y}_2}^n & \dots & \mathbf{0} \\ \vdots & \vdots & \ddots & \vdots \\ \mathbf{0} & \mathbf{0} & \dots & \mathbf{M}_{\mathbf{y}_{N_\mathrm{m}}}^n \end{bmatrix}. \tag{47}$$

Furthermore, the macro–micro coupling Jacobians, $\partial \mathbf{R}_{\mathbf{y},st}^n/\partial \mathbf{x}^n$ and $\partial \mathbf{R}_{\mathbf{x},st}^n/\partial \mathbf{y}^n$, are sparse with a rectangular band structure. The block diagonal structure of the matrices $\mathbf{J}_{\mathbf{y}}^n$ and $\mathbf{M}_{\mathbf{y}}^{n+1}$ together with the rectangular band structure of $\partial \mathbf{R}_{\mathbf{x},st}^n/\partial \mathbf{y}^n$ and $\partial \mathbf{R}_{\mathbf{y},st}^n/\partial \mathbf{x}^n$ simplifies the calculation of the terms $\mathbf{c}_1$ and $\mathbf{c}_2$, decomposing the full system of all microscale states into multiple subproblems. Instead of solving one linear problem of the size of all microscale problems, N_m linear solves are performed, each the size of a single microscale problem.

After solving for $\boldsymbol{\lambda}_{\mathbf{x}}^n$, we find $\boldsymbol{\lambda}_{\mathbf{y}}^n$ via (43). Again the decomposition of the microscale problem seen in (47) allows us to perform these calculations separately for each microscale problem:

$$\boldsymbol{\lambda}_{\mathbf{y}_i}^n = \left(\left(\mathbf{J}_{\mathbf{y}_i}^n\right)^T\right)^{-1} \left(\frac{\partial \mathcal{F}^n}{\partial \mathbf{y}_i^n} + \left(\frac{M_{\mathbf{y}_i}^{n+1}}{\Delta t}\right)^T \boldsymbol{\lambda}_{\mathbf{y}_i}^{n+1} - \left(\frac{\partial \mathbf{R}_{\mathbf{x}_i,st}^n}{\partial \mathbf{y}^n}\right)^T \boldsymbol{\lambda}_{\mathbf{x}}^n\right). \tag{48}$$

Using the adjoint states $\boldsymbol{\lambda}_{\mathbf{x}}^n$ and $\boldsymbol{\lambda}_{\mathbf{y}}^n$ at each time step, the derivatives of the objective with respect to s_i can be computed as follows:

$$\frac{\mathrm{d}Z}{\mathrm{d}s_i} = \frac{\partial Z}{\partial s_i} - \sum_{n=1}^{N_\mathrm{t}} \begin{bmatrix} \boldsymbol{\lambda}_{\mathbf{x}}^n \\ \boldsymbol{\lambda}_{\mathbf{y}}^n \end{bmatrix}^T \begin{bmatrix} \dfrac{\partial \mathbf{R}_{\mathbf{x}}^n}{\partial s_i} \\ \dfrac{\partial \mathbf{R}_{\mathbf{y}}^n}{\partial s_i} \end{bmatrix}. \tag{49}$$

The accuracy of the sensitivity analysis has been verified through comparisons with finite differencing results. To illustrate the savings in computational cost of the proposed adjoint sensitivity analysis versus numerical finite differencing, we compare the runtimes for the example presented in the following section, which involves 8564 degrees of freedom, 80 state-dependent constraints, and up to 120 design variables. One forward simulation of the battery discharge process with approximately 50 time steps and the evaluation of objective and constraints require a total of 10-min

DOI: 10.1002/nme

wall-clock time. Using either a forward or backward differencing method to compute a sensitivity takes approximately 10-min wall-clock time per design variable; calculating all 120 sensitivities via the differencing method requires 20-h wall-clock time. With the use of the multiscale sensitivity analysis approach presented here, all design sensitivities are found in approximately 5-min wall-clock time. This includes computing the adjoint solutions for the objective and the 80 constraints via (43) and performing the post-multiplications (49) for all design variables. The efficiency of the proposed adjoint approach versus finite differencing increases further as the number of design variables increases and the number of constraints decreases. Note that for this example, as well as the problems presented in Section 4, the model is sufficiently small such that storing the state variables during the forward analysis is not a concern and the run-time performance is the dominating factor in these simulations. For large numerical models, strategies for reducing the memory requirements of the adjoint sensitivity analysis might need to be considered [31–33].

4. NUMERICAL EXAMPLES

In this section, we demonstrate the potential of the proposed optimization framework for improving the performance of Li^+ battery electrodes. The purpose of the problems presented here is not to cover all aspects of improving battery performance but to highlight some capabilities and features of the proposed framework. A follow-up paper will study the application of our computational framework to optimize the layout of electrodes in greater detail.

Results presented here illustrate the use of both macroscale and microscale design criteria and variables to improve Li^+ battery performance. We seek to find optimal electrode designs to maximize the usable capacity of a battery cell while constraining the stresses during discharge by (1) manipulating the local cathode porosities and (2) using both local porosities and particle radii as design variables. The particle level stress is a microscale design criterion, whereas the capacity is macroscale. The design variables of the local porosities and particle radii were chosen because of their previously shown effect on the particle level stresses [7,34]. In addition, research in developing methods to fabricate functionally graded electrodes has advanced [35,36].

For all examples presented, the forward problem consists of a galvanostatic discharge of a cell at a constant current of 12.1 A/m^2 until the potential of the cathode material at the cathode–current collector interface reaches 3.2 V versus Li. To simplify the problem, we model a Li half-cell that includes a porous cathode and Li foil anode that is modeled though boundary conditions on the macroscale Li^+ concentration and potential fields [7]. The cathode has a thickness of $\delta_+ = 100\ \mu m$; the active material is Mn_2O_4, and the electrolyte is PEO-$LiCF_3SO_3$; the thickness of the separator is $\delta_s = 50\ \mu m$. The material parameters and initial conditions are given in Tables I and II.

The problem is discretized in time using an adaptive time-stepping algorithm with the time steps varying between $\Delta t = [0.1, \ldots, 600]$ s. The time steps decrease as the discharge rate increases. The separator is discretized by 20 elements, the cathode by 40 elements, and each microscale particle by 20 elements. Two-point Gauss integration is used at the macroscale, which results in $N_m = 80$ microscale problems. In total, there are 244 macroscale state variables and 8320 microscale state variables. Studies were performed to ensure mesh and time convergence.

Table I. PEO-$LiCF_3SO_3$ electrolyte material parameters.

Symbol	Value	Units	Description
$c_{l,max}$	3920	mol/m^3	Maximum Li^+ concentration in electrolyte
$c_{l,0}$	2070	mol/m^3	Initial Li^+ concentration in electrolyte
$\phi_{1,0}$	$U'(c_{s,0})$	V	Initial potential in solid phase
$\phi_{2,0}$	0	V	Initial potential in liquid phase
$\mathbf{u}$	0	m	Initial macroscopic displacements
κ_∞	6.5e−3	S/m	Conductivity in electrolyte
D_l	7.5e−12	m^2/s	Diffusivity of Li in electrolyte
E_l	0.69	MPa	Young's modulus
ν_l	0.4	–	Poisson's ratio

DOI: 10.1002/nme

Table II. Mn_2O_4 cathode material parameters.

Symbol	Value	Units	Description
$c_{s,max}$	22,900	mol/m^3	Maximum Li concentration in cathode
$c_{s,0}$	4351	mol/m^3	Initial Li concentration in cathode
$u_{r,0}$	0	m	Initial microscopic displacements in cathode
σ_s	3.8	S/m	Conductivity in cathode
D_s	7.08e−15	m^2/s	Diffusivity of Li in cathode
E_s	10	GPa	Young's modulus
ν_s	0.3	–	Poisson's ratio
Ω_{Li}	3.497e−6	m^3/mol	Partial molar volume
k_2	1e−10	m^4/mol/s	Butler–Volmer reaction rate constant
ϕ_{end}	3.2	V	Cutoff potential
τ_0	−0.606	J/m^3	Surface tension
K^s	10.65	N/m	Surface modulus

Table III. Globally convergent method of moving asymptotes parameters.

Parameter	Value
Step size	0.01–0.2
Initial adaptation of asymptotes	0.5
Adaptation of asymptotes	0.7
Maximum number of subcycles	1
Convergence criterion ϵ_s	10^{-8}

The design optimization problems are solved using the globally convergent method of moving asymptotes (GCMMA) of Svanberg [37]. The GCMMA constructs a sequence of convex separable subproblems that are solved by a primal–dual method and is guaranteed to converge to a Karush–Kuhn–Tucker optimal point. This algorithm is well suited for problems with large numbers of design variables and few constraints. The GCMMA is considered converged if the constraints are satisfied and the relative change in design variables, ϵ_s, is sufficiently small:

$$\frac{\| \mathbf{s}^{m-1} - \mathbf{s}^m \|}{\| \mathbf{s}^{m-1} \|} \leqslant \epsilon_s, \tag{50}$$

where m is the iteration number of the optimization process. Parameters used for the GCMMA algorithm are given in Table III; their influence on the convergence of the optimization algorithm is discussed in [37].

4.1. Maximum capacity optimization

Theoretically, lower porosities have higher capacities as there is a greater amount of active electrode material available for Li^+ to intercalate into. However, in practice, a decrease in the usable capacity of the battery is seen with low porosities as Li^+ transport through the electrode region is inhibited causing the battery to reach more rapidly its cutoff potential, that is, the lower operating bound of the battery potential. If the battery is discharged beyond the cutoff voltage, side reactions occur causing irreversible capacity loss and may lead to failure of the battery. The goal is to maximize the usable capacity of the battery, which is the discharge rate multiplied by the time until the battery potential reaches the cutoff potential of 3.2 V.

First, we illustrate the influence of porosity on the electrochemical and mechanical response of the battery cell of Figure 2 by considering an electrode with spatially uniform porosity and microscale particles of constant radius $R_s = 5\ \mu$m. As seen in Figure 3, uniformly varying the porosity strongly influences the discharge behavior of the battery: high porosities result in a lower capacity and a quick discharge to the cutoff potential. Low porosities allow for a greater overall volume of active material

DOI: 10.1002/nme

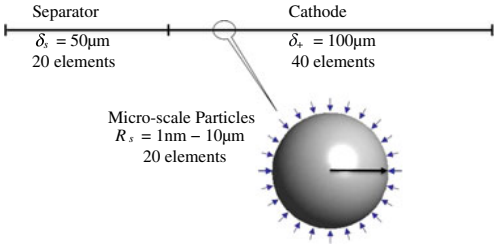

Figure 2. Model setup and discretization.

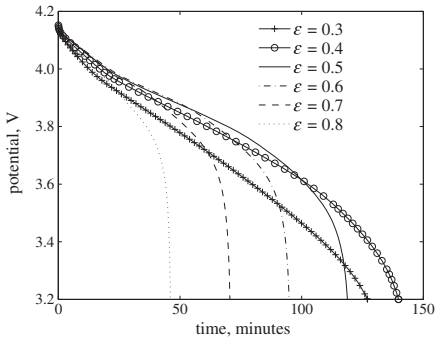

Figure 3. Battery potential as a function of time for uniform porosity distribution with $R_s = 5$ μm.

and yield a higher usable capacity down to $\varepsilon = 0.4$, beyond which the low porosity limits Li^+ transport in the electrolyte, causing the battery to discharge more quickly as seen in the line for $\varepsilon = 0.3$. Figure 4(a) shows the relationship between the usable capacity of the battery and a spatially uniform porosity. The capacity is highest with intermediate porosities. As seen in Figure 4(b), low (and high) porosities lead to higher stresses, which are generated by a high Li flux into the particles.

After having illustrated the general influence of porosity on the electrochemical and mechanical response of a battery cell, we now study the effects of spatially varying porosity distributions to maximize the usable capacity of the battery during a galvanostatic discharge at $I = 12.1$ A/m^2 while constraining the maximum tensile tangential stress, σ_T, observed in any particle over the discharge period.

$$\begin{gathered} \max_{\mathbf{s}} \quad I\hat{t} \\ \max_t \ \max_r \ \max_i \ \sigma_{T,t,r,i} - \sigma_{\max} \leqslant 0 \\ t = 1 : N_t, \ r = 0 : R_s, \ i = 1 : N_m, \end{gathered} \tag{51}$$

where $\hat{t}$ is the time at which the battery reaches the cutoff potential, r denotes the radial direction in the particle model, i the individual microscale particles, and t the time step. The constraint level for the stresses, $\sigma_{\max}$ is set to 50 MPa. This stress level was chosen on the basis of stress levels seen in the constant porosity solutions as shown in Figure 4(b). Considering only constant porosity solutions, the best solution satisfying the constraints is a constant porosity of $\varepsilon = 0.38$ with a usable capacity of 28.53 Ahr/m^2.

DOI: 10.1002/nme

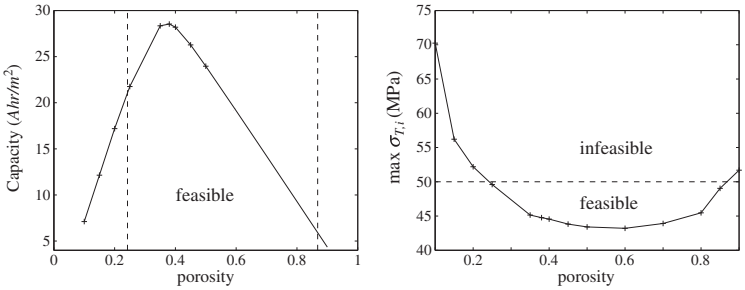

(a) Battery potential (b) Maximum tangential particle stress

Figure 4. Battery potential at the end of discharge and maximum stress values for constant porosities; horizontal and vertical lines separate feasible and infeasible domains. (a) Battery potential; (b) Maximum tangential particle stress.

The design problem (51) is solved using the following problem formulation:

$$\begin{aligned} &\min_{\mathbf{s}} \quad -I\hat{t} \\ &\tilde{\sigma}_{T,i} - \sigma_{\max} \leqslant 0 \\ &0.1 \leqslant s_i \leqslant 0.9 \quad i = 1 : N_{\mathrm{s}}, \end{aligned} \tag{52}$$

with

$$\tilde{\sigma}_{T,i} = \frac{1}{\beta} \ln \sum_{t} \sum_{r} \exp\left(\beta \sigma_{T,t,r,i}\right) \quad t = 1{:}N_{\mathrm{t}},\ r = 0{:}R_{\mathrm{s}}. \tag{53}$$

To reduce the number of stress constraints, we approximate the maximum particle stress, $\tilde{\sigma}_{T,i}$, by the Kreisselmeier–Steinhauser function with $\beta = 3$; this β-value gives an error in the approximation of less than 2%. Using 40 finite elements along the cathode with element-wise constant porosity results in $N_{\mathrm{s}} = 40$ design variables. The local porosities are varied between 0.1 and 0.9. The Kreisselmeier–Steinhauser approximation of the stress constraint is imposed at each macroscale integration point resulting in $N_{\mathrm{g}} = 80$ inequality constraints. Note that as the number of constraints is larger than the number design variables, the direct approach for computing the design sensitivities would be more efficient for this problem than the adjoint approach.

The initial design is chosen as $\varepsilon = 0.2$, which has a high theoretical capacity, but lower usable capacity due to Li^+ transport limitations, and stresses above the maximum allowable levels. The usable capacity of the optimized design is increased to 28.78 Ahr/m^2 from an initial value of 17.19 Ahr/m^2. This is a slight improvement over the constant porosity optimal solution of $\varepsilon = 0.38$. Figure 5(a) shows the porosity distributions for the initial and optimal configurations. Figure 5(b) shows the potential of the battery versus time for both configurations. The battery potential decrease with time occurs at a lower rate for the optimal configuration as compared with the initial.

The differences between initial and optimized designs are further illustrated by examining the particle stress and Li concentration distributions within the cathode particles over time. Figure 6 shows the evolution of the maximum tangential stress, and Figure 7 shows the evolution of the Li concentration normalized by $c_{\mathrm{s,max}}$ in the solid particles for both configurations as a function of time and position within the battery cell. In the initial configuration, there is a significant uptake of Li in the front of the cathode, which leads to high stresses above the stress constraint level. The optimal design spreads the uptake of Li further into the cathode. By increasing the porosity at the front of the cathode, where the highest stresses are located, the maximum stress is reduced, whereas the lower porosity at the back of the cathode helps to maintain a higher potential during discharge. The aforementioned results suggest that functional grading of the cathode results in a small but distinct improvement in the performance of the battery.

DOI: 10.1002/nme

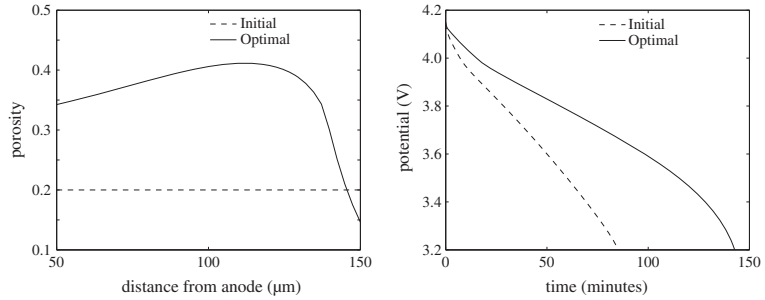

Figure 5. (a) Initial and optimal porosity distributions in cathode; (b) battery potential as a function of time for initial and optimal solutions.

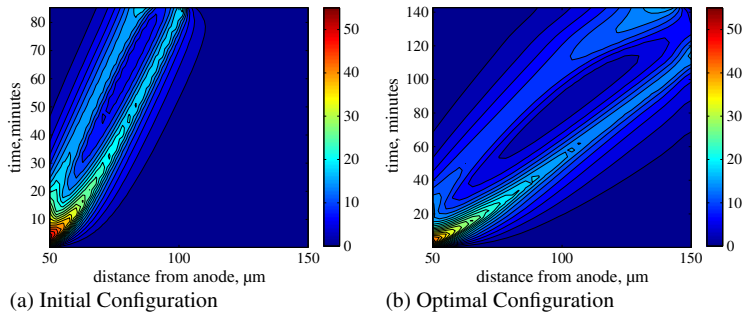

Figure 6. Maximum tangential particle stress as a function of position and time (MPa). (a) Initial configuration; (b) optimal configuration.

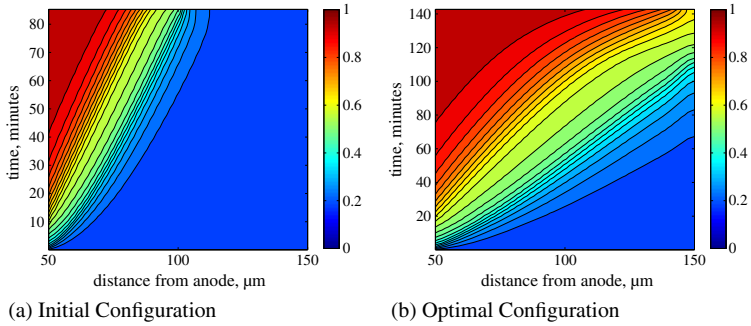

Figure 7. Normalized Li concentration ($c_s/c_{s,\max}$) in cathode particles as a function of position and time. (a) Initial configuration; (b) optimal configuration.

4.2. Maximum capacity optimization with variable porosity and particle radii

Both the electrochemical and mechanical performances of Li^+ batteries are affected by the size of the microscale particles. For uniform particle radius and porosity distributions across the electrode, Figure 8(a) illustrates the influence of different particle radii on the battery potential as a function of time. This plot suggests that in general, smaller particle radii improve the usable capacity. However, as seen in Figure 8(b), for particle radii smaller than approximately 20 nm and larger than 6 μm,

DOI: 10.1002/nme

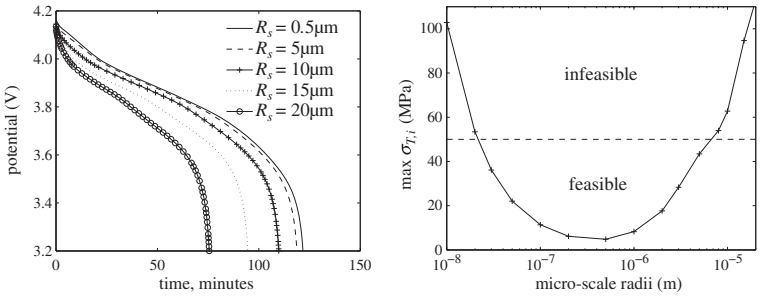

(a) (b)

Figure 8. (a) Battery potential as a function of time and (b) maximum stress for uniform particle radius distribution and $\varepsilon = 0.5$.

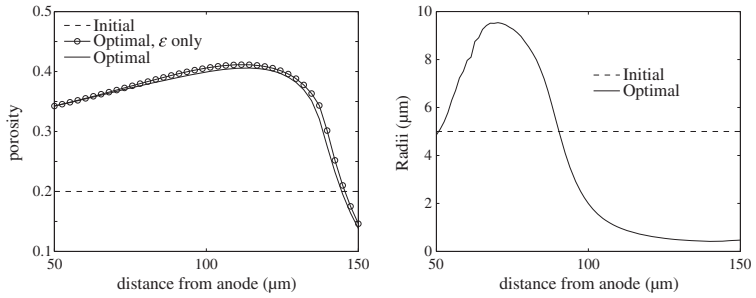

(a) Porosity (b) Particle Radii

Figure 9. Initial and optimal porosity and radii distributions. (a) Porosity; (b) Particle Radii.

the stress levels are above the constraint level. For larger particles, the intercalation of Li into the particle is diffusion limited, and the resulting concentration gradient causes mismatch strains and stresses owing to the stress–diffusion coupling, (13) and (14). This effect increases with increasing particle size. The high stresses in the smaller particles are due to the surface stress effect [29, 34].

In the following, we show that using the local particle radii in addition to the local porosities as design variables allows for an additional increase in the usable capacity while maintaining the stress constraint. We perform the same optimization problem as in Section 4.1, with the addition of the microscale particle radii as design variables. The design variables associated with the particle radii are scaled such that they are of similar magnitude as the porosity variables. Using the same discretization as before, this problem has a total of 120 design variables: 40 macroscale porosities and 80 microscale radii. The particle radii are limited to vary between 1 nm and 10 μm. Again, the upper limit of the tangential particle stress is enforced via 80 constraints. Note that for this problem, the adjoint approach is more efficient than a direct sensitivity analysis as the number of design variables is larger than the number of constraints.

The optimization problem is initialized with particles of radius 5 μm and a constant porosity of 0.2, and the stress constraint level is 50 MPa. Figure 9 shows the initial and optimal porosity and particle radii distributions. Figure 10 plots the battery potential as a function of time for the initial and optimal configurations. The initial configuration has a usable capacity of 17.19 Ahr/m^2, whereas the optimal configuration increases the usable capacity to 29.27 Ahr/m^2, which is an improvement over the optimal usable capacity of 28.78 Ahr/m^2 using only porosities as design variables.

The optimal design has a similar porosity profile as the porosity only optimization problem, and the additional improvement in performance is due to the change in the radii profiles. Larger particle sizes are diffusion limited, maintaining high surface Li concentrations, thus decreasing the rate of Li

DOI: 10.1002/nme

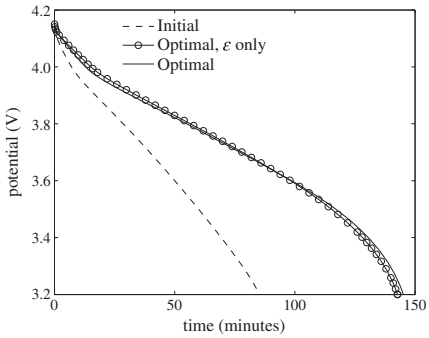

Figure 10. Battery potential as a function of time for initial and optimal configurations.

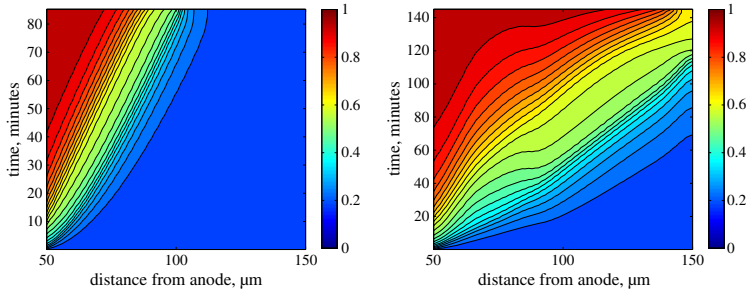

(a) Initial Configuration (b) Optimal Configuration

Figure 11. Normalized Li concentration ($c_s/c_{s,max}$) in particles as a function of position and time. (a) Initial configuration; (b) optimal configuration.

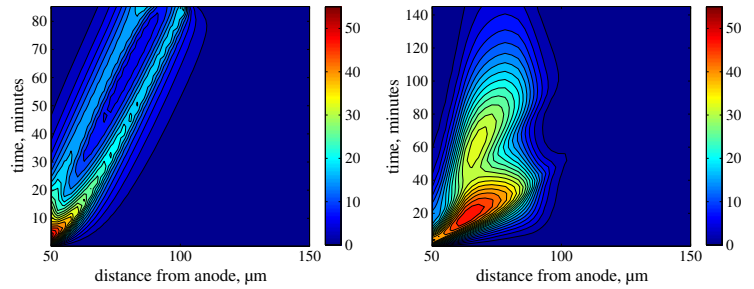

(a) Initial Configuration (b) Optimal Configuration

Figure 12. Maximum tensile tangential particle stress as a function of position and time (MPa). (a) Initial configuration; (b) optimal configuration.

insertion, and allowing for greater Li^+ transport in the electrolyte. This dominates in the front half of the cathode. Towards the rear of the cathode, smaller particle sizes dominate as the small particle sizes allow for faster Li insertion into these particles. As seen in Figure 11, the initial design utilizes only a small part of the cathode, with Li uptake occurring at the front of the electrode. The optimal design pushes the Li uptake further into the cathode with most of the particles reaching saturation levels by the end of the discharge. For the initial configuration, the highest stresses are located at the front of the cathode, whereas for the optimal configuration, the highest stress levels occur further

DOI: 10.1002/nme

into the cathode where the largest particle sizes occur as seen in Figure 12. Overall, the addition of particle radii as design variables improves both the electrochemical and mechanical performance of the battery.

5. CONCLUSIONS

In this paper, we developed a computational framework for optimizing Li^+ battery cells using a multiscale finite element model. The efficiency of this framework relies on an adjoint sensitivity analysis. The computational burden of solving the adjoint sensitivity equations is reduced by decomposing the full problem into multiple independent microscale problems. Adjoint sensitivity analysis was shown to significantly reduce the computational cost versus finite differencing; the computational savings increase with increasing number of design variables. The potential of this framework was illustrated with numerical examples optimizing the electrode layout to improve the usable capacity of the battery. The performance of the battery cell was improved considering macroscale and microscale design criteria and variables. The optimization results suggest that both the electrochemical and mechanical performances of battery cells can be improved by functionally grading electrodes.

The current battery model does not account for several phenomena that may impact the optimal electrode layout. This includes finite strain effects due to large deformations of the microscale particles [38] and the formation of a solid electrolyte interphase layer on the particle surface [39, 40]. Whereas the inclusion of these phenomena may alter the optimization results presented in this paper, our proposed computational framework allows for integrating the associated models. Beyond Li^+ battery cells, our computational framework can be applied to other multiscale problems involving coupled electrochemical and mechanical phenomena, such as super-capacitors, solar cells, and fuel cells.

APPENDIX A

Table A.I. List of symbols.

Symbol	Units	Description
$\mathbf{C}_{\text{eff}}$	Pa	Homogenized elasticity tensor
$\mathbf{C}_{\text{s}}, \mathbf{C}_{\text{l}}$	Pa	Isotropic elastic stiffness matrix for solid and liquid phases
c_{l}	mol/m^3	Concentration of Li in electrolyte
$c_{\text{l,max}}$	mol/m^3	Max concentration of Li in electrolyte
c_{s}	mol/m^3	concentration of Li in solid particles, microscale state variable
$c_{\text{s,max}}$	mol/m^3	Max concentration of Li in solid particles
D_{eff}	m^2/s	Macroscale effective diffusion coefficient of Li in electrolyte
D_{l}	m^2/s	Diffusion coefficient of Li^+ in bulk electrolyte
D_{s}	m^2/s	Diffusion coefficient of Li in solid
E_{s}	Pa	Solid particles Young's modulus
E_{l}	Pa	Electrolyte Young's modulus
$\mathbf{e}$		Macroscopic strains due to macroscopic displacements
$\mathbf{e}_{\text{ch}}$		Macroscale chemically induced eigenstrain
$\mathbf{e}_{\text{V}}$		Volumetric strain of microscale solid particle
F	C/mol	Faraday constant
G_j		Optimization constraint
$\mathbf{I}$	A/m^2	Applied macroscale current density
i_0	A m/mol	Exchange current density
$\mathbf{i}_1$	A/m^2	Current density in solid phase
$\mathbf{i}_2$	A/m^2	Current density in electrolyte phase
$\mathbf{J}$	mol/m^2/s	Li flux in solid particles
j_{eff}	mol/m^3/s	Macroscale effective pore wall flux
j_{s}	mol/m^2/s	Microscale pore wall flux
k_2	m^4/mol/s	Reaction rate constant at cathode/polymer interface

DOI: 10.1002/nme

Table A.I. *Continued.*

K^s	N/m	Microscale surface modulus
$\mathbf{N}$	mol/m^2/s	Li^+ flux in the electrolyte
N_g		Number of optimization constraints
N_m		Number of microscale problems
N_s		Number of optimization design variables
N_t		Number of time steps
P_h	Pa	Microscale surface pressure from Mori–Tanaka theory
P_{micro}	Pa	Microscale surface pressure exerted on a particle
P_{SS}	Pa	Microscale surface pressure due to surface stress effects
p_{lm}	Pa	Macroscale applied pressure
R	J/mol/K	Universal gas constant
R_s	m	Radius of cathode particles
r	m	Microscale distance from center of cathode particle
$\mathbf{S}$		Eshelby's tensor
$\mathbf{s}$		Vector of design variables
s_i^L		Lower bound for optimization variable
s_i^U		Upper bound for optimization variable
T	K	Temperature
t	s	Time
t_0^+		Li^+ transference number
U'	V	Open circuit potential
$\mathbf{u}$	m	Macroscopic displacements
u_r	m	Microscopic displacements
V	m^3	Total volume
V_l	m^3	Volume of liquid phase
x	m	Distance from anode
$\tilde{\mathbf{x}}$		Vector of all macroscale state variables at all time steps
$\tilde{\mathbf{y}}$		Vector of all microscale state variables at all time steps
Z		Optimization objective
α_A, α_C		Anodic and cathodic transfer coefficients
δ_s	m	Thickness of separator
δ_+	m	Thickness of cathode region
ε		Porosity, liquid volume fraction
ε_t		Microscopic tangential strain
ϕ_1	V	Potential in solid phase
ϕ_2	V	Potential in liquid phase
η	V	Surface over-potential
κ_{eff}	S/m	Effective conductivity of electrolyte
κ_∞	S/m	Conductivity of bulk electrolyte
λ	S/m	Conductivity of solid matrix
Ω_{Li}	m^3/mol	Partial molar volume
$\boldsymbol{\sigma}$	Pa	Macroscopic stress
σ_R	Pa	Microscopic radial stress
σ_T	Pa	Microscopic tangential stress
σ_h	Pa	Hydrostatic stress
τ_0	J/m^2	Microscale deformation-independent surface tension
Γ_{x_A}		Boundary at anode–separator interface
Γ_{x_C}		Boundary at cathode–current collector interface
$\boldsymbol{\lambda}_{\tilde{\mathbf{x}}}$		Macroscale adjoint states at all time steps
$\boldsymbol{\lambda}_{\tilde{\mathbf{y}}}$		Microscale adjoint states at all time steps

ACKNOWLEDGEMENTS

The authors gratefully acknowledge the support of the Air Force Office of Scientific Research MURI (Grant No. F9550-06-1-0326) monitored by Dr. B. L. Lee and the National Science Foundation under Grant No. 0729520; the first author acknowledges the support of a Graduate Research Fellowship from the National Science Foundation.

DOI: 10.1002/nme

REFERENCES

1. Winter M, Brodd RJ. What are batteries, fuel cells, and supercapacitors? *Chemical Reviews* 2004; **104**(10): 4245–4269.
2. Zhang X, Shyy W, Sastry AM. Numerical simulation of intercalation-induced stress in Li-ion battery electrode particles. *Journal of the Electrochemical Society* 2007; **154**(10):910–916. DOI: 10.1149/1.2759840.
3. Baggetto L, Niessen RAH, Roozeboom F, Notten P H L. High energy density all-solid-state batteries: a challenging concept towards 3D integration. *Advanced Functional Materials* 2008; **18**:1057–1066. DOI: 10.1002/adfm.200701245.
4. Chan CK, Peng H, Liu G, McIlwrath K, Zhang XF, Huggins RA, Cui Y. High-performance lithium battery anodes using silicon nanowires. *Nature Nanotechnology* 2008; **3**:31–35. DOI: 10.1038/nnano.2007.411.
5. Wang D, Wu X, Wang Z, Chen L. Cracking causing cyclic instability of LiFePO4 cathode material. *Journal of Power Sources* 2005; **140**(1):125–128.
6. Wang H, Jang YI, Huang B, Sadoway DR, Chiang YM. Tem study of electrochemical cycling-induced damage and disorder in LiCoO[sub 2] cathodes for rechargeable lithium batteries. *Journal of The Electrochemical Society* 1999; **146**(2):473–480. DOI: 10.1149/1.1391631.
7. Golmon S, Maute K, Dunn ML. Numerical modeling of electrochemical–mechanical interactions in lithium polymer batteries. *Computers & Structures* 2009; **87**(23-24):1567–1579. DOI: 10.1016/j.compstruc.2009.08.005.
8. Chen Y, Evans JW. Thermal analysis of lithium polymer electrolyte batteries by a two dimensional model – thermal behaviour and design optimization. *Electrochimica Acta* 1994; **39**(4):517–526. DOI: 10.1016/0013-4686(94)80095-2.
9. Yu LJ, Qin MJ, Zhu P, Yang L. Numerical simulation and optimization of nickel–hydrogen batteries. *Journal of Power Sources* 2008; **179**(2):848–853. DOI: 10.1016/j.jpowsour.2007.12.126.
10. Kim MJ, Peng H. Power management and design optimization of fuel cell/battery hybrid vehicles. *Journal of Power Sources* 2007; **165**(2):819–832. DOI: 10.1016/j.jpowsour.2006.12.038.
11. Chen YH, Wang CW, Zhang X, Sastry AM. Porous cathode optimization for lithium cells: Ionic and electronic conductivity, capacity, and selection of materials. *Journal of Power Sources* 2010; **195**:2851–2862. DOI: 10.1016/j.jpowsour.2009.11.044.
12. Ramadesigan V, Methekar RN, Latinwo F, Braatz RD, Subramanian VR. Optimal porosity distribution for minimized ohmic drop across a porous electrode. *Journal of The Electrochemical Society* 2010; **157**(12):A1328–A1334. DOI: 10.1149/1.3495992.
13. Du W, Gupta A, Zhang X, Sastry AM. Effect of cycling rate, particle size and transport properties on lithium-ion cathode performance. *International Journal of Heat and Mass Transfer* 2010; **53**:3552–3561. DOI: 10.1016/jijheatmasstransfer.2010.04.017.
14. Doyle M, Fuller TF, Newman J. Modeling of galvanostatic charge and discharge of the lithium/polymer/insertion cell. *Journal of the Electrochemical Society* 1993; **140**(6):1526–33.
15. Fuller TF, Doyle M, Newman J. Simulation and optimization of the dual lithium ion insertion cell. *Journal of the Electrochemical Society* 1994; **141**(1):1–10.
16. Fuller TF, Doyle M, Newman J. Relaxation phenomena in lithium-ion-insertion cells. *Journal of the Electrochemical Society* 1994; **141**(4):982–990. DOI: 10.1149/1.2054868.
17. Doyle M, Newman J. The use of mathematical modeling in the design of lithium/polymer battery systems. *Electrochimica Acta* 1995; **40**:2191–2196. DOI: 10.1016/0013-4686(95)00162-8.
18. Doyle M. Design and simulation of lithium rechargeable batteries. *Ph.D. Thesis*, University of California, Berkeley, 1995.
19. Newman J, Thomas KE. *Electrochemical Systems*, 3rd ed. Hoboken: Wiley-Interscience, 2004.
20. Kanouté P, Boso D, Chaboche J, Schrefler B. Multiscale methods for composites: a review. *Archives of Computational Methods in Engineering* 2009; **16**:31–75. DOI: 10.1007/s11831-008-9028-8.
21. Miehe C, Schröder J, Schotte J. Computational homogenization analysis in finite plasticity simulation of texture development in polycrystalline materials. *Computer Methods in Applied Mechanics and Engineering* 1999; **171**(3-4):387–418.
22. Miehe C, Schotte J, Lambrecht M. Homogenization of inelastic solid materials at finite strains based on incremental minimization principles. Application to the texture analysis of polycrystals. *Journal of the Mechanics and Physics of Solids* 2002; **50**(10):2123–2167.
23. Feyel F. Multiscale Fe2 elastoviscoplastic analysis of composite structures. *Computational Materials Science* 1999; **16**(1-4):344–354.
24. Feyel F, Chaboche JL. Fe2 multiscale approach for modelling the elastoviscoplastic behaviour of long fibre SiC/Ti composite materials. *Computer Methods in Applied Mechanics and Engineering* 2000; **183**(3-4):309–330.
25. Feyel F. A multilevel finite element method (Fe2) to describe the response of highly non-linear structures using generalized continua. *Computer Methods in Applied Mechanics and Engineering* 2003; **192**(28-30):3233–3244.
26. Mori T, Tanaka K. Average stress in matrix and average elastic energy of materials with misfitting inclusions. *Acta Metallurgica* 1973; **21**:571–574.
27. Benveniste Y. A new approach to the application of Mori–Tanakas theory in composite materials. *Mechanics of Materials* 1987; **6**:147–157.
28. Benveniste Y, Dvorak G. *On a Correspondence Between Mechanical and Thermal Effects in Two-Phase Composites. In Micromechancis and Inhomogeneity*. Springer: New York, 1990.

29. DeLuca CM, Maute K, Dunn ML. Effects of electrode particle morphology on stress generation in silicon during lithium insertion. *Journal of Power Sources* 2011; **196**(22):9672–9681. DOI: 10.1016/j.jpowsour.2011.07.035.
30. Cheng YT, Verbrugge MW. The influence of surface mechanics on diffusion induced stresses within spherical nanoparticles. *Journal of Applied Physics* 2008; **104**(8):083–521. DOI: 10.1063/1.3000442.
31. Hinze M, Walther A, Sternberg J. An optimal memory-reduced procedure for calculating adjoints of the instationary navier-stokes equations. *Optimal Control Applications & Methods* 2006; **27**(1):19–40. DOI: 10.1002/oca.771.
32. Rumpfkeil M, Zingg D. The optimal control of unsteady flows with a discrete adjoint method. *Optimization and Engineering* 2010; **11**(1):5–22. DOI: 10.1007/s11081-008-9035-5.
33. Rumpfkeil M, Zingg D. Unsteady optimization using a discrete adjoint approach applied to aeroacoustic shape design. *AIAA 2008-0018, Grand Sierra Resort Hotel 46th AIAA Aerospace Sciences Meeting and Exhibit: Reno, NV*, 2008.
34. Golmon S, Maute K, Lee SH, Dunn ML. Stress generation in silicon particles during lithium insertion. *Applied Physics Letters* 2010; **97**(3). DOI: 10.1063/1.3458707.
35. Chiang YM, Hellweg B. Reticulated and controlled porosity battery structures, 06 2009. (Available from: http://patents.justia.com/2009/07553584.html) accessed on 1/4/12.
36. Mirzaeian M, Hall P. Preparation of controlled porosity carbon aerogels for energy storage in rechargeable lithium oxygen batteries. *Electrochimica Acta* 2009; **54**:7444–7451. DOI: 10.1016/j.electacta.2009.07.079.
37. Svanberg K. A class of globally convergent optimization methods based on conservative convex separable approximations. *SIAM J. on Optimization* 2002; **12**(2):555–573. DOI: 10.1137/s1052623499362822.
38. Bower A, Guduru P, Sethuraman V. A finite strain model of stress, diffusion, plastic flow, and electrochemical reactions in a lithium-ion half-cell. *Journal of the Mechanics and Physics of Solids* 2011; **59**:804–828. DOI: 10.1016/j.jmps.2011.01.003.
39. Christensen J, Newman J. A mathematical model for the lithium-ion negative electrode solid electrolyte interphase. *Journal of The Electrochemical Society* 2004; **151**(11):A1977–A1988. DOI: 10.1149/1.1804812.
40. Yan J, Xia BJ, Su YC, Zhou XZ, Zhang J, Zhang XG. Phenomenologically modeling the formation and evolution of the solid electrolyte interface on the graphite electrode for lithium-ion batteries. *Electrochimica Acta* 2008; **53**(24):7069–7078. DOI: 10.1016/j.electacta.2008.05.032.

Appendix D

Publication: A Design Optimization Methodology for Li^+ Batteries

Journal of Power Sources 253 (2014) 239–250

Contents lists available at ScienceDirect

Journal of Power Sources

journal homepage: www.elsevier.com/locate/jpowsour

A design optimization methodology for Li^+ batteries

Stephanie Golmon [a,b], Kurt Maute [a,b,*], Martin L. Dunn [a,c]

[a] Department of Aerospace Engineering Sciences, University of Colorado, Boulder, CO 80309, USA
[b] Department of Aerospace Engineering Sciences, University of Colorado, Boulder, CO 80309, USA
[c] Department of Mechanical Engineering, University of Colorado, Boulder, CO 80309, USA

HIGHLIGHTS

- A formal design optimization methodology for functionally graded electrodes of Li^+ batteries is developed.
- A multi-scale finite element model for predicting the power-storage characteristics of a full battery cell is presented.
- A multi-objective formulation is introduced to optimize the useable capacity over a range of discharge currents.
- The influence of spatially varying porosity and sizes of active particles on optimized electrodes is analyzed.
- The difference between considering a half-cell versus a full cell in the optimization process is shown.

ARTICLE INFO

Article history:
Received 13 August 2013
Received in revised form
18 November 2013
Accepted 6 December 2013
Available online 16 December 2013

Keywords:
Design optimization
Electrodes
Multi-scale modeling
Porosity
Particle size
Capacity

ABSTRACT

Design optimization for functionally graded battery electrodes is shown to improve the usable energy capacity of Li batteries predicted by computational simulations and numerically optimizing the electrode porosities and particle radii. A multi-scale battery model which accounts for nonlinear transient transport processes, electrochemical reactions, and mechanical deformations is used to predict the usable energy storage capacity of the battery over a range of discharge rates. A multi-objective formulation of the design problem is introduced to maximize the usable capacity over a range of discharge rates while limiting the mechanical stresses. The optimization problem is solved via a gradient based optimization. A $LiMn_2O_4$ cathode is simulated with a PEO–$LiCF_3SO_3$ electrolyte and both a Li Foil (half cell) and LiC_6 anode. Studies were performed on both half and full cell configurations resulting in distinctly different optimal electrode designs. The numerical results show that the highest rate discharge drives the simulations and the optimal designs are dominated by Li^+ transport rates. The results also suggest that spatially varying electrode porosities and active particle sizes provides an efficient approach to improve the power-to-energy density of Li^+ batteries. For the half cell configuration, the optimal design improves the discharge capacity by 29% while for the full cell the discharge capacity was improved 61% relative to an initial design with a uniform electrode structure. Most of the improvement in capacity was due to the spatially varying porosity, with up to 5% of the gains attributed to the particle radii design variables.

1. Introduction

Further advances in the energy density, rate capability, and cycling efficiency of batteries are needed in order to meet growing energy storage demands. The essential characteristics of a battery are typically represented via (1) Ragone plots showing the tradeoff between energy storage capacity and power (or rate) capability of the battery and (2) cycling efficiency values which measure the loss in energy storage capacity as a function of cycle number. In this paper, we focus on the trade-off between power and energy densities with consideration of mechanical stress levels that could lead to degradation over time. We do not explicitly model degradation phenomena such as loss of lithium due to side reactions and SEI layer formation and mechanical fracture [1]; instead we consider approximately mechanical degradation by introducing a stress limit in the electrode particles.

In general the energy storage capacity, or usable capacity decreases, with increasing rate or power demand as seen in Fig. 1. Here, we define the usable capacity as the amount of energy that can be extracted from the battery during discharge. In this study, we will show that the decrease in usable capacity at higher discharge rates can be mitigated by optimally designing the internal electrode structure based on the range of rates required from

* Corresponding author. Department of Aerospace Engineering Sciences, University of Colorado, Boulder, CO 80309, USA.
E-mail address: maute@colorado.edu (K. Maute).

0378-7753/$ – see front matter © 2013 Elsevier B.V. All rights reserved.
http://dx.doi.org/10.1016/j.jpowsour.2013.12.025

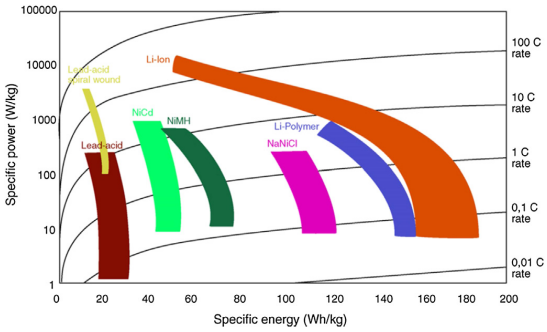

Fig. 1. Ragone plot comparing battery technologies [34].

the battery for a given application. We focus the study on lithium batteries which are among the most promising battery chemistries due to their high energy densities and operating voltages. Design variables for the battery electrode include the local porosity and particle radii distributions in the electrodes. Additional design variables such as the electrode thickness and material properties can be incorporated into this approach. We formulate this design problem via a multi-objective formulation, maximizing the usable capacity at various discharge rates while constraining the stress levels in the electrode particle to be below a specified maximum value. The optimization problem is solved via a gradient-based algorithm which allows for a large number of both design constraints and optimization variables. The battery simulation uses a transient, non-linear, multi-scale framework to simulate the discharge of the battery at prescribed rates. The sensitivities of the objective and constraints to the design variables are calculated via a multi-scale adjoint approach which is more accurate and efficient than computation of the sensitivities via finite differencing [2]. Adjoint sensitivity analysis combined with a gradient-based optimization algorithm drives the problem to the optimal electrode structure.

This paper is aimed at advancing the state-of-the-art in model-based optimization for Li batteries. Previous optimization studies for Li battery performance have focused on pack-level thermal [3–5] and power management [6] strategies. Design studies focusing on the cell level have been severely limited in number of design variables due to the complexity and computational cost of most battery models [7–10]. This brief literature review does not include design studies based on experimental investigations and parameter sweeps. Here, we are not limited in number of design variables due to our use of multi-scale adjoint sensitivity analysis developed by Golmon et al. [2]. Our approach is flexible, allowing for different types of objectives, constraints, and types of design variables without compromising the accuracy of the overall model. Possible optimization variables include but are not limited to: the electrode porosity and particle size, discharge rate(s), electrode thickness, and material properties. In this study, we focus on improving the discharge performance of the battery through functionally graded electrodes by optimizing the porosity and radii distribution in both electrodes over a range of discharge rates. We consider the effects of Li^+ transport in the electrolyte, Li transport in the electrode particles, local electrode surface kinetics, diffusion-induced stresses in the electrode particles and resulting aggregate swelling of the electrode. Solid electrolyte interphase (SEI) layer growth, chemical side reactions, thermal effects, and degradation effects from cycling and aging are not included. The optimization approach used here could be extended to more sophisticated models such as that of Kim et al. [11].

2. Multi-scale battery model

A typical Li battery is shown in Fig. 2 and consists of current collectors, porous electrodes and a separator region. The porous electrode includes active insertion compounds, conductive additives, and binders with electrolyte filling the pores. The liquid volume fraction of electrolyte is referred to as the porosity, ε, and in a typical battery is 30% [12]. When the battery is discharged, Li in the anode oxidizes. Electrons flow through the external circuit to the cathode and lithium ions, Li^+ are carried through the electrolyte via diffusion and migration to the cathode, where they are reduced. In modern Li batteries, Li inserts into a host electrode material rather than plating onto metals, and these compounds shrink and swell as a result of the Li insertion and de-insertion. The resulting stresses can exceed the fracture toughness of the active particle and experimental studies have linked mechanical effects with capacity fade [13] and localized degradation of the electrode [14]. Stress-induced surface cracks in electrode particles have been shown to nucleate new SEI layer growth and substantially contribute to the loss of Li, causing capacity fade [1]. These studies demonstrate that it is necessary to consider mechanical effects when optimizing the electrode structure in order to limit mechanical degradation. In this study, we define performance in terms of the trade-off between usable energy and power density during discharge of the battery. To minimize mechanical degradation over the life cycle of the battery, we limit electrode stress levels during discharge.

Here, we use a coupled electrochemical–mechanical multi-scale model to simulate the discharge of Li batteries [15]. This model is an extension of Doyle and Newman's electrochemical battery model [16–20] which describes the transport processes within the electrodes using porous electrode theory [21,20] rather than modeling the detailed geometry of the composite electrode. We have extended this model to include deformations due to external mechanical loads and swelling of electrode particles upon lithiation. This model explicitly considers two length scales: at the macro-scale, transport processes in the electrolyte, electric potentials in both the electrolyte and electrode, and mechanical deformations across the battery cell are described; at the micro-scale, the response of a single electrode particle is modeled; a meso-scale model is used to relate these two scales using volume averaging homogenization methods. The effective macro-scale properties are computed as a function of the micro-scale state variables at each time-step in the transient simulation. Qualitative comparisons of discharge curves generated by the electrochemical portion of this model with experimental studies have shown good agreement [22].

In the following sub-sections, we summarize the governing equations used to describe the battery behavior at the macro-scale, micro-scale and the homogenization approaches used to connect the two scales at the meso-scale.

2.1. Governing equations at macro-scale

At the macro-scale, the Li^+ concentration in the electrolyte, c_l, electric potentials in the solid, ϕ_1, and liquid, ϕ_2, phases, and displacements, **u**, are modeled.

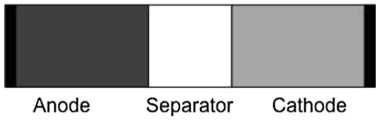

Fig. 2. Battery cell.

Lithium ions are transported through the electrolyte via diffusion and migration:

$$\varepsilon\frac{\partial c_l}{\partial t}+\nabla\cdot\mathbf{N}+\frac{1}{F}\frac{\partial t_+^0}{\partial c_l}\mathbf{i}_2\cdot\nabla c_l-\left(1-t_+^0\right)j_{\text{eff}}=0, \tag{1}$$

where $\mathbf{N}$ is the diffusive flux, t_+^0 is the Li^+ transference number, F is the Faraday constant, and j_{eff} is a source term which accounts for the volume average flux of Li^+ from the electrolyte into the electrode particles.

Within the solid (electrode), the electric potential is governed by Ohm's law:

$$\nabla\cdot\mathbf{i}_1+Fj_{\text{eff}}=0. \tag{2}$$

Similarly, the electric potential in the electrolyte is governed by a modified Ohm's law that accounts for the dependence of the current in the electrolyte, $\mathbf{i}_2$, on the concentration of Li^+ in the electrolyte, c_l.

$$\nabla\cdot\mathbf{i}_2-Fj_{\text{eff}}=0. \tag{3}$$

The macro-scale mechanical response is assumed to be linear-elastic with a volume-averaged eigenstrain model to account for swelling of the micro-scale electrode particles:

$$\nabla\cdot\boldsymbol{\sigma}+\mathbf{b}=0, \tag{4}$$

where $\boldsymbol{\sigma}$ and $\mathbf{b}$ are the macro-scale stress tensor and body force. Here, the body force is assumed to be zero.

The diffusive flux, electric currents, stress and strains are described by the following constitutive equations:

$$\mathbf{N}=-D_{\text{eff}}\nabla c_l, \tag{5}$$

$$\mathbf{i}_1=-\lambda\nabla\phi_1, \tag{6}$$

$$\mathbf{i}_2=-\kappa_{\text{eff}}\left[\nabla\phi_2-\frac{RT}{F}\left(1-t_+^0\right)\nabla\ln(c_l)\right], \tag{7}$$

$$\boldsymbol{\sigma}=\mathbf{C}:(\mathbf{e}-\mathbf{e}_{\text{ch}}),\mathbf{e}=\frac{1}{2}\left(\nabla\mathbf{u}+\nabla\mathbf{u}^T\right), \tag{8}$$

where D_{eff} is the effective diffusion coefficient of Li^+ in the electrolyte, λ is the conductivity of the electrode particles, κ_{eff} is the effective ionic conductivity of the electrolyte, $\mathbf{C}_{\text{eff}}$ is the homogenized elasticity tensor, and $\mathbf{e}_{\text{ch}}$ is the volume-averaged chemically induced eigenstrain due to the aggregate swelling of the electrode particles. More complex mechanical models to capture nonlinear stress–strain relationships, finite strains, and irreversible deformations could be included in this framework.

For a galvanostatic discharge of the battery, boundary conditions are applied as follows: at the anode-current collector boundary, Γ_{AC}, and cathode-current collector boundary, Γ_{CC}, all the current is carried by the electrode particles. The boundary conditions are given in columns two and three of Table 1.

To simplify the computational burden of these simulations, we also model a Li half cell, in which a porous cathode is discharged against a Li foil anode; the anode is modeled through boundary conditions at the anode-separator interface. At the anode-separator boundary, Γ_{AS}, Li^+ enters the electrolyte based on the rate of discharge, I, and all current is carried by the electrolyte. At the cathode-current collector the conditions remain the same. These boundary conditions are shown in columns three and four of Table 1.

Table 1
Boundary conditions for macro-scale battery model.

	Anode-current collector boundary, Γ_{AC}	Cathode-current collector boundary, Γ_{CC}	Anode-separator boundary, Γ_{AS}
Li^+ flux	$\nabla c_l=0$	$\nabla c_l=0$	$\mathbf{N}=\frac{I(1-t_+^0)}{F}$
Current in solid particles	$\mathbf{i}_1=I$	$\mathbf{i}_1=I$	$\mathbf{i}_1=0$
Current in electrolyte	$\mathbf{i}_2=0$	$\mathbf{i}_2=0$	$\mathbf{i}_2=I$
Displacements	$\mathbf{u}=0$	$\mathbf{u}=0$	$\mathbf{u}=0$

2.2. Governing equations at micro-scale

At the micro-scale, the response of a single electrode particle embedded in the host electrolyte is modeled. We assume that the macro-scale Li^+ concentration, electric potentials, and displacement fields are spatially constant in the electrolyte immediately surrounding the particle. Assuming the micro-scale particles are spherical results in uniform boundary conditions and allows for simplification of the micro-scale model to one dimension using spherical coordinates. The micro-scale model is based on the coupled diffusion-stress model developed by Zhang et al. [23], and extended to include Butler–Volmer surface kinetics and surface pressures.

The concentration, c_s, and deformation, u_r, fields within the particle are described by diffusion and linear static mechanical models:

$$\frac{\partial c_s}{\partial t}+\left(\frac{\partial}{\partial r}+\frac{2}{r}\right)\mathbf{J}=0, \tag{9}$$

$$\frac{d\sigma_R}{dr}+\frac{2}{r}(\sigma_R-\sigma_T)=0, \tag{10}$$

with the following constitutive equations:

$$\mathbf{J}=-D_s\left(\nabla_r c_s-\frac{\Omega c_s}{RT}\nabla_r\sigma_h\right), \tag{11}$$

$$\sigma_R=\frac{E}{(1+\nu)(1-2\nu)}\left((1-\nu)\nabla u_r+2\nu\frac{u}{r}-\frac{\Omega}{3}c_s(1+\nu)\right), \tag{12}$$

$$\sigma_T=\frac{E}{(1+\nu)(1-2\nu)}\left(\frac{u}{r}+\nu\nabla u_r-\frac{\Omega}{3}c_s(1+\nu)\right), \tag{13}$$

where D_s is the diffusion coefficient of Li in the particle; R is the universal gas constant; T is the temperature; σ_R, σ_T, and σ_h are the radial, tangential, and hydrostatic stresses; E and ν are the Young's modulus and Poisson's ratio of the electrode material. The Li partial molar volume, Ω, accounts for the swelling of the particle upon lithiation and the stress–diffusion coupling increases with Ω. The hydrostatic stress is defined as:

$$\sigma_h=(\sigma_R+2\sigma_T)/3. \tag{14}$$

At the particle center, $r=0$, the displacements and Li flux are zero, $u_r=0$, $\mathbf{J}=0$. At the particle surface, $r=R_s$, Li enters the particle and mechanical surface pressure is applied.

$$\mathbf{J}=j_s \text{ at } r=R_s, \tag{15}$$

$$\sigma_R=P_{\text{micro}} \text{ at } r=R_s. \tag{16}$$

The Li pore wall flux at the particle surface, j_s, is described by the Butler–Volmer surface kinetics model which predicts the current/Li flux across the boundary as a function of the electric potentials and concentrations in both phases:

$$j_s = \frac{i_0}{F}\left[c_{s|r=R_s}e^{k_1} - \left(c_{s,\max} - c_{s|r=R_s}\right)e^{k_2}\right], \tag{17}$$

$$\begin{aligned} i_0 &= FK_2\left(c_{l,\max} - c_l\right)^{\alpha_C}(c_l)^{\alpha_A},\\ k_1 &= \frac{\alpha_A F}{RT}\left(\eta - U'\left(c_{s|r=R_s}\right)\right),\\ k_2 &= -\frac{\alpha_C F}{RT}\left(\eta - U'\left(c_{s|r=R_s}\right)\right),\\ \eta &= \phi_1 - \phi_2, \end{aligned} \tag{18}$$

where $c_{s,\max}$ and $c_{l,\max}$ are the maximum Li and Li^+ concentrations in the electrode particle and electrolyte; α_A and α_C are the anodic and cathodic transfer coefficients; η is the surface overpotential; and $U'(c_{s|r=R_s})$ is the open circuit potential as a function of Li concentration.

The surface pressure, P_{micro}, has contributions due to the inclusion of the particle in the swelling aggregate, P_h, and from surface stress, P_{SS}, which can be written for spherical particles as [24]:

$$P_{\text{micro}} = P_h + P_{SS}, \tag{19}$$

$$P_{SS} = -2\frac{\tau_0 + K^s\varepsilon_T|_{r=R_s}}{R_s}, \tag{20}$$

where τ_0 is the deformation-independent surface tension, K^s is the surface modulus, and ε_T is the tangential strain, which in spherical coordinates is defined as: $\varepsilon_T = u_r/r$. The model presented here does not include more complex phenomena such as non-Fickian diffusion, the effects of chemical potential on stress, finite strains, and plastic deformations [25–27].

2.3. Governing equations at meso-scale

The influence of the micro-scale particles on the macro-scale is seen through the effective pore wall flux, j_{eff}, and chemical chemically induced eigenstrain $\mathbf{e}_{ch}$. Similarly, the microscopic pore wall flux, j_s, and surface pressure, P_h depend on both macro- and micro-scale state variables. Aggregate theory [28] and Bruggeman relations [16,20] are used to relate the scales. The effective pore wall flux is related to the micro-scale pore wall flux through:

$$j_{\text{eff}} = \frac{3(1-\varepsilon)}{R_s}j_s. \tag{21}$$

The porosity of the electrode influences the effective properties D_{eff} and κ_{eff} which are found via Bruggeman relations based on the diffusion coefficient D_l and electrolyte conductivity, κ_∞ in the bulk electrolyte:

$$\begin{aligned} D_{\text{eff}} &= \varepsilon D_l,\\ \kappa_{\text{eff}} &= \varepsilon^{3/2}\kappa_\infty. \end{aligned} \tag{22}$$

The micro-scale surface pressure and macro-scale chemically induced eigenstrain depend on macro- and micro-scale strains through the Mori-Tanaka model [28–30]. Here, we assume there is no chemically induced strain in the electrolyte.

$$P_h = \left(\mathbf{b}_s + \mathbf{B}_s\mathbf{C}_{\text{eff}}(\mathbf{e} - \mathbf{e}_{ch})\right)\hat{\mathbf{n}}, \tag{23}$$

$$\mathbf{e}_{ch} = (1-\varepsilon)\mathbf{e}_V + (1-\varepsilon)\left(\mathbf{C}_s^{-1} - \mathbf{C}_l^{-1}\right)\mathbf{b}_s, \tag{24}$$

where $\mathbf{C}_l$ and $\mathbf{C}_s$ are the isotropic constitutive tensors of the electrolyte and active particles and $\mathbf{C}_{\text{eff}}$ is the effective material tensor of the composite electrode. The matrices $\mathbf{B}_s$ and $\mathbf{b}_s$ are homogenization operators; for details, the reader is referred to references [15] and [2].

The micro-scale volumetric strain, $\mathbf{e}_V$ is found via:

$$\mathbf{e}_V = \frac{1}{3}\left(\frac{\left(R_s + u_{r|r=R_s}\right)^3}{R_s^3} - 1\right). \tag{25}$$

2.4. Ragone plot simulation

The set of equations presented in Sections 2.1–2.3 is used to predict the Ragone curve for the battery by simulating the discharge of the battery over a range of rates. We discharge the battery using a Li_xC_6 anode, PEO–$LiCF_3SO_3$ electrolyte, $Li_yMn_2O_4$ cathode system where $0 \le x \le 1$ and $0 \le y \le 1$. Material properties are given in Tables 2–4. For the simulations in this paper, the separator is 50 μm thick and the cathode is 100 μm thick. This yields a theoretical capacity of the battery of 34.8 Ah m^{-2}. The theoretical capacity for a given design is the minimum of the anode and cathode capacities upon discharge. For the cathode, the theoretical capacity is the amount of cathode active material multiplied by the amount of Li that can be intercalated into the cathode particles:

$$\int_{x=\delta_{SC}}^{x=\delta_{CC}} (1-\varepsilon)\mathrm{d}x\left(c_{s,\max} - c_{s,0}\right)*F. \tag{26}$$

Similarly the capacity of the anode is the amount of anode active material multiplied by the amount of Li present in the anode at the start of the discharge:

$$\int_{x=\delta_{AC}}^{x=\delta_{AS}} (1-\varepsilon)\mathrm{d}x*c_{s,0}*F. \tag{27}$$

The thickness of the anode of 142 μm was chosen so that both electrodes would have the same theoretical capacity. The battery is discharged at a constant rate, I, until the potential difference between the electrodes $(\phi_1|_{x=\Gamma_{CC}} - \phi_1|_{x=\Gamma_{AC}})$ reaches the cutoff potential, $\hat{\phi}_1$ of 2.7 V; this cutoff potential was selected due to its position on the discharge curves – as below 2.7 V, the battery potential quickly drops to zero with a negligible increase in capacity.

At both scales, the governing equations are discretized spatially using finite elements and in time using an implicit Euler backwards scheme. An adaptive time stepping algorithm is used that varies the time step size based on the rate of change of the potential difference across the electrodes of the battery. Spatially, we discretize the system using 20 elements in the separator region, 80 elements in each electrode region, and 20 elements in each micro-scale problem. Studies were performed to ensure mesh and time

Table 2
Anode material parameters, Li_xC_6, $0 \le x \le 1$.

Symbol	Value	Units	Description
$c_{s,\max}$	26,400	mol m^{-3}	Maximum Li concentration in cathode
$c_{s,0}$	13,070	mol m^{-3}	Initial Li concentration in cathode
σ_s	100	S m^{-1}	Conductivity in cathode
D_s	5e-13	m^2 s^{-1}	Diffusivity of Li in cathode
E_s	15	GPa	Young's modulus
ν_s	0.3	–	Poisson's ratio
Ω	4.221e-6	m^3 mol^{-1}	Partial molar volume
k_2	1e-10	m^4 mol^{-1} s^{-1}	Butler–Volmer reaction rate constant

Table 3
PEO–$LiCF_3SO_3$ electrolyte material parameters.

Symbol	Value	Units	Description
$c_{l,max}$	3920	mol m^{-3}	Maximum Li^+ concentration in electrolyte
$c_{l,0}$	2070	mol m^{-3}	Initial Li^+ concentration in electrolyte
κ_∞	6.5e-3	S m^{-1}	Conductivity in electrolyte
D_l	7.5e-12	m^2 s^{-1}	Diffusivity of Li in electrolyte
E_l	0.69	MPa	Young's modulus
ν_l	0.4	–	Poisson's ratio

convergence. Two-point Gauss integration is used at the macro-scale which results in 320 micro-scale problems. In total, there are 564 macro-scale state variables, and 33,280 micro-scale state variables.

Fig. 3 is a Ragone plot of the rate versus usable capacity tradeoff seen when the battery is discharged at 14 rates ranging from 0.01 A m^{-2} to 25 A m^{-2}; these results use a uniform porosity of $\varepsilon = 0.3$ and particle radii of 5 μm in both electrodes. At low discharge rates, the battery utilizes up to 99% of the theoretical capacity of the battery. However as the discharge rate increases, there is a significant drop in the usable capacity of the battery. Ideally, the usable capacity of the battery would not decrease with increasing discharge rate.

We compare the discharge of the battery using a carbon anode to a Li foil anode. The theoretical capacity of the battery is the same, however the Li foil provides an effectively unlimited source of Li^+ at the anode-separator boundary, Γ_{AS}. As seen in Fig. 3, this shifts the Ragone line to the right, i.e. higher capacities for higher rates. Nevertheless, the decrease in usable capacity for high rates is still seen. The advantage of analyzing the capacity of the half-cell of the cathode cycled vs. a Li foil anode is in the decrease in computational cost as the anode does not need to be discretized. For the computational model used in this study, the number of macro-scale state variables decreases to 404 and the number of micro-scale state variables is halved from 33,280 to 16,640.

When discharging the half-cell, the cutoff potential is set at 3.2 V. The higher cutoff potential as compared to the carbon anode simulations is due to the constant anode potential (versus increasing potential) during discharge for the half-cell simulations. For both types of studies, the cutoff potentials were selected based on reaching the regime in which the overall battery potential quickly drops to zero. Qualitatively, the Ragone plots predicted by this model are in good agreement with experimental results for Li batteries [17].

3. Design optimization

In order to improve the high rate usable capacity of the battery, we optimize the electrode structure when the battery is discharged

Table 4
Cathode material parameters, $Li_yMn_2O_4$, $0 \le y \le 1$.

Symbol	Value	Units	Description
$c_{s,max}$	22,900	mol m^{-3}	Maximum Li concentration in cathode
$c_{s,0}$	4351	mol m^{-3}	Initial Li concentration in cathode
σ_s	3.8	S m^{-1}	Conductivity in cathode
D_s	7.08e-15	m^2 s^{-1}	Diffusivity of Li in cathode
E_s	10	GPa	Young's modulus
ν_s	0.3	–	Poisson's ratio
Ω	3.497e-6	m^3 mol^{-1}	Partial molar volume
k_2	1e-10	m^4 mol^{-1} s^{-1}	Butler–Volmer reaction rate constant
τ_0	−0.606	J m^{-3}	Surface tension (Si value)
K^s	10.65	N m^{-1}	Surface modulus (Si value)

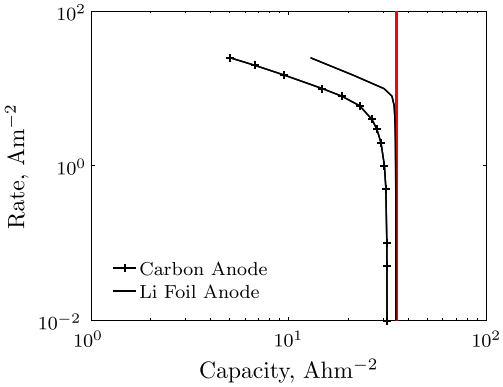

Fig. 3. Ragone Plot for full battery simulation with $\varepsilon = 0.3$ and $R_s = 5$ μm, for both types of anodes, the vertical line is the theoretical capacity.

over a range of discharge rates, $I_j j = 1{:}N_j$, where N_j is the number of rates simulated. Previous studies have shown an influence of the porosity and micro-scale particle radii on the discharge behavior of the battery [15,31,2]. Therefore we consider the local porosities and electrode particle radii in both electrodes as design variables. For a given layout of the electrodes, we simulate the discharge of the battery over the specified range to the cutoff potential and maximize the minimum capacity for the range of discharge rates considered. This max-min multi-objective optimization problem is solved via a bound formulation [32]. To this end, we introduce an auxiliary variable, β:

$$\beta = \min(I_j \hat{t}_j), \tag{28}$$

where $\hat{t}_j$ is the time the battery reaches the cutoff potential when discharged at rate I_j. The objective is to maximize β by manipulating the design variables, **s**. Constraints are placed on the difference, $\beta - I_j\hat{t}_j$, in order to ensure that β is the minimum value. This results in the following problem formulation:

$$\begin{aligned} &\max_{\mathbf{s}} \beta(\mathbf{s}) \\ &s.t. G_j = \beta - I_j\hat{t}_j \le 0 \quad \forall\ j = 1,\ldots,N_j. \end{aligned} \tag{29}$$

The design variables of the particle radii are limited to be between 1 nm and 10 μm and the porosities are limited to between 0.05 and 0.95 to ensure that both electrode and electrolyte phases are present throughout the electrode. In addition, we place constraints on the maximum stress level in the micro-scale electrode particles during discharge:

$$\begin{aligned} &G_\sigma = \max_t \max_r \max_i \sigma_{T,j,t,r,t} - \sigma_{\max} \le 0, \\ &\forall j = 1:N_j,\ t = 1:N_{t,j},\ i = 1:N_m,\ r = 1:N_r \end{aligned}, \tag{30}$$

where r is the node id of the particle finite element model, i the individual micro-scale particle, and t the time step. $N_{t,j}$ is the number of time-steps needed when discharged at rate I_j, N_m is the number of micro-scale particles, and N_r is the number of nodes in the particle model. In this paper, we set σ_{max} to 50 MPa. This stress level was chosen on the basis of stress levels seen in the constant porosity solutions of Ref. [2]. To reduce the number of stress constraints, we approximate the maximum particle stress in an

Table 5
GCMMA parameters.

Parameter	Value
Step size, Δ_s	0.01–0.2
Initial adaptation of asymptotes	0.5
Adaptation of asymptotes	0.7
Maximum number of sub-cycles	1
Relative change in optimization variables	$\Delta_s = 10^{-8}$

individual particle, i, at discharge rate I_j using the Kreisselmeier–Steinhauser (KS) function with $\omega = 3$:

$$\tilde{\sigma}_{T,j,i} = \frac{1}{\omega}\ln\sum_t\sum_r \exp(\omega\sigma_{T,j,t,r,i}) \quad t = 1:N_{t,j}, r = 0:R_s. \tag{31}$$

The accuracy of this approximation has been monitored in the numerical examples to ensure the approximation is accurate to within 0.1% at 50 MPa.

The design optimization problems are solved using the Globally-Convergent Method of Moving Asymptotes (GCMMA) of Svanberg [33]. The GCMMA constructs a sequence of convex separable subproblems that are solved by a primal-dual method, and is guaranteed to converge to a Karush–Kuhn–Tucker (KKT) optimal point. This algorithm is specifically suited for problems with large numbers of design variables and few inequality constraints as it is the case in the current study. The GCMMA is considered converged if the constraints are satisfied and the relative change in design variables, Δ_s is sufficiently small:

$$\frac{||\mathbf{s}^{m-1} - \mathbf{s}^m||}{||\mathbf{s}^{m-1}||} \leq \Delta_s, \tag{32}$$

where m is the iteration number of the optimization process. Parameters used by the GCMMA are given in Table 5; for a detailed explanation of these parameters, the reader is referred to Ref. [33].

GCMMA requires the derivatives of G_j and G_σ, with respect to the design variables. The derivatives of the objective, β, with respect to the design variables are zero, while the derivatives of the constraints, G_j and G_σ, are nonzero due to the dependence of the simulation time, $\hat{t}_j$, and model behavior on the design variables. Due to the potentially high number of design variables and computational cost of the model, the sensitivities are found using an adjoint approach. The main advantage of this approach is that the numerical costs of computing the design sensitivities are nearly independent of the number of design variables. For the problem of interest, the adjoint sensitivity equations only need to be solved N_G times in each step of the optimization procedure, where N_G is the number of constraints. This involves integrating backward in time the linearized multi-scale model described in Section 2. Details on the formulation, numerical procedure, and computational efficiency of performing adjoint sensitivity analysis for the multi-scale framework are provided in Golmon et al. [2].

4. Design optimization examples

4.1. Optimization of cathode discharged against Li foil anode

We solve the above design optimization problem (29) for a range of discharge rates, I_j = [0.01:20] A m^{-2}, first with a Li foil anode. The cathode is initialized with uniform porosity of 0.3 and particle radii of 5 μm, consistent with the nominal design in previous studies [15]. Fig. 4(a) shows the effect of optimizing the electrode design on the Ragone plot, and Fig. 4(b) and (c) plots the

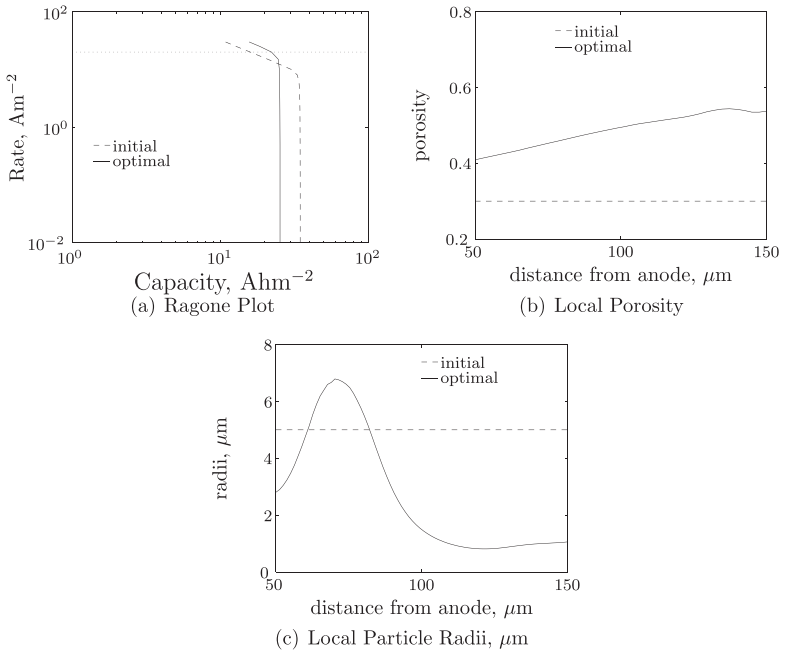

Fig. 4. Ragone plot, porosity and particle radii distributions of initial and optimal designs for design optimization problem with I_j = [0.01:20] A m^{-2}.

initial and optimal porosity and particle radii distributions. A 39% improvement in capacity is obtained at 20 A m^{-2}, however at low rates, there is a 27% decrease in capacity. The theoretical capacity of the battery decreases from 34.80 Ah m^{-2} to 29.8 Ah m^{-2} due to the increased porosity of the electrode. The optimal configuration achieves 75% of the theoretical capacity at 20 A m^{-2} and up to 86% of the theoretical capacity at lower discharge rates. The optimization problem is dominated by the performance at the 20 A m^{-2} discharge rate which has the lowest capacity and highest electrode particle stress levels throughout the optimization process. This would allow for a reduction of the optimization problem to a simple single-objective problem, maximizing the capacity at a discharge rate of 20 A m^{-2}.

The influence of the electrode design on the behavior of the battery is seen in Figs. 5 and 6 which show the Li^+ concentration in the electrolyte, the normalized Li concentration in the electrode particles, and the stress levels in the electrode particle as a function of time and position within the battery for initial and optimal configurations for 10 A m^{-2} and 20 A m^{-2} discharge rates.

Two main mechanisms dominate the discharge process: (1) lithiation of the cathode particles at the back of the electrode as seen in Fig. 5(d), and (2) depletion of Li^+ in the electrolyte within the cathode as seen in Figs. 5(a), 6(a) and 6(b). Depletion of Li^+ in the electrolyte is undesirable as it prohibits full utilization of the active material. Once the electrolyte is depleted, the potential of the battery drops quickly. The optimal design for these rates increases the porosity towards the back of the electrode which allows for increased Li^+ transport in the electrolyte and thus a longer time before depletion occurs. The electrode particle size is decreased near the separator-cathode interface primarily to decrease the stress levels in the particles; smaller particles allow for faster diffusion of Li into the particles, decreasing the stress and strain

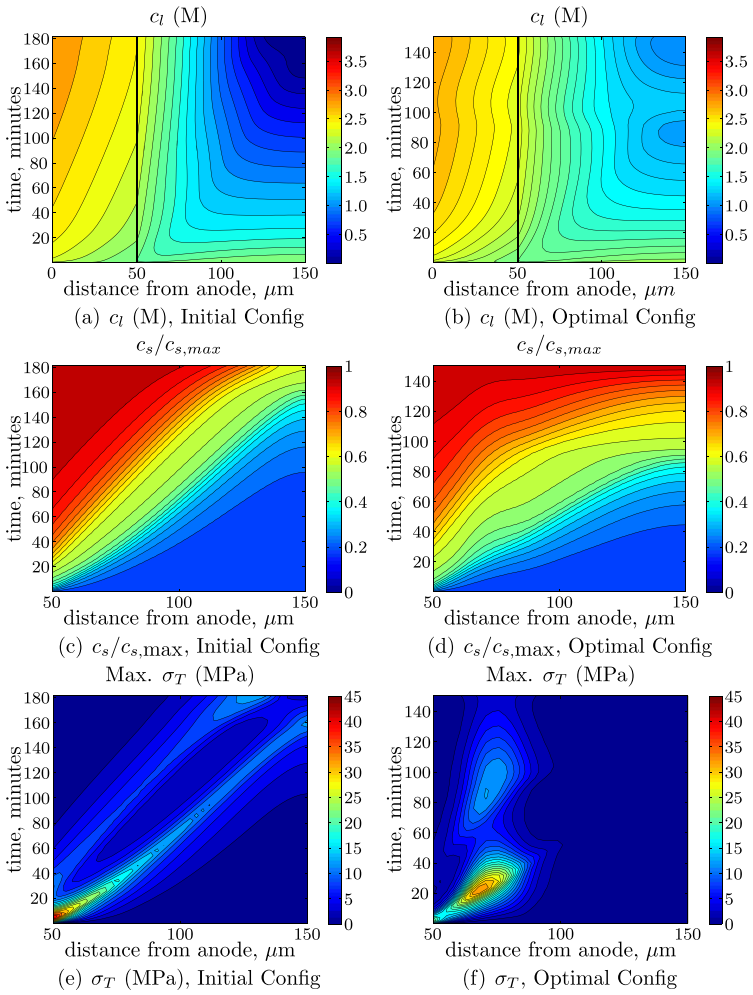

Fig. 5. c_l and c_s concentrations and maximum σ_T as a function of time and position in the battery for initial and optimal configurations when discharged at $I = 10$ A m^{-2} for the optimization problem with I_j = [0.01:20] A m^{-2}. The vertical lines in (a) and (b) show the separator-cathode interface.

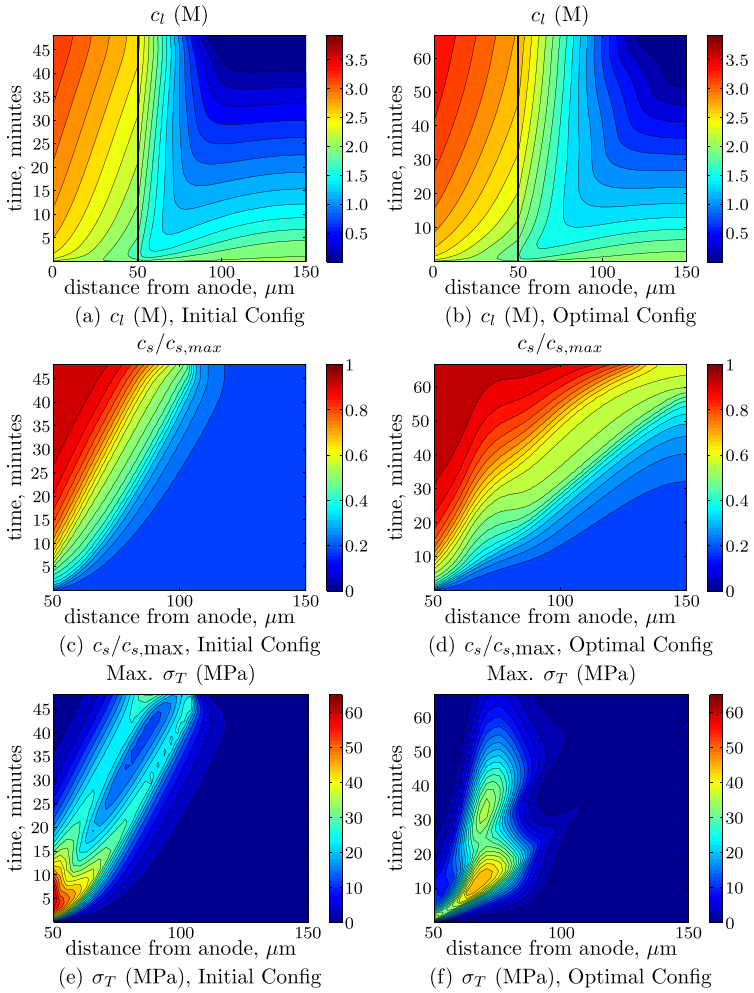

Fig. 6. c_l and c_s concentrations and maximum σ_T values as a function of time and position in the battery for initial and optimal configurations when discharged at $I = 20$ A m^{-2} for the optimization problem with I_j = [0.01:20] A m^{-2}. The vertical lines in (a) and (b) show the separator-cathode interface.

mismatch in the particle. The larger particle sizes slow the rate of Li^+ uptake by the particles, which results in enhanced Li^+ transport towards the back of the cathode [2]. The optimal porosity distribution is most important in increasing the battery capacity, while adding the radii as design variables allows for a further improvement on the order of 0.5–1 Ah m^{-2}.

For the discharge at 20 A m^{-2} using the initial configuration, only the front half of the cathode is saturated with Li during discharge (Fig. 6(c)) and the cathode particles at the current collector interface only see a negligible increase in Li concentration. The stress constraint level of 50 MPa is exceeded near the separator–cathode interface (Fig. 6(e)).

In contrast, for the optimal configuration, the Li concentration throughout the cathode increases during discharge (Fig. 6(d)) which increases the capacity and percent utilization of the theoretical capacity of the battery. The Li^+ concentration at the back of the cathode (Fig. 6(b)) is depleted over a smaller region of the cathode and occurs later in the discharge. The stress levels in the particles are maintained below 50 MPa (Fig. 6(f)) with the highest stress levels positioned at the largest particle sizes. The "waves" seen in the contour lines for the normalized Li concentration in the cathode particles are due to the interplay between the different Li transport rates in the electrolyte and particles.

If the range of discharge rates is reduced to a range of [0.01:10] A m^{-2} or [0.01:1] A m^{-2}, the capacity of the battery can be increased over what is possible for the [0.01:20] A m^{-2} range. Fig. 7 shows the designs and Ragone plots for all three optimization problems as compared to the initial configuration. The decrease in the rate range to [0.01:10] A m^{-2} results in an optimal design with a theoretical capacity of 33.96 Ah m^{-2} and the [0.01:1] A m^{-2} range optimal design has a theoretical capacity of 45.21 Ah m^{-2}.

At low discharge rates, the low optimal porosities result in higher usable and theoretical capacity of the battery; here the capacity is reaction-rate limited. As the discharge rate is increased,

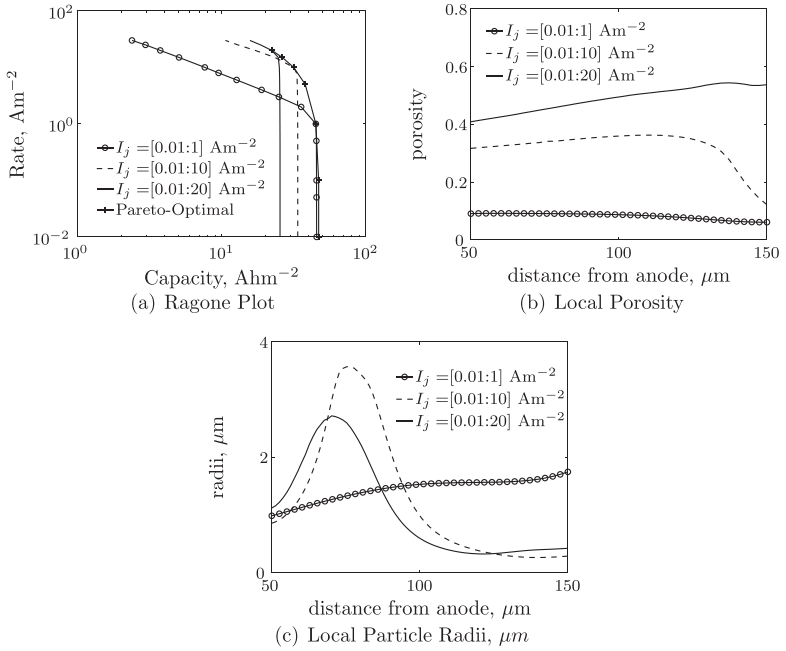

Fig. 7. Ragone plot, porosity and particle radii distributions of initial and optimal designs for all three design optimization problems.

and the transport is limited by diffusion of Li^+ in the electrolyte, the porosity is increased which allows for greater Li^+ transport. Particle size primarily influences stress levels as large particles are diffusion limited resulting in concentration gradients that cause mismatch strains and stresses due to the stress–diffusion coupling; see Eqns. (12) and (13). With very small particles (<0.5 μm), the stress levels will increase due to the surface stress effect; see Eq. (20). The particle size can also influence the usable battery capacity by effecting the local rate of Li^+ uptake throughout the electrode.

A tradeoff is seen between the low and high rate performance of the battery: for the highest rates an increase in usable capacity is shown while the low rates show a decrease in usable capacity. The highest discharge rate dominates the design for each simulation, suggesting that the electrode should be designed based on the highest discharge rate expected during operation. Optimal designs for each discharge rate give upper bounds on what is achievable with these design variables, giving the Pareto-optimal set of designs (Fig. 7(a)).

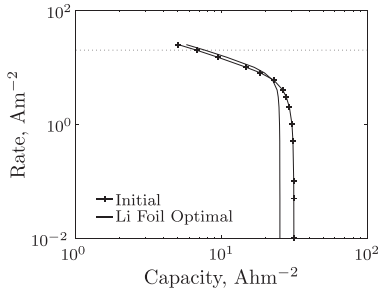

Fig. 8. Ragone plot for the cathode found via optimization of the cathode with a Li foil anode when discharged with a carbon anode.

As a next step, we replace the Li foil anode with a carbon anode as in Section 2.4, which has the optimal cathode porosity and radii distribution from the Li foil [0.01:20] A m^{-2} discharge rate range. As seen in Fig. 8, the performance improvement is significantly reduced and the overall theoretical capacity of the cell is still reduced by 24%. This result demonstrates that it is necessary to perform the design optimization on the full problem if the carbon anode is to replace the Li foil anode.

4.2. Optimization including carbon anode

The design optimization problem (29) is solved for discharge rates of I_j = [0.01:1] A m^{-2}, [0.01:10] A m^{-2}, and [0.01:20] A m^{-2}, with both anode and cathode porosities and radii as optimization variables. Both electrodes are initialized with uniform porosities of 0.3 and particle radii of 5 μm. For simplicity, the stress constraint (30) is applied only in the cathode region.

Simultaneously optimizing the porosity and particle size distributions in a full battery cell results in greater capacity improvement than using the optimal cathode design with the Li foil anode. As shown in Fig. 9, the resulting optimal design for the [0.01:20] A m^{-2} range improves the capacity of the battery by 61% relative to the initial configuration when discharged at 20 A m^{-2}, while at low discharge rates the capacity is decreased by 42%. Similar levels of improvement are seen at the [0.01:1] A m^{-2} and [0.01:10] A m^{-2} rate ranges. The resulting optimal designs are depicted in Fig. 10. This figure also shows the optimal cathode configuration for the Li foil anode optimization problem for the [0.01:20] A m^{-2} discharge rate range.

The high porosity towards the separator region of the battery in both electrodes is due to the limited amount of Li available in the

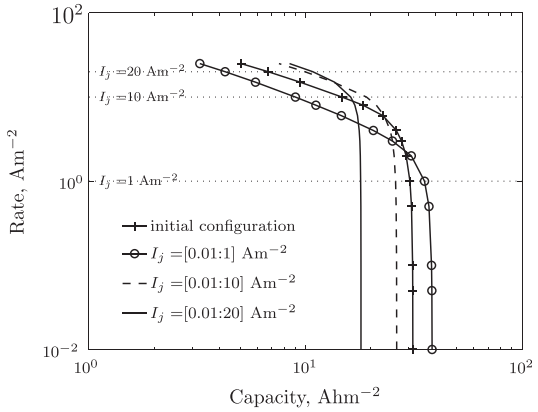

Fig. 9. Ragone plot for initial and optimal configurations for the carbon anode optimization problems.

anode as opposed to the effectively unlimited Li source when a Li foil anode is simulated. Increasing the porosity towards the separator region increases the Li^+ transport rates in the electrolyte allowing a higher percentage of the electrodes to be lithiated. At the highest rate, the cathode porosity is further increased at the back of the cathode to allow for increased Li^+ transport in the electrolyte. In the anode, the optimal particle radii distributions result in a small improvement in Li^+ transport in the electrolyte while in the cathode, the stress constraint also influences the distribution. There is a greater difference in diffusion coefficients between the electrode and electrolyte in the cathode than the anode, resulting in a larger spatial variation of the radii in the cathode.

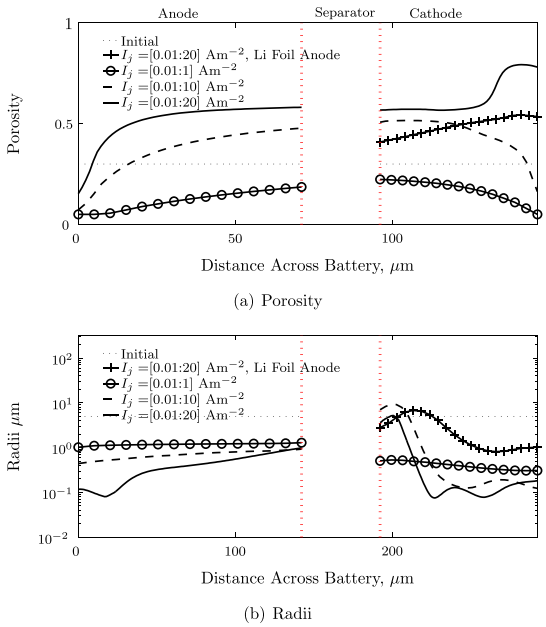

Fig. 10. Initial and optimal electrode designs for dual electrode optimization. The additional dashed lines in the cathode region are the optimal designs for the Li foil anode optimization problem.

To further understand the transport limitations of the battery, in Fig. 11 we examine the internal Li^+, normalized Li concentration, and stress fields within the battery for the initial and optimal designs at a 20 A m^{-2} discharge rate. The initial configuration limits the reactions in the electrodes to the region closest to the separator; the slow Li^+ transport limits the amount of the electrodes utilized. The optimal configuration shows reactions occurring throughout both electrodes, although Li^+ depletion is still the limiting factor. In the initial configuration, the stress levels in the cathode exceed the stress constraint level as shown in Fig. 11(e). The stress levels in the optimal configuration were decreased primarily via the increased porosity and the variation in particle radii enhances Li^+ transport through the depth of the cathode.

The study above shows that optimizing both electrodes simultaneously results in greater improvements in usable capacity than optimizing a half cell. Note, that these simulations were performed for a discharge of the battery and result in asymmetric designs between the anode and cathode, optimization of a full charge/discharge cycle could change the optimal configuration.

5. Conclusion

In this paper, a design optimization approach based on a multiscale battery cell model has been presented and applied to optimizing the electrode design, in order to increase the usable capacity of a battery over a range of discharge rates. Optimal porosity and radii distributions in the battery electrodes were found via a multiobjective design problem with constraints placed on the stress levels in the cathode particles. Studies were performed on both a Li-foil half cell and carbon anode full cell configurations which resulted in different optimal designs. For all studies, the highest rate discharge dominated the performance and the porosity design variables had a greater influence on the usable capacity than the particle radii design variables. Simulations presented showed that the transport of Li^+ in the electrolyte was the dominate process driving the optimal designs resulting in increasing porosities with increasing rates. The particle radii design variables were important in stress-mitigation near the separator-cathode interface and served to further enhance the Li^+ transport due to the effect of particle size on the rate at which Li^+ enters the particles. A tradeoff was observed between low and high rates because the highest rate of discharge drives the optimization problem.

Design optimization of the electrode porosities and particle radii resulted in a 39% increase in capacity for the Li-foil half cell and a 61% increase in capacity for the full cell versus the non-graded design at the 20 A m^{-2} discharge rate. However the optimization results are limited by the level of accuracy of the model which does not include effects such as solid electrolyte interphase (SEI) layer growth, chemical side reactions, and other degradation phenomena. Only a single discharge of the battery was simulated, and optimizing the electrode configuration over a full charge/discharge cycle may result in different optimal electrode structures. Further optimization studies over a full charge/discharge cycle and over multiple cycles, including degradation mechanisms, additional design variables of the electrode thicknesses, and at higher discharge rates are recommended.

Nevertheless, the results presented in this paper suggest that functionally grading the electrode can improve the overall battery performance allowing for greater usable energy density in a battery. Furthermore, this study has demonstrated the utility of computational design optimization as an efficient tool for the development of battery cells. As our optimization approach can incorporate a large number of design variables and can be extended

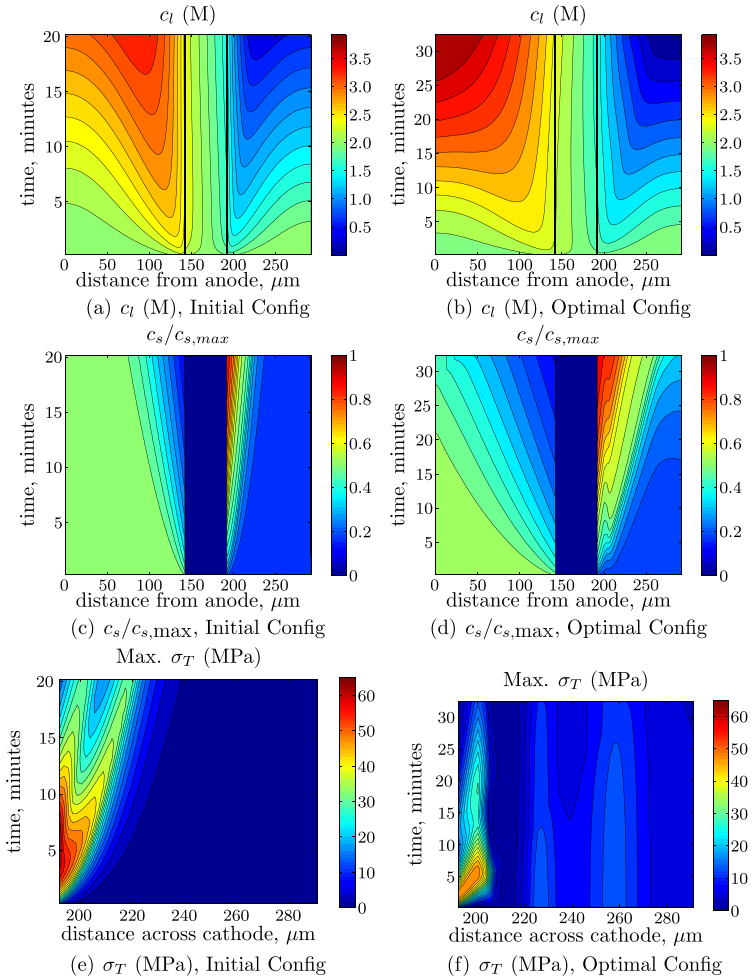

Fig. 11. c_l and c_s concentrations and maximum σ_T as a function of time and position in the battery for initial and optimal configurations when discharged at $I = 20$ A m^{-2} for the full battery optimization problem. The vertical lines show the anode-separator and separator-cathode interface.

onto more complex micro- and macro-scale models, this method could be applied to simulations investigating the overall battery cell design such as those in Ref. [11].

Acknowledgments

The authors gratefully acknowledge the support of the Air Force Office of Scientific Research MURI (Grant No. F9550-06-1-0326) monitored by Dr. B. L. Lee, the National Science Foundation under Grant No. 1201207 and 1231048, and the first author acknowledges the support of a Graduate Research Fellowship from the National Science Foundation.

References

[1] R. Deshpande, M. Verbrugge, Y.-T. Cheng, J. Wang, P. Liu, J. Electrochem. Soc. 159 (2012) A1730–A1738.
[2] S. Golmon, K. Maute, M.L. Dunn, Int. J. Numer. Methods Eng. 92 (2012) 475–494.
[3] Y. Chen, J.W. Evans, Electrochim. Acta 39 (1994) 517–526.
[4] L.-J. Yu, M.-J. Qin, P. Zhu, L. Yang, J. Power Sources 179 (2008) 848–853.
[5] A. Jarrett, I.Y Kim, J. Power Sources (2011) 10359–10368.
[6] M.-J. Kim, H. Peng, J. Power Sources 165 (2007) 819–832.
[7] W. Du, A. Gupta, X. Zhang, A.M. Sastry, Int. J. Heat Mass Transfer 53 (2010) 3552–3561.
[8] Y.-H. Chen, C.W. Wang, X. Zhang, A.M. Sastry, J. Power Sources 195 (2010) 2851–2862.
[9] V. Ramadesigan, R.N. Methekar, F. Latinwo, R.D. Braatz, V.R. Subramanian, J. Electrochem. Soc. 157 (2010) A1328–A1334.
[10] S.K. Rahimian, S. Rayman, R.E. White, J. Power Sources 196 (2011) 10297–10304.
[11] G.-H. Kim, K. Smith, K.-J. Lee, S. Santhanagopalan, A. Pesaran, J. Electrochem. Soc. 158 (2011) A955–A969.
[12] M. Winter, R.J. Brodd, Chem. Rev. 104 (2004) 4245–4269.
[13] D. Wang, X. Wu, Z. Wang, L. Chen, J. Power Sources 140 (2005) 125–128.
[14] H. Wang, Y.-I. Jang, B. Huang, D.R. Sadoway, Y.-M. Chiang, J. Electrochem. Soc. 146 (1999) 473–480.
[15] S. Golmon, K. Maute, M.L. Dunn, Comput. Struct. 87 (2009) 1567–1579.
[16] M. Doyle, T.F. Fuller, J. Newman, J. Electrochem. Soc. 140 (1993) 1526–1533.
[17] T.F. Fuller, M. Doyle, J. Newman, J. Electrochem. Soc. 141 (1994a) 1–10.
[18] T.F. Fuller, M. Doyle, J. Newman, J. Electrochem. Soc. 141 (1994b) 982–990.
[19] M. Doyle, J. Newman, Electrochim. Acta 40 (1995) 2191–2196.

[20] M. Doyle, Design and Simulation of Lithium Rechargeable Batteries (Ph.D. thesis), University of California, Berkeley, 1995.
[21] J. Newman, K.E. Thomas, Electrochemical Systems, third ed., Wiley-Interscience, 2004.
[22] P. Arora, M. Doyle, A.S. Gozdz, R.E. White, J. Newman, J. Power Sources 88 (2000) 219–231.
[23] X. Zhang, W. Shyy, A.M. Sastry, J. Electrochem. Soc. 154 (2007) 910–916.
[24] Y.T. Cheng, M.W. Verbrugge, J. Appl. Phys. 104 (2008) 083521.
[25] A. Bower, P. Guduru, V. Sethuraman, J. Mech. Phys. Solids 59 (2011) 804–828.
[26] K. Zhao, M. Pharr, S. Cai, J.J. Vlassak, Z. Suo, J. Am. Ceram. Soc. 94 (2011) S226–S235.
[27] Z. Cui, F. Gao, J. Qu, J. Mech. Phys. Solids 60 (2012) 1280–1295.
[28] T. Mori, K. Tanaka, Acta Metall. 21 (1973) 571–574.
[29] Y. Benveniste, Mech. Mater. 6 (1987) 147–157.
[30] Y. Benveniste, G. Dvorak, in: Micromechancis and Inhomogeneity, Springer, New York, 1990.
[31] S. Golmon, K. Maute, S.-H. Lee, M.L. Dunn, Appl. Phys. Lett. 97 (2010).
[32] N. Olhoff, Struct. Multidis. Optim. 1 (1989) 11–17, http://dx.doi.org/10.1007/BF01743805.
[33] K. Svanberg, SIAM J. Optim. 12 (2002) 555–573.
[34] P.V. den Bossche, F. Vergels, J.V. Mierlo, J. Matheys, W.V. Autenboer, J. Power Sources 162 (2006) 913–919.